Falling Film Evaporation on a Tube Bundle with Plain and Enhanced Tubes

THÈSE N^{O} 4341 (2009)

PRÉSENTÉE LE 3 AVRIL 2009
À LA FACULTÉ SCIENCES ET TECHNIQUES DE L'INGÉNIEUR
LABORATOIRE DE TRANSFERT DE CHALEUR ET DE MASSE
PROGRAMME DOCTORAL EN ENERGIE

ÉCOLE POLYTECHNIQUE FÉDÉRALE DE LAUSANNE

POUR L'OBTENTION DU GRADE DE DOCTEUR ÈS SCIENCES

PAR

Mathieu HABERT

acceptée sur proposition du jury:

Prof. P. Monkewitz, président du jury
Prof. J. R. Thome, directeur de thèse
Prof. J. Bonjour, rapporteur
Prof. D. Favrat, rapporteur
Prof. G. Ribatski, rapporteur

ÉCOLE POLYTECHNIQUE
FÉDÉRALE DE LAUSANNE
Suisse
2009

Abstract

The complexities of two-phase flow and evaporation on a tube bundle present important problems in the design of heat exchangers and the understanding of the physical phenomena taking place. The development of structured surfaces to enhance boiling heat transfer and thus reduce the size of evaporators adds another level of complexity to the modeling of such heat exchangers. Horizontal falling film evaporators have the potential to be widely used in large refrigeration systems and heat pumps, in the petrochemical industry and for sea water desalination units, but there is a need to improve the understanding of falling film evaporation mechanisms to provide accurate thermal design methods. The characterization of the effect of enhanced surfaces on the boiling phenomena occurring in falling film evaporators is thus expected to increase and optimize the performance of a tube bundle. In this work, the existing LTCM falling film facility was modified and instrumented to perform falling film evaporation measurements on single tube row and a small tube bundle. Four types of tubes were tested including: a plain tube, an enhanced condensing tube (Gewa-C+LW) and two enhanced boiling tubes (Turbo-EDE2 and Gewa-B4) to extend the existing database. The current investigation includes results for two refrigerants, R134a and R236fa, at a saturation temperature of $T_{sat} = 5°C$, liquid film Reynolds numbers ranging from 0 to 3000, at heat fluxes between 20 and $60 kW/m^2$ in pool boiling and falling film configurations. Measurements of the local heat transfer coefficient were obtained and utilized to improve the current prediction methods. Finally, the understanding of the physical phenomena governing the falling film evaporation of liquid refrigerants has been improved. Furthermore, a method for predicting the onset of dry patch formation has been developed and a local heat transfer prediction method for falling film evaporation based on a large experimental database has been proposed. These represent significant improvements for the design of falling film evaporators.

Keywords: falling film evaporation, pool boiling, enhanced boiling, heat transfer, two-phase flow, Wilson plot

Version Abrégée

La complexité des écoulements diphasiques au sein d'un faisceau de tubes soulève de nombreux problèmes de compréhension des phénomènes physiques y prenant place et, par la suite, lors de leur dimensionnement. Le développement récent de surfaces améliorées censées améliorer le transfert de chaleur, et donc, réduire la taille de l'évaporateur, rajoute un autre degré de complexité lors la modélisation de ces échangeurs de chaleur. Les évaporateurs à film tombant ont le potentiel pour être largement utilisés pour des grandes unités frigorifiques dans des pompes à chaleur et dans l'industrie pétrochimique ou pour le dessalement de l'eau de mer, mais il est nécessaire d'améliorer au préalable la connaissance des mécanismes d'évaporation en film pour fournir des méthodes performantes de dimensionnement pour échangeurs de chaleur. La caractérisation de l'influence des surfaces améliorées sur le phénomène d'ébullition se produisant dans les évaporateurs à film tombant devrait permettre de mieux comprendre l'augmentation et d'optimisation des performances observées avec un faisceau de tubes. Par conséquent, l'installation expérimentale du LTCM pour les échanges en film tombant a été modifiée avec l'instrumentation nécessaire pour effectuer des mesures sur une colonne de tubes horizontaux et un petit faisceau de tubes. Quatre types de tubes ont été testés: un tube lisse, un tube amélioré pour la condensation (Gewa-C+LW) et deux tubes améliorés pour l'ébullition (Turbo-EDE2 et Gewa-B4) afin d'augmenter la base de données existante. L'étude suivante présente des résultats obtenus avec deux réfrigérants, R134a et R236fa, une température de saturation $T_{sat} = 5°C$, des nombres de Reynolds compris entre 0 et 3000, des densités de flux de chaleur entre 20 et $60kW/m^2$ (méthode de Wilson, ébullition en vase et évaporation en film tombant). Des mesures locales du coefficient de transfert de chaleur ont été obtenues et utilisées pour améliorer les méthodes actuelles de prédiction. A l'issue de ce travail, la compréhension des phénomènes physiques régissant l'évaporation des réfrigérants en film tombant a été améliorée. Deux méthodes ont été proposées: une pour la prédiction de l'apparition de la formation de zones sèches et une pour le transfert de chaleur de l'évaporation en film tombant, basée sur une grande base de données expérimentales. Elles constituent une amélioration significative pour la conception des évaporateurs à film tombant.

Mots clés: évaporation en film tombant, ébullition en vase, ébullition améliorée, transfert de chaleur, écoulement biphasique, méthode de Wilson

Acknowledgments

This study has been carried out at the Laboratory of Heat and Mass Transfer (LTCM), Swiss Federal Institute of Technology Lausanne (EPFL), under the direction of Prof. John R. Thome. This project has been supported financially by the LTCM Falling Film Research Club members: Johnson Controls Inc., Trane, Wieland-Werke AG and Wolverine Tube Inc, which is gratefully acknowledged. Special acknowledgment is made to Wieland-Werke AG and Wolverine Tube Inc for providing the tube samples for the tests.

I would like to thank Prof. John R. Thome for giving me the opportunity to perform this investigation in his laboratory. His experience and expertise in two-phase flow guided me over the past years. I also would like to express my gratitude to my thesis examiners, Prof. Jocelyn Bonjour, INSA Lyon, Prof. Daniel Favrat, EPFL and Prof. Gherhardt Ribatski, Universidade de São Paulo.

I would like to thank also all my colleagues of the LTCM, who contributed in different ways to this thesis, with warm coffee breaks and interesting discussions over the last years. I particularly thank Laurent Chevalley for helping me with the technical work and making me discover Switzerland and its beauties.

Finally, I would like to thank all my friends and family for their support, and particularly Sarifa, my future wife, who hopefully will support me for all my life.

Contents

Abstract iii

Version Abrégée v

Acknowledgments vii

Nomenclature xix

1 Introduction 1

2 State of the art review 3

- 2.1 Hydrodynamics of a liquid film . . . 3
  - 2.1.1 Falling film intertube modes and transitions . . . 3
  - 2.1.2 Film breakdown and hot patches . . . 6
  - 2.1.3 Vapor/liquid interaction . . . 7
  - 2.1.4 Tube bundle flow . . . 9
- 2.2 Heat transfer mechanisms . . . 9
  - 2.2.1 Convection . . . 10
  - 2.2.2 Nucleate pool boiling . . . 11
- 2.3 Falling film enhancement . . . 13
- 2.4 Single tube and single tube row heat transfer studies . . . 14
  - 2.4.1 Saturation temperature effect . . . 14
  - 2.4.2 Heat flux effect . . . 15
  - 2.4.3 Flow rate effect . . . 15
  - 2.4.4 Tube diameter effect . . . 15
  - 2.4.5 Liquid feeder effect . . . 16
  - 2.4.6 Vapor flow effect . . . 17

2.4.7 Enhanced surfaces . . . 17
2.5 Tube bundle heat transfer studies . . . 19
2.6 Falling film heat transfer models . . . 21
2.6.1 Smooth tubes . . . 21
2.6.2 Enhanced surfaces . . . 24

3 Description of experiments 27
3.1 Falling film test facility . . . 27
3.1.1 Refrigerant circuit . . . 28
3.1.2 Water circuit . . . 30
3.1.3 Glycol circuit . . . 31
3.2 Test section . . . 32
3.2.1 Liquid distribution . . . 33
3.2.2 Tube layout . . . 34
3.3 Refrigerants . . . 35
3.4 Data acquisition and control . . . 36
3.4.1 Data acquisition system . . . 36
3.4.2 Control system . . . 37
3.5 Measurements and accuracy . . . 37
3.5.1 Instrumentation of the test section . . . 37
3.5.2 Physical properties estimation . . . 38
3.5.3 Saturation temperature . . . 38
3.5.4 Mass flow meters . . . 38
3.5.5 Water temperature profile . . . 38
3.5.6 Local heat flux . . . 40
3.5.7 Film Reynolds number . . . 41

4 Wilson plot method 43
4.1 Heat transfer calculation principles . . . 43
4.2 Wilson plot method . . . 45
4.3 Modified Wilson plot method . . . 46
4.3.1 Calculation principles . . . 46

4.3.2 Measurement system validation 48
4.3.3 Measurement procedure 48
4.3.4 Results and accuracy 49
4.3.5 Summary 50
4.4 Heat transfer measurement accuracies 52
4.4.1 Local heat flux 52
4.4.2 Local heat transfer coefficient 53

5 Single Row Falling Film Evaporation 55
5.1 Plain tube results 55
5.1.1 Pool boiling results 55
5.1.2 Falling film evaporation results 57
5.2 Enhanced surface results 60
5.2.1 Pool boiling results 60
5.2.2 Falling film evaporation results 62
5.3 Conclusions and remarks 67

6 Results on falling film bundle evaporation 69
6.1 Bundle Modifications 69
6.2 Measurement procedure 71
6.3 Plain tube results 72
6.4 Enhanced surface results 75
6.4.1 Gewa-C+LW 75
6.4.2 Gewa B4 76
6.4.3 Turbo-EDE2 76
6.5 Critical analysis of the Wilson plot method 77
6.6 Trend analysis 78
6.7 Conclusions and remarks 79

7 Heat transfer models 81
7.1 Onset of film breakdown prediction 81
7.2 New heat transfer prediction method for single-array 85
7.2.1 Apparent wet fraction area 85

7.2.2 Wet heat transfer coefficient 86
7.2.3 Local heat transfer coefficient prediction statistics 90
7.3 Prediction of bundle heat transfer 94
7.3.1 Plain Tube prediction 95
7.3.2 Enhanced tube prediction 97
7.3.3 Conclusion 100

8 Conclusion **101**

Bibliography **103**

Curriculum Vitae **109**

List of Figures

2.1 Intertube falling-film modes: (a) droplet mode; (b) column mode; (c) sheet mode; (d) illustration of the Taylor instability [8] 4

2.2 Schematic of a stable dry patch [15] 6

2.3 Schematic of liquid film breakdown from [8] 7

2.4 a) Droplet deflection due to vapor cross flow b) Column deflection due to vapor crossflow [7] 8

2.5 Falling film thermal regimes 10

2.6 Evaporation processes on an enhanced boiling surface, from Thome [2] . . 13

2.7 Schematic of the variation of heat transfer coefficient with flow rate for falling film evaporation 16

2.8 Cross-over characteristics of pored enhanced tubes as reported by Chien and Webb [34] 18

2.9 Schematic of a liquid collector with plain tubes from [56] 20

2.10 Comparison of the overall heat transfer coefficient with and without collector for R141b from [56] 20

2.11 Process of evaporation inside subsurface tunnel: Bubble growth and departure from [68] 26

3.1 3-D Solidworks drawing of the falling film facility 28

3.2 Schematic of the falling film evaporation refrigerant circuit 29

3.3 Schematic of the forced-circulation loop for the heating water 30

3.4 Schematic of the forced-circulation of glycol 31

3.5 3-D Solidworks drawing of the test Section 33

3.6 Schematic of the liquid distributor 34

3.7 Tube array and bundle layout 35

3.8 Tube instrumentation 39

3.9 Schematics of the calibration set-up 40

4.1 Thermal resistance diagram and temperature distribution during falling film evaporation . . . 44

4.2 Measurement system validation using Nüsselt theory . . . 48

4.3 Modified Wilson plots for all types of tubes in pool boiling . . . 50

5.1 Pool boiling measurement on plain tube for R134a and R236fa . . . 56

5.2 Comparison of experimental versus predicted values for pool boiling on a plain tube . . . 56

5.3 Comparison of pool boiling measurements with prediction methods on plain tube at $T_{sat} = 5°C$ for R134a and R236fa . . . 57

5.4 Falling film evaporation on plain tube at $T_{sat} = 5°C$ with R236fa . . . 58

5.5 Falling film evaporation on plain tube at $T_{sat} = 5°C$ with R134a (Roques [3]) 59

5.6 Falling film multiplier K_{ff} on plain tube at $T_{sat} = 5°C$ for R134a and R236fa 59

5.7 Pool boiling measurement on the Gewa-C+LW for R134a and R236fa . . . 60

5.8 Pool boiling measurement on Gewa-B4 for R134a and R236fa . . . 61

5.9 Pool boiling measurement on Turbo-EDE2 for R134a and R236fa . . . 61

5.10 Falling film evaporation on Gewa-C+LW at $T_{sat} = 5°C$ for R134a and R236fa 62

5.11 Falling film multiplier K_{ff} on Gewa-C+LW at $T_{sat} = 5°C$ for R134a and R236fa . . . 63

5.12 Falling film evaporation on Gewa-B4 at $T_{sat} = 5°C$ for R134a and R236fa . 63

5.13 Falling film evaporation on Gewa-B at $T_{sat} = 5°C$ for R134a [3] . . . 64

5.14 Falling film multiplier K_{ff} on Gewa B4 at $T_{sat} = 5°C$ for R134a and R236fa 64

5.15 Falling film evaporation on Turbo-EDE2 at $T_{sat} = 5°C$ for R134a and R236fa 65

5.16 Falling film evaporation on Turbo-BII and High-Flux tubes at $T_{sat} = 5°C$ for R134a [3] . . . 65

5.17 Falling film multiplier K_{ff} on Turbo-EDE2 at $T_{sat} = 5°C$ for R134a and R236fa . . . 66

5.18 Schematic of the formation of the bubbly liquid film around the tube . . . 67

6.1 Working principle of the bundle . . . 69

6.2 Schematic of the new circuits used for the bundle . . . 70

6.3 Bundle falling film coefficient on plain tube at $T_{sat} = 5°C$ for R134a . . . 72

6.4 Bundle falling film coefficient on plain tube at $T_{sat} = 5°C$ for R236fa . . . 73

6.5 Liquid distribution within the tube bundle . . . 74

6.6 Bundle falling film coefficient on Gewa-C+LW at $T_{sat} = 5°C$ for R134a . . 75

6.7 Bundle falling film coefficient on Gewa-C+LW at $T_{sat} = 5°C$ for R236fa . . 75
6.8 Bundle falling film coefficient on Gewa-B4 at $T_{sat} = 5°C$ for R134a 76
6.9 Bundle falling film coefficient on Turbo-EDE2 at $T_{sat} = 5°C$ for R134a . . 77
6.10 Bundle falling film coefficient on Turbo-EDE2 at $T_{sat} = 5°C$ for R236fa . . 77

7.1 Film breakdown Reynolds number as a function of heat flux for each tube . 82
7.2 Falling film evaporation wet data on plain tube at $T_{sat} = 5°C$ 86
7.3 Falling film evaporation wet data on Gewa-C+LW at $T_{sat} = 5°C$ 87
7.4 Falling film evaporation wet data on Gewa-B4 at $T_{sat} = 5°C$ 87
7.5 Falling film evaporation wet data on Turbo-EDE2 at $T_{sat} = 5°C$ 87
7.6 $K_{ff,wet}$ vs q_o/q_{crit} on plain tube at $T_{sat} = 5°C$ 88
7.7 $K_{ff,wet}$ vs q_o/q_{crit} on Gewa-C+LW at $T_{sat} = 5°C$ 88
7.8 $K_{ff,wet}$ vs q_o/q_{crit} on Gewa-B4 at $T_{sat} = 5°C$ 88
7.9 $K_{ff,wet}$ vs q_o/q_{crit} on Turbo-EDE2 at $T_{sat} = 5°C$ 89
7.10 $K_{ff,wet}$ vs q_o/q_{crit} on Roques' database [3] 90
7.11 Local heat transfer coefficient, experimental vs. predicted on plain tube . . 92
7.12 Local heat transfer coefficient, experimental vs. predicted on Gewa-C+LW 92
7.13 Local heat transfer coefficient, experimental vs. predicted on Gewa-B4 . . 92
7.14 Local heat transfer coefficient, experimental vs. predicted on Turbo-EDE2 93
7.15 Local heat transfer coefficient, experimental vs. predicted on Roques' database [3] 93
7.16 Bundle effect 94
7.17 Prediction of the bundle heat transfer coefficient for a plain tube with R134a at $20kW/m^2$ 95
7.18 Prediction of the bundle heat transfer coefficient for a plain tube with R134a at $40kW/m^2$ 96
7.19 Prediction of the bundle heat transfer coefficient for a plain tube with R134a at $60kW/m^2$ 96
7.20 Prediction of the bundle heat transfer coefficient for a plain tube with R236fa at $20kW/m^2$ 96
7.21 Prediction of the bundle heat transfer coefficient for a plain tube with R236fa at $40kW/m^2$ 97
7.22 Prediction of the bundle heat transfer coefficient for Gewa-C+LW with R134a at $40kW/m^2$ (Tube 2) 98

7.23 Prediction of the bundle heat transfer coefficient for Gewa-C+LW with R134a at $60kW/m^2$ (Tubes 1 and 2) 98
7.24 Prediction of the bundle heat transfer coefficient for Gewa-C+LW with R236fa at $40kW/m^2$ (Tubes 2 and 3) 98
7.25 Prediction of the bundle heat transfer coefficient for Gewa-C+LW with R236fa at $60kW/m^2$ (Tubes 1 and 2) 99

List of Tables

3.1 Experimental test conditions 27

3.2 Properties of R134a and R236fa and their relative variation at $5°C$ 36

4.1 Measurements of the corrective multiplier of the water side coefficient for the plain tube. 50

4.2 Measurements of the corrective multiplier of the water side coefficient for the Gewa-C+LW. 51

4.3 Measurements of the corrective multiplier of the water side coefficient for the Gewa B4. 51

4.4 Measurements of the corrective multiplier of the water side coefficient for the Turbo-EDE2. 51

4.5 Corrective multipliers for internal heat transfer coefficient 52

4.6 Mean relative errors of the local heat fluxes with R134a 53

4.7 Mean relative errors of the local heat fluxes with R236fa 53

4.8 Mean relative errors of the local heat transfer coefficients with R134a . . . 53

4.9 Mean relative errors of the local heat transfer coefficients with R236fa . . . 54

5.1 Comparison of experimental results with existing correlation 57

5.2 Empirical coefficients for pool boiling at $T_{sat} = 5°C$ 62

7.1 Coefficients for the film breakdown correlation from Roques (Eq. (7.1)) . . 83

7.2 Coefficients for the film breakdown correlation from Ribatski (Eq. (7.2)) . . 83

7.3 Coefficients for the apparent wet fraction area F from Ribatski (Eq. (2.39)) 86

7.4 Coefficients for $K_{ff,wet}$ for the new database 89

7.5 Coefficients for $K_{ff,wet}$ for Roques' R134a-database [3] 89

7.6 Accuracy of the prediction method for R134a 91

7.7 Accuracy of the prediction method for R236fa 91

7.8 Empirical constants e, f and Re_{peak} for the plain tube 97

7.9 Empirical constants e, f and Re_{peak} for the Gewa-C+LW 99

7.10 Empirical constant B for the Gewa-B4 and Turbo-EDE2 tube bundle prediction 99

Nomenclature

Roman Symbols

A	area	$[m^2]$
C_i	Gnielinski multiplier	[-]
C_p	specific heat at constant pressure	[J/kg K]
C_{sf}	constant in Rohsenow correlation Eq. (2.23)	[-]
D	tube diameter	[m]
d_b	bubble diameter	[m]
d_d	droplet diameter	[m]
F	apparent wet area fraction	[-]
f	friction factor	[-]
f_b	bubble frequency	[Hz]
g	gravitational acceleration	$[g = 9.81 m/s^2]$
H	enthalpy	$[J/kg]$
h	local heat transfer coefficient	$[W/m^2K]$
H_{LV}	latent heat of vaporization	[J/kg]
k	thermal conductivity	[W/mK]
K_{ff}	falling film multiplier	$[-]$
L	characteristic length	[m]
L_d	developing length	[m]
$\dot{m}$	mass flow	[kg/s]
M	molar mass	[kg/kmol]
N	number of nucleation sites	$[-]$

P	tube pitch	[m]
p_r	reduced pressure	$[-]$
q	local heat flux	$[W/m^2]$
r_{cav}	cavity radius	$[m]$
R_p	peak roughness	$[m]$
r_{wall}	tube wall thermal resistance	$[K/W]$
R_{wall}	tube wall thermal resistance	$[m^2K/W]$
T	temperature	[K]
U	overall heat transfer coefficient	$[W/m^2K]$
u_g	vapor crossflow velocity	[m/s]

Greek Symbols

α	thermal diffusivity	$[m^2/s]$
β	volumetric thermal expansion coefficient	$[1/K]$
Γ	liquid film flow rate on one side of the tube per unit length	[kg/ms]
λ	wavelength	[m]
μ	dynamic viscosity	[Pa.s]
ν	kinematic viscosity	$[m^2/s]$
ρ	density	$[kg/m^3]$
σ	surface tension	[N/m]
ϕ	angle	[rad]
θ	critical angle	[rad]

Subscripts

b	boiling
c	convective
$crit$	critical
D	dangerous
d	developing
gni	Gnielinski

h	hydraulic (diameter)
i	internal side
imp	impingement
L	saturated liquid
o	external side
pb	pool boiling
r	(fin) root
ref	refrigerant
sat	saturation conditions
V	saturated vapor
wat	water

Dimensionless Numbers

Bo	Bond number, $Bo = g(\rho_L - \rho V)D^2/\sigma$
Ga	modified Galileo number, $Ga = \rho_L \sigma^3/\mu_L^4 g$
Nu	*Nüsselt* number, $Nu = hD/k$
Pr	Prandtl number, $Pr = C_p \mu/k$
Ra	Rayleigh number, $Ra = g\beta(T - T_\infty)D^3/\nu\alpha$
Re	Reynolds number, $Re = 4\Gamma/\mu$
We	Weber number, $We = \rho\sigma^3/\mu^4 g$

Chapter 1

Introduction

The environmental issues of ozone depletion and global warming have considerably affected the refrigeration, air-conditioning and heat pump industry over the last 10 years. The introduction of non chlorine-containing refrigerants and the development of new heat transfer concepts are necessary to achieve the goals of reduced energy consumption and environmental impact.

Shell and tube heat exchangers are widely used in the refrigeration industry, particularly for evaporators in large capacity units. In flooded evaporators, liquid refrigerant enters the evaporator from the bottom and evaporates as it moves up the tube bundle due to the buoyancy of the vapor. On the other hand, falling film evaporators are based on a heat transfer process that takes place when the refrigerant is flowing downwards, due to gravity, on the heated tube bundle. Applied to a refrigeration system, the falling film evaporator presents several advantages compared to a flooded evaporator, particularly in terms of higher cycle efficiency, reduced costs and a smaller environmental impact from its reduced charge of refrigerant. The pressure drop is small as the liquid flows only by gravity, which may imply the use of a recirculation pump to bring the liquid from the bottom to the top of evaporator. There are many parameters influencing the falling film evaporation process and, despite numerous studies, the basic mechanisms remain unclear, making the prediction approach mainly empirical. The main design parameters to correlate are the onset of dryout that can degrade the evaporator performance, and the heat transfer coefficient whose evolution can help to optimize the evaporator.

Bergles [1] documented the number of journal publications related to heat transfer enhancement technology over the years showing a rapid growth until the 1990s. Surface enhancement technology in recent years has been highly focused on the improvement of two-phase heat transfer with mechanically fabricated enhanced surfaces, thus providing high nucleation site density to trap vapor and optimize bubble generation. As underlined by Thome [2], the key fundamental problems regarding the physical processes and phenomena remain unsolved and investigators need to collect a large database to try to deduce how the structure of the surface affects the heat transfer performance.

The aim of the present investigation is to collect experimental data on falling film evaporation with plain and enhanced surfaces to better understand the mechanisms linked to two-phase flow and evaporation on a dense array of tubes in heat exchangers. The

LTCM falling film facility was designed and built in the previous studies of Roques [3] and Gstoehl [4]. Numerous results on a single-array (one row) were obtained with different heat fluxes and tube pitches. This study provides extensive new information on the behavior of structured surface for two different fluids; the facility was adapted for falling film heat transfer measurement in tube bundle (3-rows of 10 tubes each in the array). Local heat transfer coefficients were measured in single-array and in bundle configuration to obtain new heat transfer data. The new results were then used to develop new prediction methods for two-phase heat transfer and a new onset of dryout prediction method.

The thesis is organized as follow:

- Chapter 1: Introduction
- Chapter 2: State of the art review on falling film heat transfer
- Chapter 3: Description of the test facility modifications and instrumentation
- Chapter 4: Description of the data processing and measurement uncertainties
- Chapter 5: Analysis of the local heat transfer coefficients obtained in a single-row for plain and enhanced tubes
- Chapter 6: Presentation and discussion of the experimental results obtained for the tube bundle
- Chapter 7: Predictions methods for the onset of dryout and the local heat transfer coefficient in single-row and for the tube bundle
- Chapter 8: The conclusions of this study are summarized

Chapter 2

State of the art review

2.1 Hydrodynamics of a liquid film

According to a comprehensive state of the art review on falling film evaporation on horizontal tubes presented by Ribatski and Jacobi [5], the thermal performance of the falling-film heat exchanger may be drastically affected by the distribution of the fluid refrigerant along a tube bundle according to the following aspects:

- type of flow mode between adjacent surfaces,
- unsteadiness of the flow,
- film thickness along the heating surfaces,
- flow contraction along the tube bundle,
- spacing of droplet and column departure sites,
- “slinging” effect [6],
- film breakdown and hot patches.

The sections below discuss the status of some of these topics.

2.1.1 Falling film intertube modes and transitions

Instability mechanisms play important roles in falling film evaporation. Liquid film flows are usually dominated by viscous, gravity and surface tension effects. Circumstances may give rise to interfacial waves on the thin liquid film that may strongly affect the vaporization rate by increasing the interfacial area and enhancing convective transport near the interface.

When a liquid film flows from one horizontal tube to another below it, the flow may take the form of droplets, circular columns, or a continuous sheet. The droplet, column and sheet mode represent the principal flow modes. Droplet-column and column-sheet, that is, flow modes between the principal ones, have also been identified. A distinction is also made for the column mode according to the relative positions of the columns impinging and departing onto the top and from the bottom of the tube, respectively. The in-line column mode is defined when the columns are vertically aligned at the top and bottom. The staggered column is defined as that when the columns' positions are shifted from one intertube space to the following one, one-half λ out of phase. The thickness of a liquid film on the horizontal tube varies around the tube periphery since the gravity force component in the flow direction varies around the perimeter. Presently, circumferentially averaged heat transfer coefficient around the perimeter of the tube are considered in this study and can be termed to be "axially local" along the tube.

In a horizontal falling-film evaporator, the physical form of the liquid film depends not only on the liquid flowrate leaving the tube but also on the distance between the tubes as described by Jung et al. [7]. When the flowrate is small and the tube spacing large, the liquid flow is usually in a form of droplets at discrete points along the underside of the tube.

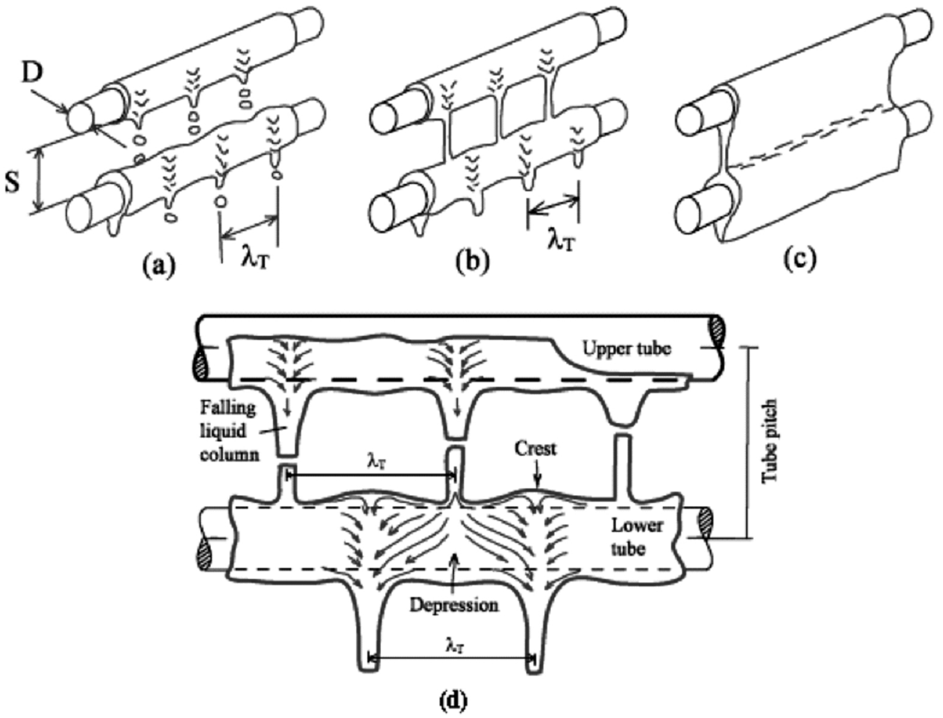

Figure 2.1: Intertube falling-film modes: (a) droplet mode; (b) column mode; (c) sheet mode; (d) illustration of the Taylor instability [8]

For the droplet and column flow modes, liquid usually falls from fixed sites along the underside of the tube. Fig. (2.1) shows some details of how the liquid film is formed. From the stagnation point of an oncoming column, the liquid flows along the tube in both axial directions. In the region when the spreading streams from the two columns overlap, a liquid crest is formed. The crest flows around the perimeter of the tube like a ring and the distance between them is related to the Taylor instability. For circumstances in which viscous effects are negligible and the fluid is incompressible, Bellman and Pennington [9] found that the critical wavelength and most dangerous Taylor wavelength are given respectively by:

$$\lambda_{crit} = 2\pi\sqrt{\frac{\sigma}{g(\rho_L - \rho_V)}} \tag{2.1}$$

$$\lambda_D = \lambda_{crit}\sqrt{3} \tag{2.2}$$

Only perturbations having wavelengths between λ_c and λ_D will grow. However, λ_D is the wavelength for which the disturbance grows most rapidly. Therefore, in real systems, the dominant disturbance wavelength is generally close to λ_D. Mitrovic [10] found departure-site spacing between the critical and the most dangerous wavelength, whereas Yung et al. [7], performing an experimental study with water, ethylene glycol and ammonia, concluded that λ is given by $\lambda_c\sqrt{2}$. Similar methods were developed by other authors, but Eq. (2.1) and Eq. (2.2) give good agreement based on simple expressions.

Flow modes of a liquid film falling on an vertical array of tubes depend principally on the flow rate and the physical properties of the liquid. Extensive studies focusing on the characterization and prediction of falling film intertube flow modes were performed by Hu and Jacobi [11] and, Armbruster and Mitrovic [12], on plain tubes, and recently by Roques et al. [13] on plain and enhanced tubes. Prediction methods for flow transitions were first proposed by Honda et al. [14] on a low finned tube and, recently, by Hu and Jacobi [11] on plain tubes and by Roques et al. [13] on plain and enhanced tubes, all for adiabatic conditions. Flow mode transitions were correlated as follows:

$$Re = aGa^b \tag{2.3}$$

where the film Reynolds number and the modified Galileo number are defined as

$$Re = \frac{4\Gamma}{\mu} \tag{2.4}$$

$$Ga = \frac{\rho_L \sigma^3}{\mu_L^4 g} \tag{2.5}$$

Comparing the current prediction methods for flow mode transitions, Ribatski and Jacobi [5] found a significant scatter among them, which is reasonable given the subjective nature of interpreting two-phase flow regime transitions.

The flow mode may be an important parameter in the optimization of falling film heat exchangers. The sheet mode seems to be the most convenient flow modes for falling film evaporation. This mode will best avoid the formation of dry patches on the heat transfer surface, although this may result in a waste of energy for pumping the excess liquid back to the distributor.

The effect of flow mode on the heat transfer performance will be discussed later.

2.1.2 Film breakdown and hot patches

If the flow rate of the liquid film is reduced sufficiently or if the amount of heat added to the surface is relatively high, the film will thin, break down and dry patches will appear. These dry patches on the tube surface result in a steep decrease in the heat transfer coefficient. A schematic of falling film breakdown is given in Fig. (2.2).

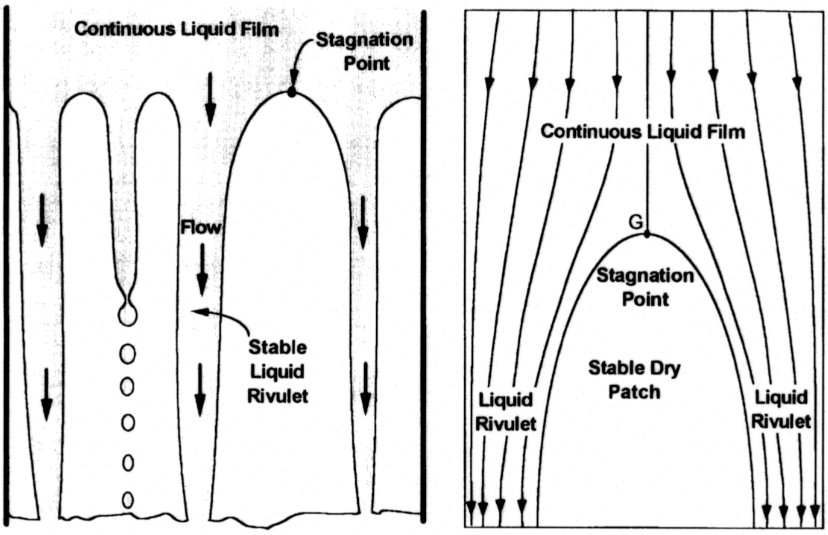

Figure 2.2: Schematic of a stable dry patch [15]

As described by Ganic et al. [16], the mechanisms and fluid forces involved in dry patch formation and its evolution are:

- the inertial force: the upstream liquid decelerates at the stagnation point which favors the rewetting of dry patches,
- the surface tension force: due to a nonzero contact angle between the liquid and solid surface, this helps to increase the dry patch size,
- the thermocapillary force (also called the Marangoni effect): a force resulting from the variation of surface tension due to the temperature gradient on the surface tends to transport liquid away from the thinnest location in the layer, inducing dry patches to form,
- the vapor thrust: the vapor creates a suction force around the liquid film which tends to enlarge the size of the dry patch,
- the interfacial shear force: the vapor entrains the liquid leading edge and tends to thin the liquid film, particularly for upward vapor flow.

In reality, the breakdown of a liquid film on a smooth heated tube appears to be mainly controlled by the surface tension phenomenon. A variation in film thickness due to waves leads to variation in the surface temperature. The thinner parts of the film (valleys) reach a higher interfacial temperature causing an even larger local variation of surface tension. The liquid will be drawn from the thin region of the film to the thicker parts (crests) and eventually local dry patches will appear on the surface when increasing the heat flux. These dry patches are usually observed beneath a crest at the lower part of the tube array. Ganic et al. [16] observed that some dry patches were not stable, sometimes re-wetting themselves.

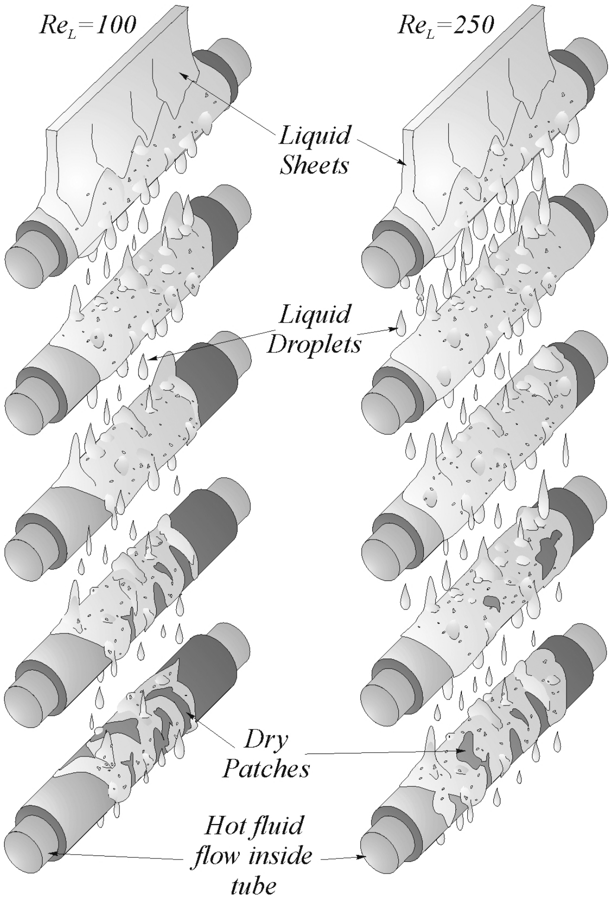

Figure 2.3: Schematic of liquid film breakdown from [8]

Fig. (2.3) from Thome [8] shows the observed liquid flow on a row of tubes for two different film flow rates, including flow contraction and intertube flow modes. This flow contraction was also observed and described by Fujita et al. [17]. They investigated breakdown of falling films with R-11 on plain tubes and defined a wetted area fraction ζ as a function of the heat flux, flow rate and tube location.

2.1.3 Vapor/liquid interaction

Compared to the intube vertical tube falling film configuration favored by the petrochemical industry, horizontal falling film evaporator design is considerably more vulnerable to vapor/liquid interaction. Reliable evaporator design requires a clear understanding of the effect of vapor crossflow. As a result of vapor crossflow, the droplets and columns falling from one tube may be partially or totally deflected away from the next tube, causing liquid redistribution and incomplete wetting of lower tubes with liquid leaving the array sideways. Entrainment mechanisms can also occur, as described by Yung et al. [7]:

- if nucleate boiling is present in the film, a mist of small droplets is generated as bubbles burst through the film and these small droplets are entrained in the flowing vapor,
- shearing or “stripping” of the liquid film from the tube surface,
- deflection of droplet/column due to the growth of instability waves for high vapor velocity as depicted in Fig. (2.4),
- liquid splashing depending of wettability and fluid velocity.

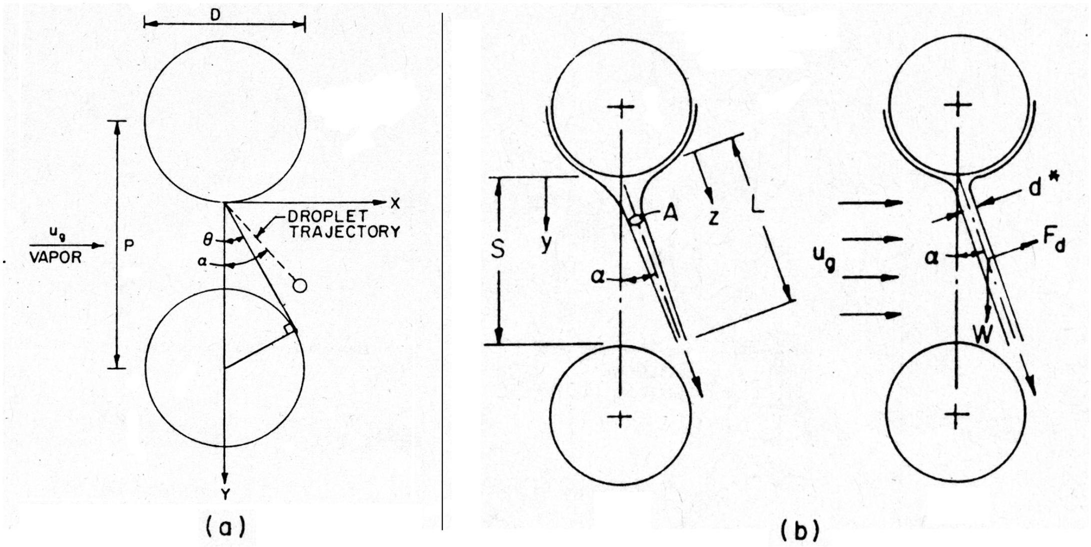

Figure 2.4: a) Droplet deflection due to vapor cross flow b) Column deflection due to vapor crossflow [7]

Yung and Lorenz [7] defined a critical angle $\theta_{droplet}$ beyond which the droplet will not hit the lower tube (see Eq. (2.6)). Based on the pitch-to-diameter ratio P/D and the critical deflection angle θ_{column} (see Eq. (2.7)), they solved the equations of motion of a single droplet to obtain the following two expressions:

$$\theta_{droplet} = \tan^{-1}\left(\frac{1}{2}\left[\frac{P}{D}\left(\frac{P}{D}-1\right)\right]^{-1/2}\right) \tag{2.6}$$

$$\theta_{column} = \tan^{-1}\left[\frac{1}{3}\frac{\rho_g}{\rho_l}\frac{u_g^2}{d_d}\right] \tag{2.7}$$

From Eq. (2.7) and Eq. (2.6), they obtained the maximum allowable vapor crossflow velocity u_g.

$$u_g = \left(\frac{3}{2}\frac{\rho_l}{\rho_g}d_d\right)^{1/2}\left[\frac{P}{D}\left(\frac{P}{D}-1\right)\right]^{-1/4} \tag{2.8}$$

They also conducted a similar but more complex analysis for the liquid column deflection, available in the cited article. They underlined the fact that this deflection of liquid does not necessary imply a loss of heat transfer performance, because the liquid may experience a good “hit”. In essence, good wetting on the tube is essential to ensure a good heat transfer performance and a well-controlled liquid flow is preferable to relying on random liquid hits on tubes in adjacent columns.

2.1.4 Tube bundle flow

With the formation of a horizontal gravitational liquid film on the surface of a horizontal circular tube, a non-stabilized flow practically always results since the main driving force is a projection of the gravitational force on the surface of the tube, which varies around the perimeter. This induces acceleration of the film on the upper part of the tube and deceleration on the lower part and in a such way it introduces momentum forces not accounted for in Nüsselt’s classic theory [18]. Additionally, momentum forces appear due to liquid impingement on the top of the tube and its run off. The hydrodynamic processes become more complicated for wavy or turbulent film flow on a vertical row of horizontal tubes with strongly developed vortex formation in the intertube spacing. For small intertube spacing, the surface tension forces will increase pressure 90° from the impingement area and decrease it in the intertube spacing, having a particular effect on the film thickness as described by Sinkunas [19]. Surface tension plays a significant role. Even when formally small, surface tension often has a significant smoothing effect preventing the formation of shocks (sharp jumps in the film thickness). Generally speaking, surface tension effects tend to flatten a film (to reduce curvature), thus producing a smooth film. This beneficial effect is limited where curvature variation is small [20].

The interfacial drag on the liquid film in a tube bundle is determined by the flow pattern in the space between the tubes. Significant accelerations and decelerations of the flow, characteristic to tube bundles, induce a drag effect on the flow. Consequently, the tube geometry and layout affect the drag. At low Reynolds numbers, the drag is represented by viscous friction and is directly proportional to the velocity. When the Reynolds number is increased, eddies are generated and cause a loss of kinetic energy in addition to the viscous friction, coupling the relationship between the velocity and the drag.

2.2 Heat transfer mechanisms

The hydrodynamic behavior of a fully developed isothermal falling film is retained also when heat transfer is superimposed on the flow, as long as film breakdown does not occur. For Rohsenow [21], the resistance to heat transfer resides in a thin thermal layer adjacent to the wall which is approximately equal to the residual film thickness. According to him, outside this thermal boundary layer, the mixing action of the interfacial waves leads to approximately a constant film temperature. For the case of saturated falling films, convective heat transfer leads to evaporation at the liquid-vapor interface. With an increase of heat flux, nucleate boiling occurs. It was reported that boiling occurs first on the lower side of the tube, near the downstream stagnation point. Vapor bubbles grow and are carried along by the film flow. Both thin falling film evaporation and nucleate boiling play a role in the heat transfer process, depending mainly on the heat flux and liquid mass flow rate.

Chyu and Bergles [22] defined three heat transfer regions illustrated on Fig. (2.5): the jet impingement region, the thermally developing region and the fully developed region.

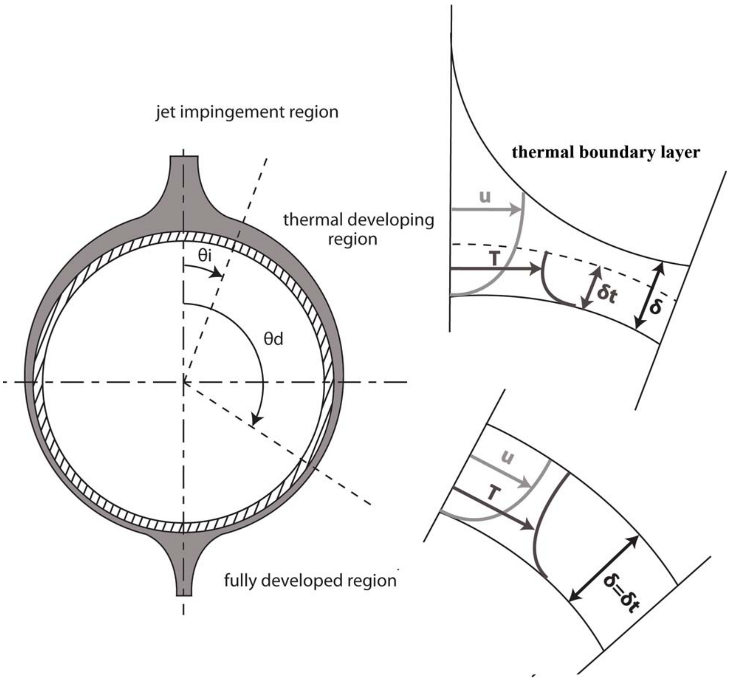

Figure 2.5: Falling film thermal regimes

The jet impingement region is a short region in which the heat transfer coefficient is relatively high due to liquid feed at the top of the tube. In the thermally developing region, the film is superheated from the uniform saturation temperature to a fully developed profile; all the heat transferred from the wall goes to superheating the liquid film and no evaporation occurs. In the fully developed region, all of the heat transfer goes to evaporation at the liquid/vapor interface if no nucleate boiling occurs within the film.

The convective and boiling heat transfer regimes have to be considered separately because the two heat transfer mechanisms are different.

2.2.1 Convection

Natural convection within the heat exchanger is due to local density gradients within the heat exchanger. At low flow rates these natural convection effects become evident. Although the liquid refrigerant is being propelled downward by gravity, some of the vapor in the heat exchanger moves on its own due to localized natural convection. When the tubes are hot, the vapor that comes close to the tubes is heated, becomes less dense, and displaces the nearby vapor that does not come into contact with the copper tubes. In this case, flow can be characterized as a combination of forced and natural convection.

Morgan [23], Churchill and Chu [24] and others have determined empirical correlation equations which focus mainly on the area and time-averaged Nüsselt number for natural convection. For an isothermal cylinder, Morgan proposed the following equation:

$$\overline{Nu} = \frac{\overline{h}D}{k_L} = CRa^n \tag{2.9}$$

For tabulated values of C and n, refer to [23]. Churchill and Chu recommended a single correlation for a wide range of Rayleigh numbers:

$$\overline{Nu} = \left(0.60 + \frac{0.387Ra^{1/6}}{[1+(0.559/Pr)^{9/16}]^{8/27}}\right)^2 \tag{2.10}$$

This equation is valid for $Ra \leq 10^{12}$ and is probably the most widely used for natural convection.

2.2.2 Nucleate pool boiling

The Rohsenow [25] correlation, to predict the heat transfer coefficient in nucleate pool boiling, was among the first to be recognized. According to Rohsenow, the high heat transfer rates associated to nucleate pool boiling are caused by bubbles departing from the surface. The resulting correlation has the following form:

$$Nu_b = \frac{hD}{k_L} = \frac{1}{C_{sl}} Re^{(1-n)Pr_l^{-m}} \tag{2.11}$$

C_{sl} as well as m and n are constants depending on different nucleation properties of a particular liquid/surface combination, while the Reynolds number was expressed using the superficial liquid velocity on the surface:

$$Re = \frac{q}{H_{lv}\rho_l}\left[\frac{\sigma}{g(\rho_l - \rho_v)}\right]^{1/2}\frac{\rho_l}{\rho_v} \tag{2.12}$$

Ishibashi [26] proposed a fairly simple correlation between heat flux and heat transfer coefficient for boiling of saturated water in narrow spaces in the form of

$$h \propto q^n \tag{2.13}$$

Stephan [27] recommended values of around 0.6 to 0.7 for n. In a previous study, Stephan et al. [28] proposed a correlation for several fluids including water, organics, refrigerants and cryogens:

$$h = 207\frac{k_l}{d_b}\left[\frac{qd_b}{k_l T_{sat}}\right]^{0.745}\left[\frac{\rho_v}{\rho_l}\right]^{0.581} Pr_l^{0.533} \tag{2.14}$$

In this correlation, the bubble diameter d_b was calculated according to Fritz [29]:

$$d_b = 1.192\phi_{contact}\sqrt{\frac{\sigma}{g(\rho_l - \rho_v)}} \tag{2.15}$$

Cooper [30] correlated the heat transfer coefficient with not only heat flux, but also reduced pressure, surface roughness and molecular weight. For boiling on horizontal plane surfaces, the heat transfer coefficient is given by:

$$h = 55Cp_r^{0.12-0.2log_{10}R_p}(-log_{10}p_r)^{-0.55}M^{-0.5}q^{0.67} \tag{2.16}$$

For boiling on horizontal copper cylinders, the constant C has to be chosen equal to 1.7. This correlation is probably the most widely used to accurately predict nucleate pool boiling heat transfer coefficients. It is valid for $0.001 \leq p_r \leq 0.9$ and $2 \leq M \leq 200$.

Gorenflo [31] developed a method for predicting nucleate pool boiling coefficients using a reference heat transfer coefficient h_0 obtained at reference conditions ($p_{r0} = 0.1$, $R_{p0} = 0.4\mu m$ and $q_0 = 20000W/m^2$). Knowing h_0, the heat transfer coefficient at other conditions is given by:

$$h = h_0 F_{PF}\left(\frac{q}{q_0}\right)^{nf}\left(\frac{R_p}{R_{p0}}\right)^{0.133} \tag{2.17}$$

The pressure correction factor F_{PF} was obtained by:

$$F_{PF} = 1.2p_r^{0.27} + 2.5p_r + \frac{p_r}{1-p_r} \tag{2.18}$$

and the index nf was given by:

$$nf = 0.9 - 0.3p_r^{0.3} \tag{2.19}$$

Boiling in a thin liquid film differs from its pool boiling counterpart. Falling film evaporation provides much higher heat transfer coefficients than pool boiling in the low heat flux, convective region. Cerza and Cernas [32] hypothesized that the enhancement to heat transfer from nucleate boiling in the liquid film is due to the fact that a bubble lies embedded in the superheated liquid film, compared to nucleate boiling where the bubble growth is generally confined to the thickness of the superheated thermal layer next to the wall.

2.3 Falling film enhancement

Numerous attempts have been made to improve the heat transfer performance by using enhanced surfaces. A great variety of enhancement techniques have been developed and applied to horizontal falling film evaporators: structured surfaces (porous metallic surfaces, knurled tubes), rough surfaces (ribbed or grooved tubes), extended surfaces (circumferential or helical fins)...

The general objective of these techniques is to reduce the size of the evaporator and increase the heat transfer efficiency by reducing the driving temperature difference. Typically, enhanced surfaces on the outside of tubes are for enhancing nucleate boiling, whereas those on the inside are for enhancing the heat transfer from the chiller water flowing inside. Refer to Bergles [33] and Thome [2] for comprehensive treatments of this subject.

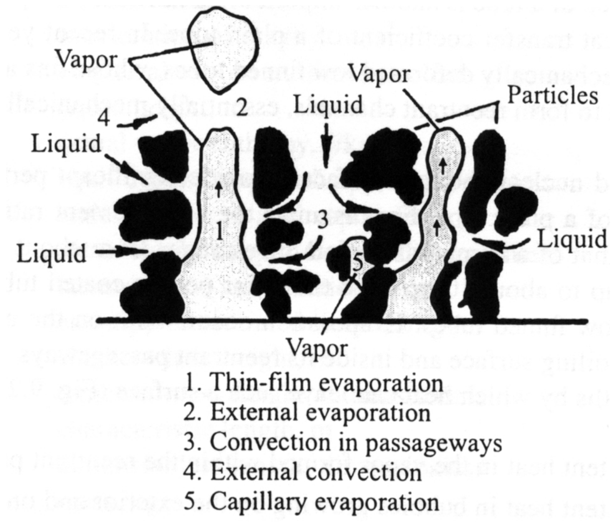

Figure 2.6: Evaporation processes on an enhanced boiling surface, from Thome [2]

The enhanced boiling process is different from normal nucleate boiling from cavities. Evaporation occurs both on the external surface and inside its reentrant channels. Thus, there are four possible ways for heat to be dissipated, as illustrated in Fig. (2.6):

1. As latent heat generating vapor within the reentrant channels,
2. As latent heat into bubbles growing on the outside surface of the enhancement,
3. As sensible heat to the liquid "pumped" through the reentrant channels and back out,
4. As sensible heat to the liquid in the external thermal boundary layer.

If enhanced surfaces were originally developed to improve nucleate pool boiling, they have only been applied to thin film evaporation since the 1980s. Structured surfaces promote nucleate boiling in the film at modest temperature differences, enhance turbulence within the film, and provide an increase in heat transfer area.

The parameters influencing the degree of enhancement are mainly the shape, geometry and surface area of the cavities and the nucleation site density while for porous coatings on surfaces the principal parameters are the particle size, the coating thickness and the porosity. Using the equation of Laplace and Clasius-Clapeyron, it can be shown that the wall superheat required for a bubble to exist at the mouth of a cavity of radius r_{cav} is given by:

$$T_{wall} - T_{sat} = \frac{q r_{cav}}{k_L} + \frac{2\sigma_L T_{sat}}{\rho_V H_{LV} r_{cav}} \tag{2.20}$$

The bubble departure diameter d_b can be calculated assuming the buoyancy force equals the surface tension force at the time of departure. The force balance gives:

$$d_b = C_b \left[\frac{2\sigma}{(\rho_L - \rho_V) g} \right] \tag{2.21}$$

The nucleation site density N/A was correlated by different authors as proportional to the heat transfer coefficient: $h \propto (N/A)^n$. Chien and Webb [34], [35] investigated the effect of pore diameter, pore pitch and tunnel shape using R11 and R123. They found there is a preferred pore diameter and pore pitch for a specific heat flux range. The main problem here is that the determination of the above parameters is extremely difficult and is purely empirical.

The behavior of structured surfaces is not well understood. As such, the point has not yet been reached where reliable methods are available to guide the custom design of the enhanced surface geometry for a particular fluid and operating condition. Poniewski and Thome [36] have recently proposed a new, free web book dedicated to the state-of-the-art of this topic.

2.4 Single tube and single tube row heat transfer studies

Falling film evaporation has been widely studied in terms of effects such as liquid feed flow rate, liquid distribution method, liquid feed flow pattern, liquid feed temperature, tube surface structure, surface aging, tube spacing, heat flux, surface subcooling, vapor cross flow, etc. Experimental data for boiling of thin films is relatively scarce when compared to the abundance of data for pool boiling. Much of the previous studies were made for Ocean Thermal Energy Conversion (OTEC) and desalination research on water. Unfortunately, only a few data are available for other working fluids, such as refrigerants.

2.4.1 Saturation temperature effect

In the convective evaporation regime (without nucleate boiling), authors like Fletcher et al. [37], Parken et al. [38] or Armbruster et al. [39] observed an increase of performance with increasing saturation pressure. This increase is related to the variation of viscosity with temperature and consequently to the film thickness. For the boiling regime, the effect of saturation temperature is not so clear. Zeng et al. [40] pointed out an increase in heat transfer coefficient, whereas Parken et al. [38] observed an opposite behavior for certain conditions. According to Ribatski and Jacobi [5], two competing effects can either increase or decrease the heat transfer coefficient: an increase of the activated nucleation site density with temperature and bubble growth inhibition due to a steeper temperature profile.

2.4.2 Heat flux effect

The effect of heat flux for the convective evaporation region was found to not affect the heat transfer performance by several authors like Fujita et al. [41] and Hu and Jacobi [42]. On the other hand, for nucleate boiling-dominated conditions, higher heat transfer coefficients are obtained for higher heat flux because of an increased nucleation site density as described by Moeykens [43] and Zeng et al. [40]. The variation of heat transfer coefficient with heat flux has been noted as particularly high for low reduced pressure fluids by Fletcher et al. [44].

2.4.3 Flow rate effect

Under stricly-convective evaporation conditions, two different behaviors were described in the literature: an increase of heat transfer performance with increasing flow rate as found by Ganic and Roppo [45] and non-dependence on the flow rate. For nucleate boiling-dominated conditions, the heat transfer coefficient becomes independent of the flow rate as noted by Chyu and Bergles [46] and Moeykens and Pate [43]. Roques [3]

proposed another heat transfer measurement strategy to obtain the local value at the midpoint of each tube, using a modified Wilson plot technique combined with measurement of the heating water temperature profile. According to him, the trend for falling film evaporation is made up of two distinct regions as shown on Fig. (2.7): a plateau corresponding to an all-wet nucleate boiling-dominated regime where the heat transfer coefficient varies little with the flow rate, a point of onset of dryout, and a partially-wet regime with nucleate boiling in the remaining film with a thus rapidly decreasing heat transfer coefficient tending towards the vapor phase natural convection coefficient at complete dryout. Hence, the onset of dryout is an important part of the heat transfer process and its modeling. Instead, once through hot water heating with tube-length averaged heat transfer coefficients with progressive dryout from one end to the other tend to give the monotonic trend illustrated in Fig. (2.7).

2.4.4 Tube diameter effect

The effect of tube diameter is related to the thermal boundary layer development and impingement region length relative to the “unwrapped” length $\pi D/2$. For non-boiling

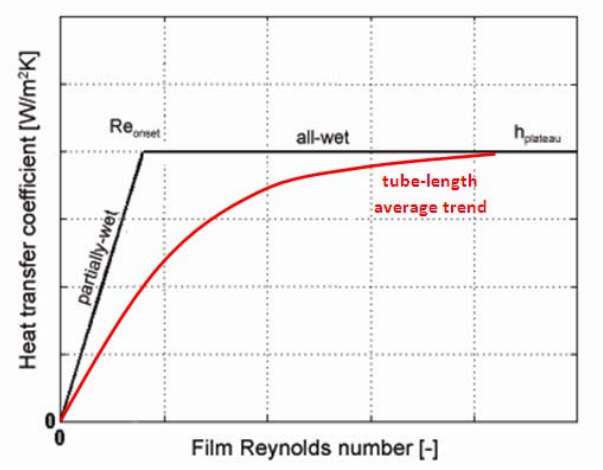

Figure 2.7: Schematic of the variation of heat transfer coefficient with flow rate for falling film evaporation

conditions, Parken and Fletcher [47] measured a higher heat transfer coefficient for smaller tube diameters. The respective proportion of the impingement region on the overall flow area increases with decreasing diameter giving higher performance. Such a noticeable diameter effect is not expected when nucleate boiling is dominant.

2.4.5 Liquid feeder effect

The configuration and the height of the liquid feeder above the top of the tube can affect the evaporator performance. A poorly designed or mal-situated feeder will cause a non-uniform axial uniformity of the liquid film and can lead to refrigerant maldistribution and premature formation of dry patches. Different liquid feeders were tested in the literature, such as perforated plates or spray nozzles, and the influence of their height on the impinging effect was studied.

Fletcher et al. [44] used a perforated plate instrumented with thermocouples at 3 locations around the tube to see the possible variation of circumferential temperature. They noted an axial temperature variation due to flow non-uniformity. Fujita and Tsutsui [48], [41] compared the heat transfer performance obtained for 3 different feeders: a sintered porous tube, a tube with nozzles and a plate with nozzles. They found that the porous sintered tube and the perforated plate with one, two or three dummy tubes performed 20% better than the cylindrical feeder with holes along the top. For Chyu et al. [49], the liquid flow rate given by nozzles depended on spray angle, nozzle height, nozzle interval, tube diameter, spray coverage and distribution of the liquid droplet within the spray coverage area. They analyzed different nozzle configurations to look at the spray coverage and the uniformity of the distribution. Moeykens and Pate [43] reported results for wide-angle low- and high-pressure-drop nozzles. The high-pressure-drop nozzles gave the best performance, probably because of a higher impingement effect. An increase of the feeder height resulted in higher impingement velocities which influenced the performance of the top tubes. It may also yield better uniformity of the spray and thus mitigate maldistribution effects.

The main disadvantage of the use of nozzles is that a significant portion of the liquid spray misses the top row of tubes, thus does not participate in the heat transfer. Also, the spray coverage from different nozzles intersect one another creating some nonuniformities within the liquid distribution. Large pressure drops in such nozzles also have an energy penalty. Roques [3] and Gstoehl [4] took special care in designing the liquid distributor described in Chapter 3 such that a stable and uniform liquid film fell along the top tube. They added a half tube below the liquid feeder to achieve a homogeneous liquid distribution along the test surfaces.

2.4.6 Vapor flow effect

Vapor flow can affect the heat transfer performance of a falling film evaporator in two opposite ways: on one hand, the vapor flow can create some maldistributions due to droplet atomization or column deflection, leading to partial dryout; on the other hand, it can promote waves within the liquid film and enhance the convective effect. The effect of vapor flow depends not only on its velocity but also on its direction. Rana et al. [50], working on air/water falling film heat transfer, reported that heat transfer in flowing air was 0.85 to 1.7 times that in quiescent air, depending on air velocity. For Armbruster and Mitrovic [39], flowing air, not saturated with vapor, can considerably increase the heat transfer due to evaporation at the surface and waves within the film.

Ribatski [51] studied the vapor shear effect of R134a falling film evaporation for enhanced and plain tubes. He noted that even for low vapor velocities, vapor flowing upwards can dramatically affect the liquid distribution and the heat transfer performance due to liquid hold-up. This trend was also observed by Danilova [52], who found that for countercurrent vapor flow the liquid film can become stagnant or even detach from the tube wall. For vapor flowing downwards, Ribatski [51] found an almost negligible effect of the vapor flow on the heat transfer coefficient. Hu and Jacobi [42] noted an increase of heat transfer coefficient with air velocity for co-current flow for convective evaporation without nucleate boiling, but this effect was within their uncertainty range.

2.4.7 Enhanced surfaces

Much work has been performed on pool boiling using enhanced surfaces. Surface modifications previously investigated include the use of porous structures and structured surface geometries (micro and macro). Each of these techniques has been shown to enhance heat transfer under certain conditions. The bubble growth mechanism on an enhanced surface is different from that on plain surface, because the liquid is mainly evaporated inside the tunnel for structured surfaces, while evaporation occurs on the microlayer for the plain tube.

Chien and Webb [34], [35] tested structured surfaces similar to Turbo-B using R11 and R123. They observed at low heat flux that tubes having smaller total open areas (sum of cavity areas) gave higher heat transfer coefficients while at higher heat flux, tubes having larger total open areas yielded higher heat transfer performance. They reported a cross-over characteristic of the boiling curves as shown on Fig. (2.8):

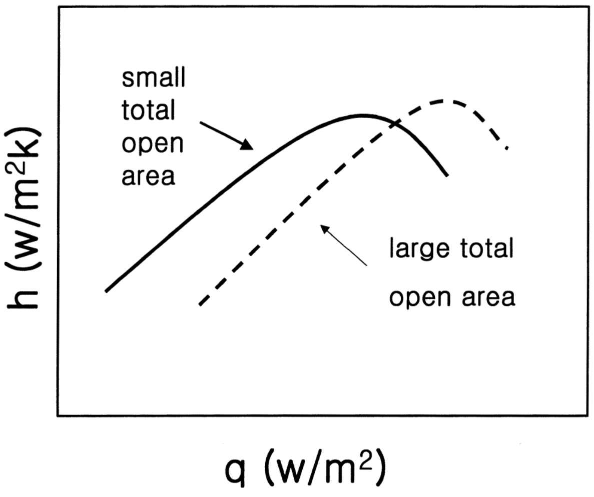

Figure 2.8: Cross-over characteristics of pored enhanced tubes as reported by Chien and Webb [34]

If the total open area is too large at low heat flux, the tunnel becomes flooded by the liquid and the heat transfer coefficient decreases. If the total open area is too small at high heat flux, the tunnel will dry out without enough liquid supply. The flow visualization study they made on these tubes [53] support this trend.

Moeykens et al. [54] observed that enhanced boiling surfaces give higher performance than finned tubes and lower performance than enhanced condensing surfaces used for evaporation. They noted an increase of heat transfer coefficient with heat flux reaching a maximum before then decreasing with any further increase of heat flux. This is probably caused by partial dryout.

Roques [3] tested 3 different enhanced surfaces: Gewa-B, Turbo-BII and High-Flux tubes. His data are for local circumferentially averaged heat transfer coefficients at the midpoint of his tube while other liquid heated data in other studies are tube length averaged, which may include dry zones somewhere along the length. He observed a similar trend for each surface and a strong dependance of the heat transfer performance with the heat flux. The High-Flux surface with its porous coating reaches performances up to 3 times higher than the other surfaces. The falling film multiplier K_{ff}, defined as the ratio between falling film evaporation and pool boiling heat transfer coefficients, gives values between 1 and 2 depending on the surface and the experimental conditions. In general, at low heat fluxes, falling film provides higher performance than pool boiling. This is probably related to enhanced convective effects of the falling film. At high heat fluxes, boiling is the dominating factor. The convective effect tends to disappear and the performances become comparable to those in pool boiling. The competition between these two effects depends on the surface structure.

Due to the highly complicated nature of the spray/surface interaction and the difficulty of making local heat transfer and film characteristics measurements on enhanced surfaces, a general explanation of the observed results cannot currently be given. Even on smooth surfaces, the mechanisms by which heat is removed during spray cooling is not well understood due to the difficulty to measure local film thickness, contact angle, nucleation site density, etc.

2.5 Tube bundle heat transfer studies

Assuming an ideal liquid flow, the falling film will be uniformly distributed within the bundle. However, according to several experimental studies, maldistributions, film breakdown and local dryout occur in a real bundle and affect the heat transfer performance.

According to Lorenz and Yung [55], the behavior of a tube bundle is complicated by the influence of intertube evaporation and turbulence generated as liquid falls from one tube to the next. They observed that the behavior of the top tubes is similar to that of a single isolated tube and concluded that the model for a single tube is directly applicable in this case. They found a fairly uniform heat transfer coefficient over the bundle cross section within ± 10% of the bundle-averaged value. According to them, vapor crossflow can be an important parameter, but with the relative small tube spacing in this study, the influence of turbulence may not have been significant. In view of this uncertainty, caution should be exercised when using results of single tube experiments to characterize the behavior of an entire bundle. For enhanced tubes, the potential improvement in performance resulting from these effects is relatively small. They also pointed out a critical Reynolds number of 300 below which the heat transfer coefficient of the bundle decreased compared to the single tube. This drop-off reflects the onset of the film breakdown and the feed of the lower tubes depends on the history of the fluid as it drips from tube to tube in the bundle due to a cumulative effect of evaporation vapor crossflow, flow nonuniformities and instabilities.

Chang and Chiou [56] designed a liquid film collector (see Fig. (2.9)) to prevent liquid droplets from bouncing from onto other heated tubes and thus delay the dry-out phenomenon. They compared the results obtained in pool boiling and spray evaporation with and without their collector and observed that, if at moderate heat fluxes both spray cases gave similar performance, at higher heat fluxes only the case with a liquid collector improves the heat transfer performance and could surpass pool boiling data. The maximum heat flux and the corresponding heat transfer coefficient exceeded by 30% that of the pool boiling data (see Fig. (2.10)).

The effect of the bundle layout on performance was investigated by different authors. Zeng et al. [57] investigated the tube bundle effect by comparing the performance given by triangular- and square-pitch bundles using ammonia. They observed that most of the interstices between tubes were filled with a liquid and vapor mixture moving downwards, and that there was no clearly defined liquid film flowing on individual tube walls. The space between tubes in a triangular-pitch bundle was narrower than that in a square-pitch bundle. The narrower flow passage made it more likely for the bubbles to be in contact with tube walls, therefore achieving higher heat transfer coefficients in a triangular-pitch bundle. Furthermore, the zigzag passages between tubes in the triangular-pitch bundle increased the chance for bubbles to impinge and to slide over tube walls. It was found that the triangular-pitch tube bundle also provides an advantage in terms of size reduction of the evaporator. The two phase flow pattern within a falling film tube bundle is similar

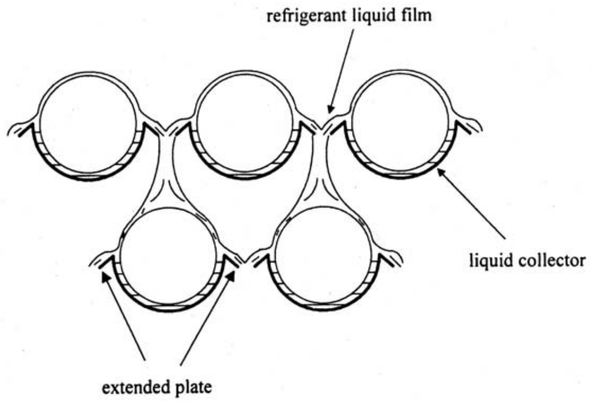

Figure 2.9: Schematic of a liquid collector with plain tubes from [56]

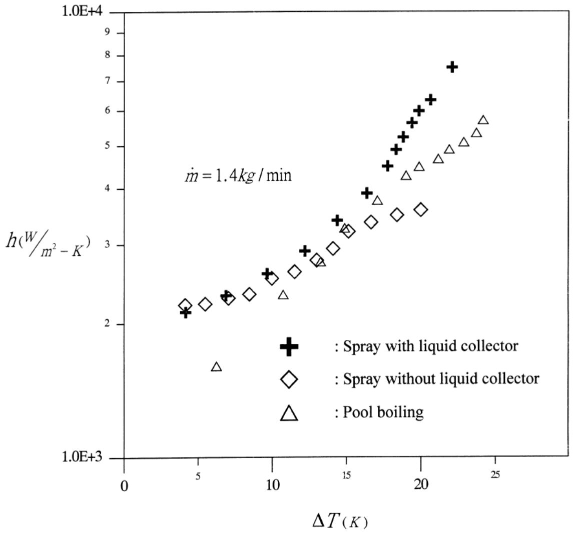

Figure 2.10: Comparison of the overall heat transfer coefficient with and without collector for R141b from [56]

to that within a tube bundle in pool boiling except that the flow direction is reversed. In pool boiling the direction of the two-phase flow is upwards due to buoyancy, while the flow direction is downwards in falling film evaporation due to gravity. In both cases, two-phase flow convection provides increased turbulence induced by bubbles impinging onto and sliding over the tube walls, as well as thin film evaporation on the tube wall as bubbles slide across them.

In a square-pitch bundle layout for falling film evaporation with nucleate boiling, Moeykens [58], [59] observed a higher performance in the first rows with R134a whereas they found an increase in heat transfer coefficient from row to row for R123. In the triangular-pitch arrangement, the liquid distribution tended to be less uniform and thus a larger variation from row to row was observed. Plain surfaces in the triangular-pitch bundle gave a decrease of heat transfer performance from row to row, particularly for high heat fluxes and low flow rates. He also noted that the heat transfer coefficient depended on the bundle overfeed ratio; too low of a bundle overfeed ratio could lead to a dramatic decrease of performance, apparently due to the formation of dry patches. By overfeed ratio, it was meant the actual flow rate relative to that if all the liquid ideally just finished evaporating when reaching the bottom. He also visually observed foaming within the liquid film, which seemed to increase the convective component of the overall heat transfer coefficient. These data were tube length averaged and hence might have included dryout effects at the end of the one-pass hot water heated bundle.

2.6 Falling film heat transfer models

Previous heat transfer studies on falling film evaporation have yielded various semi-empirical and empirical prediction methods. These methods take into account both convective and nucleate boiling components. In the literature, analytical predictions are mainly made for non nucleate boiling heat transfer only. One of the objectives of the current project is to develop an improved method to predict accurately the falling film heat transfer performance or update one of the existing models to fit the experimental data. This objective also tacitly means that a good method for predicting the onset of dry patch formation is required.

2.6.1 Smooth tubes

A simple model of combined evaporation and nucleate boiling of liquid films on horizontal tubes was developed by Lorenz and Yung [60]. They treated the case of a single horizontal tube by “unwrapping” the tube to form a vertical surface of length $L = \pi D/2$ and modeling the overall heat transfer coefficient as a superposition of the convective evaporation and boiling components:

$$\overline{h} = h_b + h_d \frac{L_d}{L} + h_c \left(1 - \frac{L_d}{L}\right) \tag{2.22}$$

The first term of Eq. (2.22) represents nucleate boiling over the entire length of the tube. The pool boiling correlation of Rohsenow was used to estimate h_b:

$$h_b = \frac{\mu h_{LV}}{C_{sf}^3 \sqrt{\frac{g_o}{g}\frac{\sigma}{\rho}}} \left[\frac{C_p}{H_{LV} Pr^{1.7}}\right]^3 \Delta T^2 \tag{2.23}$$

The other terms represent respectively convection in the thermal developing region and in the fully developed region. The average heat transfer coefficient in the developing region h_d was calculated from an energy balance giving:

$$h_d = \frac{3}{8} C_p \frac{\Gamma}{L_d} \tag{2.24}$$

The developing length L_d was estimated based on a constant film thickness given by Nüsselt theory, ignoring the effects of the bubbles within the film.

$$L_d = \frac{\Gamma^{4/3}}{4\pi\rho\alpha}\sqrt{\frac{3\mu}{g\rho^2}} \tag{2.25}$$

The average heat transfer coefficient for the fully developed region h_c was obtained from Chun and Seban [61] and their correlation for heat transfer to evaporate liquid films on smooth vertical tube is:

Laminar:

$$h_c = 0.821\left(\frac{\nu^2}{k^3 g}\right)^{-1/3}\left(\frac{4\Gamma}{\mu}\right)^{-0.22} \tag{2.26}$$

Turbulent:

$$h_c = 3.8 \times 10^{-3}\left(\frac{\nu^2}{k^3 g}\right)^{-1/3}\left(\frac{4\Gamma}{\mu}\right)^{0.4}\left(\frac{\nu}{a}\right)^{0.65} \tag{2.27}$$

This model uses Rohsenow's correlation, which requires the knowledge of a fluid-surface factor. This parameter is difficult to determine precisely and requires gathering a significant amount of pool boiling data. Another possibility would be to use an in-house pool boiling correlation instead of Eq. (2.23).

Two models were developed by Chyu and Bergles [46] for saturated non-boiling falling film evaporation. Both were based on the three heat transfer regions defined in section 2.2. The only difference between their models was in the fully developed region. The first model uses the correlations developed by Chun and Seban (see Eq. (2.26) and Eq. (2.27)) for fully developed film evaporation on a vertical tube, while the second uses a conduction solution based on Nüsselt's film condensation analysis as follows:

$$\overline{Nu}_{fd} = \frac{1}{\pi - \phi_d}\int_{\phi_d}^{\pi}\frac{sin^{1/3}\phi}{(A - \frac{4}{3}\int_{\phi_d}^{\pi} sin^{1/3}\phi' d\phi')^{1/4}}d\phi \tag{2.28}$$

with

$$A = \left[\frac{3\mu_l\Gamma^4}{g\rho_l(\rho_l - \rho_v)}\right]^{1/3}\left[\frac{H_{LV}}{Rk_f(T_w - T_{sat})}\right] \tag{2.29}$$

For both models, the average heat transfer coefficient was obtained by summing heat transfer contributions from each of the flow regimes:

$$\overline{h} = \overline{h}_s\left(\frac{\phi_s}{\pi}\right) + \overline{h}_{imp}\left(\frac{\phi_{imp} - \phi_s}{\pi}\right) + \overline{h}_d\left(\frac{\phi_d - \phi_{imp}}{\pi}\right) + \overline{h}_{fd}\left(1 - \frac{\phi_d}{\pi}\right) \tag{2.30}$$

The main limitation of this model is that it was developed for a non nucleate boiling condition and is not applicable when there is nucleate boiling in the film.

Prediction models and correlations developed from experimental data taken with refrigerants are fewer than those made from water studies. Fujita and Tsutsui [17] performed R-11 falling film evaporation tests on a plain tube bundle. Based on turbulent flow analysis they proposed the following correlation, which predicts their data to within ±20%.

$$Nu = (Re^{-2/3} + C_F Re^{0.3} Pr^{0.25})^{1/2} \tag{2.31}$$

The empirical constant C_F is equal to 0.008 for the tubes in the first row under the liquid feeder and 0.01 for the tubes in the other rows.

Roques [3] proposed a correlation to predict the falling film mutliplier $K_{ff} = h_o/h_{pb}$ for R134a as a function of the tube pitch P and heat flux:

$$K_{ff,plateau} = \left(1 + b_1 \frac{P}{P_o}\right)\left(b_2 + b_3\left(\frac{q_o}{q_{crit}}\right) + b_4\left(\frac{q_o}{q_{crit}}\right)^2\right) \tag{2.32}$$

In this equation, the tube pitch P is nondimensionalized with the minimum tube pitch tested, $P_o = 22.25mm$ and the heat flux q_o is reduced with the critical heat flux q_{crit} from Kutateladze's correlation:

$$q_{crit} = 0.131\rho_V^{0.5} H_{LV} \left(g\left(\rho_L - \rho_V\right)\sigma_L\right)^{0.25} \tag{2.33}$$

The main limitation of this method is the estimation of the empirical constant b_1, b_2, b_3 and b_4,which requires a large database of falling film evaporation measurements.

Chien and Cheng [62] proposed a new predictive model including bubble nucleation for 5 different refrigerants. They developed a superposition model inspired from the Chen model, where the nucleate boiling and the convective components are respectively weighted by a boiling suppression factor S and a two-phase enhancement factor E:

$$h = Sh_{nb} + Eh_{cv} \tag{2.34}$$

The S-factor was correlated as a function of Reynolds, Boiling and Weber numbers and the convective heat transfer coefficient h_{cv} was calculated by the Alhusseini et al. correlation [63]. For a plain tube, the proposed correlation is given by:

$$h = \left(0.185 + 56.2066\frac{We_F^{0.4531}}{Bo_F^{0.687} Re_f^{1.3078}}\right) h_{nb} + h_{cv} \tag{2.35}$$

This model predicts their plain tube data of R-11, R-123, R-134a, R-141b and R-22 within ±20% for plain tubes and ±33% for their Turbo B data.

More recently, Ribatski and Thome [64] developed a predictive method for plain tubes with R-134a to characterize both local dryout and non-dryout conditions. They defined an objective criterion to characterize the onset of dryout based on K_{ff}. The onset of dryout (i.e. formation of dry patches) was defined by a drastic decrease of the heat transfer coefficient with decreasing film flow rate and a decrease in the average heat flux, mathematically expressed by:

$$\frac{K_{ff,j} - \frac{1}{n}\sum_{j=1}^{n} K_{ff,j}}{\frac{1}{n}\sum_{j=1}^{n} K_{ff,j}} < -0.05 \tag{2.36}$$

This criterion was used to segregate the data as either being under partial dryout or non-dryout conditions. In this new method for partial dryout, the heat transfer area was divided into wet and dry regions respectively governed by nucleate boiling and vapor natural convection heat transfer. The local external heat transfer coefficient and heat flux were defined by:

$$h_o = h_{wet}F + h_{dry}(1 - F) \tag{2.37}$$

$$q_o = q_{wet}F + q_{dry}(1 - F) \tag{2.38}$$

where F represents the apparent wet area fraction defined as the ratio between the wet area and the total area.

Based on a regression analysis of the non-dryout data, a simple correlation of h_{wet} was obtained, based on a nucleate pool boiling expression such as $h_o = ap_r^b q_{wet}^c M^d Ra^e$. The values of h_{dry} were calculated using the Churchill and Chu's correlation [24] for [65] free convection assuming a quiescent vapor condition within the falling film evaporator. By combining Eq. (2.37) and Eq. (2.38), values of F can be backed out and correlated as function of the flow rate:

$$F = aRe_{top}^b \tag{2.39}$$

The method works reasonably well with 76% of data predicted within ± 30% for dryout conditions and 96% predicted within ± 30% for non-dryout conditions. The prediction method captures well the heat flux effect on the heat transfer coefficient and the onset of dryout. This method still needs to compared to a wider range of fluids and could be adapted to enhanced surfaces by using enhanced pool boiling models.

2.6.2 Enhanced surfaces

Nakayama et al. [66] proposed an analytical model to predict the performance of structured enhanced surfaces. They described 3 possible boiling mechanisms: the flooded mode, the suction-evaporation mode and the dried-up mode. In their model, the boiling mechanism within porous matrices was assumed as suction-evaporation. Nakayama et al. assumed that the total heat flux from an enhanced surface is expressed as $q = q_{tun} + q_{ex}$ where:

1. The tunnel heat flux q_{tun} due to thin-film evaporation inside the tunnels of the structured surface is:

$$q_{tun} = (N/A) f_b H_{LV} \rho_V (\pi d_b^3/6) \tag{2.40}$$

2. The sensible heat flux q_{ex} due to the external convection induced by bubble agitation is:

$$q_{ex} = (\Delta T/C)^{1/y} (N/A)^{-x/y} \tag{2.41}$$

Hence, they have introduced two of the four mechanisms identified in Fig. (2.6). A, N, f_b and d_b represent, respectively, the base area of the surface, the number of active nucleation sites, bubble formation frequency and the departure diameter. C, x and y have to be determined through a separate series of experiments. All these parameters are extremely difficult to estimate.

They also proposed a dynamic model of bubble growth and departure, dividing the bubble cycle into three phases:

1. The pressure build-up phase due to evaporation of liquid held in the corner of the tunnel, until the meniscus at the cavity reaches a hemispherical shape. The pressure in the tunnel then reaches its maximum,
2. The pressure reduction phase as the vapor flows into the growing bubble,
3. The liquid intake phase when a pressure depression occurs in the tunnel, draining fresh liquid into the tunnel through the inactive nucleation sites.

Ayub and Bergles [67] followed the same approach as Nakayama assuming that the total heat flux was the sum of the external heat flux q_{ex}, defined by Eq. (2.41), and the latent heat flux calculated using:

$$q_L = Ck(T_{wall} - T_{sat}) \tag{2.42}$$

C is a constant to be determined experimentally.

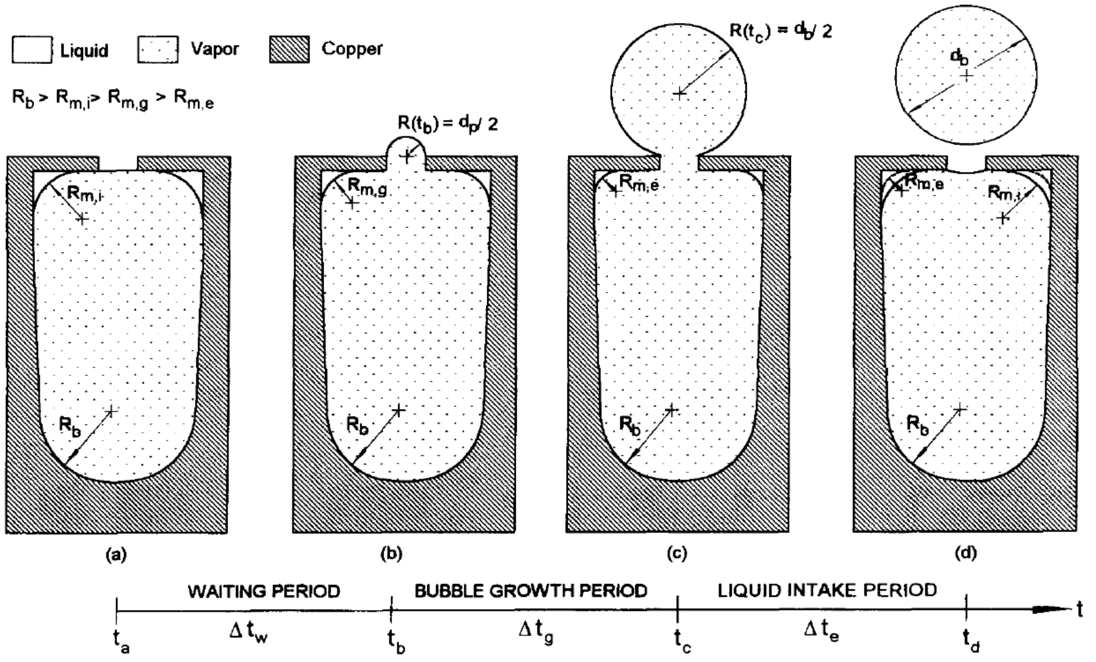
Liquid
Vapor
Copper
$R_b > R_{m,i} > R_{m,g} > R_{m,e}$
$R(t_b) = d_p/2$
$R(t_c) = d_b/2$
d_b
$R_{m,i}$
$R_{m,g}$
$R_{m,e}$
R_b
(a)
(b)
(c)
(d)
WAITING PERIOD
BUBBLE GROWTH PERIOD
LIQUID INTAKE PERIOD
t_a
Δt_w
t_b
Δt_g
t_c
Δt_e
t_d
t

Figure 2.11: Process of evaporation inside subsurface tunnel: Bubble growth and departure from [68]

Webb and Chien [68] proposed a semi-analytical model for nucleate boiling based on flow visualization on an enhanced surface with a circular fin base. The model also assumes a 3-period bubble cycle similar to the one of Nakayama: the waiting, bubble growth and liquid intake period as shown on Fig. (2.11). They formulated the size of the departing bubble d_b by writing a force balance on the bubble:

$$d_b = \left[\frac{Bo + \sqrt{Bo^2 + 2304(96/Bo - 3)}}{192 - 6Bo} \right]^{1/2} \tag{2.43}$$

The authors then describe a prediction method involving a set of 11 equations to estimate total heat flux, bubble departure diameter and bubble frequency.

Most of the existing falling film evaporation models and enhanced boiling models are difficult to apply in practice because they require parameters extremely difficult to measure experimentally to finalize the model. For these reasons, in this study, only an empirical approach will be used and the methods developed at LTCM by Roques and Ribatski will be considered as a first reference.

Chapter 3

Description of experiments

The existing LTCM falling film refrigerant test loop has been modified and adapted to the new test conditions and measurement methods. One new test section setup was built for bundle evaporation tests. The present configuration allows tests to be run under diabatic conditions in pool boiling mode and falling film evaporation mode on single tube rows and with a bundle of 3 tube rows. All modifications have been made on the original test facility developed by Roques [3] and Gstoehl [4].

3.1 Falling film test facility

The objective of the experimental part of this study was to run falling film evaporation tests over a wide range of experimental conditions. The objective was to obtain accurate values of local heat transfer coefficients on a tube array (one vertical row of horizontal tubes) and on a bundle (three vertical rows of horizontal tubes) for different tube surfaces. The existing test facility had to be modified to run evaporation tests on the 3x10 tube bundle with an industrial tube layout. Two new circuits were built to create the liquid overfeed on the side columns and to heat the two side tube rows. The test section was also adapted to fit the new tube layout and to connect all these tubes together.

The ranges of experimental conditions tested are shown in Table 3.1.

Conditions	Pool Boiling	Falling Film Evaporation
Test fluids	R134a, R236fa	R134a, R236fa
Tube layout	1 tube	1×10 and 3×10
Saturation Temperature	5, 10 and $20°C$	$5°C$
Local Heat Flux	20-60 kW/m^2	20-60 kW/m^2
Internal Reynolds Number	$6000-16000$	$6000-16000$
Liquid Film Flow Rate	$-/-$	20 to 250 $g/m.s$

Table 3.1: Experimental test conditions

The test facility consists of a natural circulation loop for the refrigerant and a forced circulation loop for the heating water. In order to avoid pump vibrations and simplify construction, the test facility was divided into two units. First, the main unit with the refrigerant circuit includes the evaporator, the test section and the overhead condenser as depicted in Fig. (3.1). Second, the auxiliary units includes pumps and heat exchangers for conditioning the heating and cooling fluids for the test section, and the glycol for the auxiliary condenser. Detailed descriptions of these circuits will be given in the following subsections.

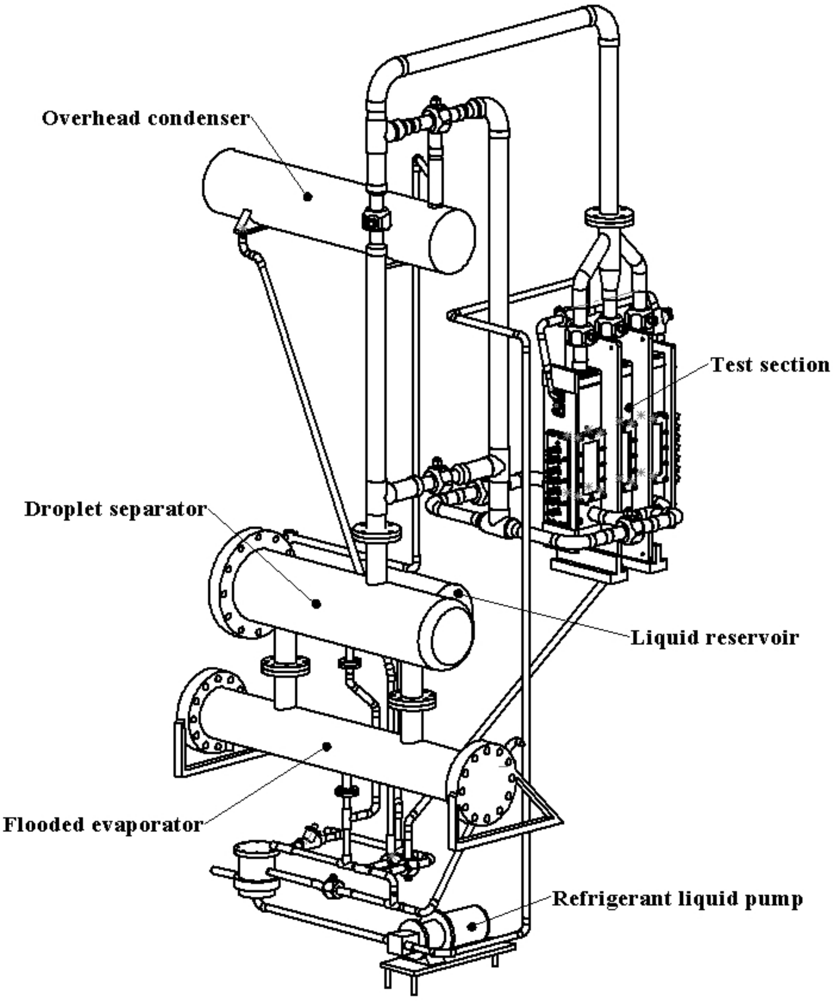

Figure 3.1: 3-D Solidworks drawing of the falling film facility

3.1.1 Refrigerant circuit

The refrigerant circuit is the main circuit of the test facility. It comprises an electrically heated evaporator to maintain the desired saturation condition, an auxiliary condenser to create the vapor flow in the test section and the test section itself. As the test facility is designed for multiple purposes, various pipe connections were made between these three basic elements. The operating mode can be chosen by opening and closing the valves in the circuit to set the path for the vapor and liquid flows. For a detailed diagram showing all piping in the refrigerant circuit, see Roques [3]. In the present investigation, the capability of the test facility was only partially used. The manner in which the vapor and liquid refrigerant loop were used in the present study is described below.

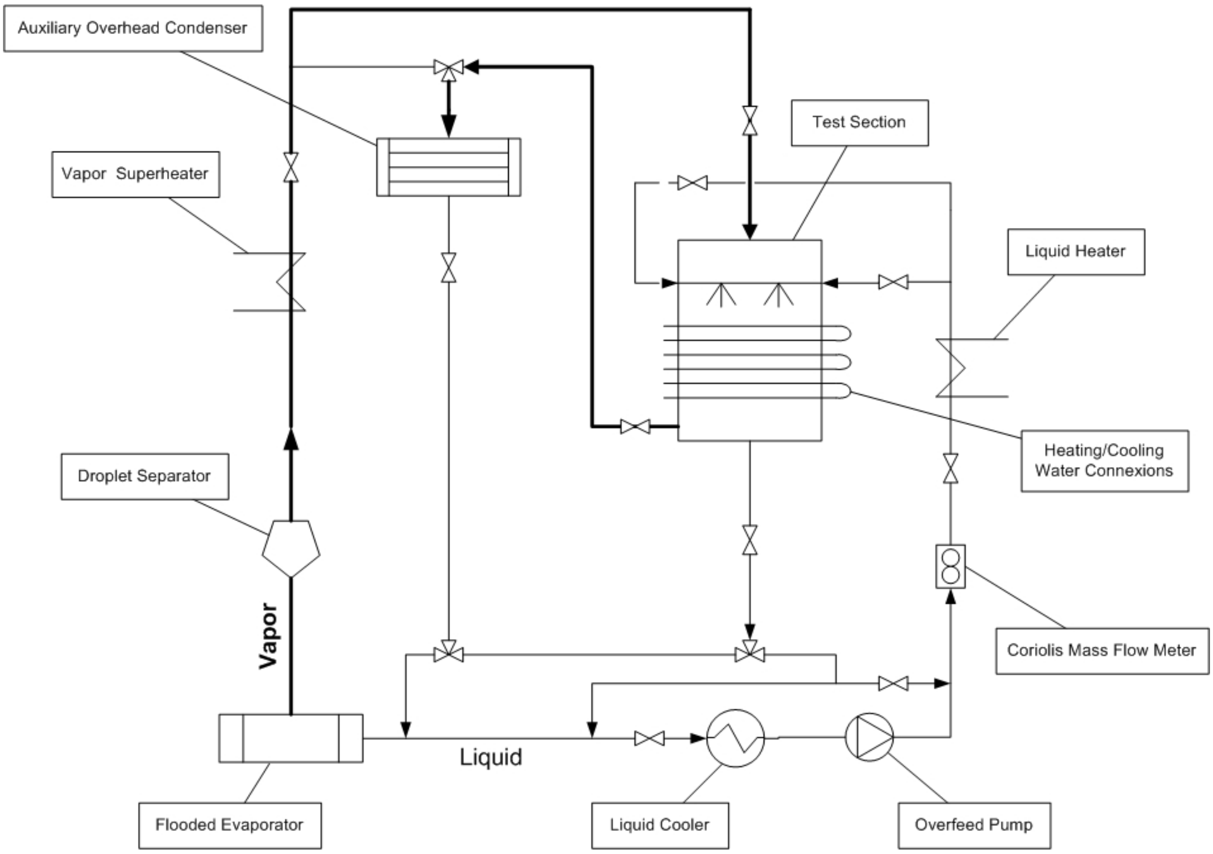
Auxiliary Overhead Condenser
Vapor Superheater
Test Section
Liquid Heater
Heating/Cooling Water Connexions
Droplet Separator
Coriolis Mass Flow Meter
Vapor
Liquid
Flooded Evaporator
Liquid Cooler
Overfeed Pump

Figure 3.2: Schematic of the falling film evaporation refrigerant circuit

During operation, most of the liquid is in the flooded evaporator, which acts as a liquid reservoir in the circuit. Starting from this flooded evaporator, the refrigerant flows through the subcooler to the magnetically driven gear pump (self-lubricating without oil). The pump is frequency controlled. The filter removes any particles from the liquid refrigerant and also contains a refrigerant drying cartridge. The subcooler is used at the pump entrance to avoid cavitation. Bypass piping is also installed together with a frequency controller and achieve the desired liquid flow rate. For very low flow rates, in order to avoid oscillations, the bypass is opened rather than using very low frequencies with the gear pump. There is then a vibration absorber, a coriolis mass flow meter, and an electric heater to bring the liquid back close to the saturation conditions at the test section inlet. At this point, the liquid enters the test section and has to be distributed uniformly on the heated tubes. Special care has been taken to achieve this distribution; the liquid distributor is detailed in section 3.2.1. Once the liquid leaves the distributor, it falls on top of the heated tubes where it is partially evaporated and the residual liquid leaving the test section flows via gravity back to the flooded evaporator. The vapor refrigerant circuit is a natural circulation loop. The vapor is evaporated in the lower part of the circuit and condensate is formed in the upper parts. The liquid flows back from the auxiliary condenser to the flooded evaporator by gravity. The test facility offers three different possibilities for the vapor flow: downwards, upwards, and quiescent vapor flow.

This last mode was chosen for use in this study because in this mode, the vapor leaves the test section very slowly with very little vapor shear effect.

3.1.2 Water circuit

The heating water flowing inside the test tubes is cooled down in the test section and heated back up in the auxiliary unit. This forced-circulation loop for the heating water is illustrated in Fig. (3.3).

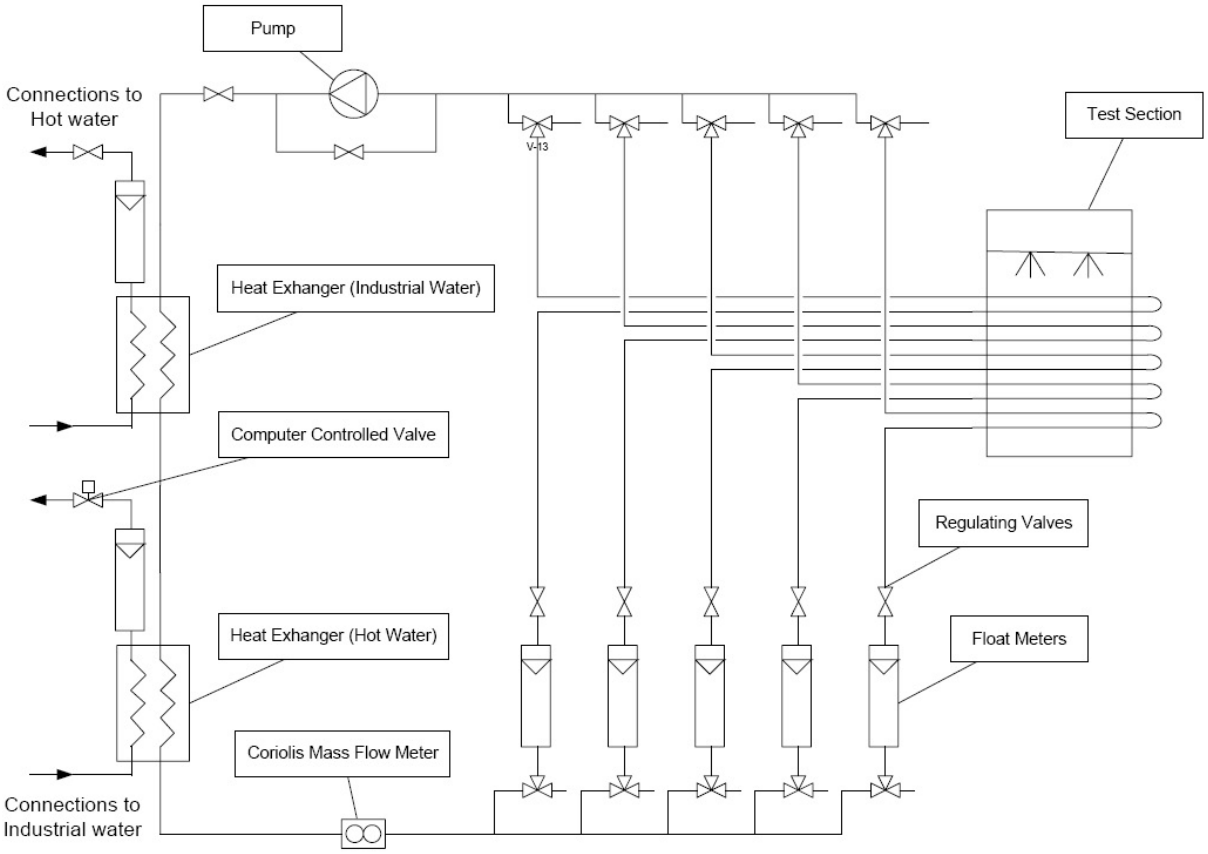
Pump
Connections to Hot water
V-13
Test Section
Heat Exhanger (Industrial Water)
Computer Controlled Valve
Regulating Valves
Heat Exhanger (Hot Water)
Float Meters
Coriolis Mass Flow Meter
Connections to Industrial water

Figure 3.3: Schematic of the forced-circulation loop for the heating water

The circuit is equipped with a centrifugal pump. An electronic speed controller together with a bypass and a valve allows good precision in the mass flow adjustment. After the pump, the water goes into the first liquid-liquid heat exchanger. In this heat exchanger, the test section water exchanges heat with industrial water. This is water from Lake Geneva, available in the laboratory at a very constant temperature of about $7°C$. The cooling capacity of the exchanger is set by adjusting the mass flow rate of the industrial water. The test section water then flows through a second liquid-liquid heat exchanger where it can be heated with hot water from a heating unit. The heating unit available at the laboratory is gas fired and can provide hot water with adjustable temperatures ranging from $40°C$ to $90°C$ with a maximum capacity of $160kW$. The heat exchanged in this heat exchanger is controlled by the flow rate of the hot water. An electronicallyactuated, computer-controlled valve sets this flow rate, based on the test section water temperature at the outlet of the heat exchanger. The water temperature at the test section inlet is thus automatically maintained constant when the flow rate is changed or if there are any temperature variations in the water provided by the heating unit. At this point, the water for the test section is well conditioned in terms of stability of its temperature and flow rate. The total mass flow rate is finally measured with a Coriolis mass flow meter.

The main flow of water is then split to the sub-circuits of the test section. Each sub-circuit has its own float flow meter and valve to control its flow rate and thus set the water distribution uniformly between the sub-circuits. The goal is to achieve the same flow rate in all sub-circuits. There are five sub-circuits and each one can be included in the main circuit (or not) with two three-way valves for each. A sub-circuit usually has two tube passes, i.e. water goes in a copper tube in one direction and comes back through the copper tube just above in the opposite direction within the test section. With this setup, the water temperature profiles in the two tubes are opposed. The quantity of liquid refrigerant evaporated after each two tubes in the test array is thus nearly uniform along the tube length. Tests in other published projects often use only one water pass, which creates a significant heat flux variation along the tubes, which in turn creates an imbalance in the axial liquid film distribution and hence make those data dependent on the test setup, which is to be avoided. After the test section, the sub-circuits merge and the water flows back to the pump.

3.1.3 Glycol circuit

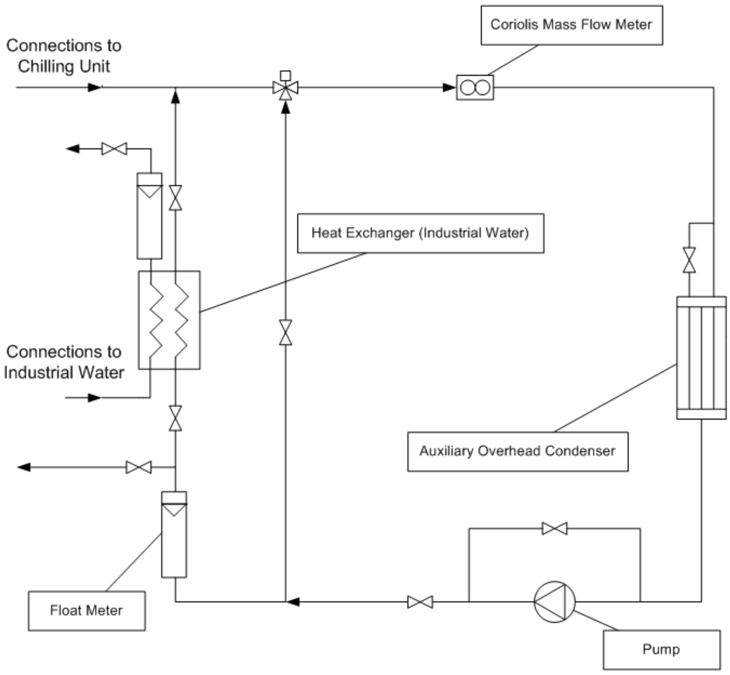
Coriolis Mass Flow Meter
Connections to Chilling Unit
Heat Exchanger (Industrial Water)
Connections to Industrial Water
Auxiliary Overhead Condenser
Float Meter
Pump

Figure 3.4: Schematic of the forced-circulation of glycol

Glycol is used as a cold source for the auxiliary condenser of the test facility. The glycol is heated up when it passes through the auxiliary condenser and has to be cooled in the auxiliary unit. The circulation loop of glycol is depicted in Fig. (3.4).

The circuit is equipped with a centrifugal pump. An electronic speed controller together with a bypass line and a valve are used for the glycol mass flow adjustment. After the pump a part of the glycol passes through a float meter to a liquid-liquid heat exchanger. In this heat exchanger the glycol is cooled by industrial water. As the industrial water is at constant temperature, the cooling capacity of the heat exchanger is set by adjusting the mass flow of industrial water by a hand valve. The cooled glycol leaving the heat exchanger flows to the motorized three-way valve. In this valve the cold glycol is mixed with the other part of glycol that did not pass through the heat exchanger to obtain the desired temperature. This recirculation allows fine adjustment of the glycol temperature. The glycol mass flow is then measured by a Coriolis flow meter. The conditioned glycol goes then to the auxiliary condenser, which is a three-pass condenser with a design capacity of $50kW$. It is possible to use only one half of the tubes in the condenser to have a good power adjustment accuracy over a wide operating range.

For very low glycol temperatures and very high thermal capacity of the auxiliary condenser, the glycol loop has the capability to use a chilling unit as a cold source. In this case, the valve at the inlet to the heat exchanger is closed and the glycol passes to the chilling unit. In this configuration the recirculation can also be used for fine adjustment of the temperature. The chilling unit available in the laboratory can provide glycol at $-20°C$ and has a maximum continuous cooling capacity of $80kW$.

3.2 Test section

The test section is a rectangular stainless steel vessel (554x650x69mm) illustrated in Fig. (3.5). The tested tubes have a standard nominal outside diameter of 19.05mm (3/4in), and the removable end plates (1) holding the tubes at the two extremes of the test section allow different tube layouts to be used. Depending on the tube pitch, 6 to 10 tubes can be tested in a vertical array of horizontal tubes, and a maximum of 30 tubes can be reached in a bundle configuration. The active tube length from plate to plate is 554mm.

The refrigerant vapor enters the test section through 3 inlets at the top (3) and the generated vapor leaves the test section by 4 outlets (5) at the bottom. Two outlets are located on the front and two on the rear of the test section. The vapor velocity in the test section is always below 1m/s. To investigate the onset of dry-out and the effect of the liquid film flow rate on the tube performance, the test section is equipped with a system to distribute the liquid refrigerant onto the first tube. The liquid refrigerant enters the liquid feeder (2) from two inlets located on each side (5). The direction and uniformity of the liquid film can be adjusted visually using hand valves located on both inlets. The excess liquid leaves the test section by gravity through an outlet on the bottom of the test section.

The test section is equipped with 6 large windows (3), three on the front and three on the rear, to get full visual access inside the test section and observe the fluid flow on the

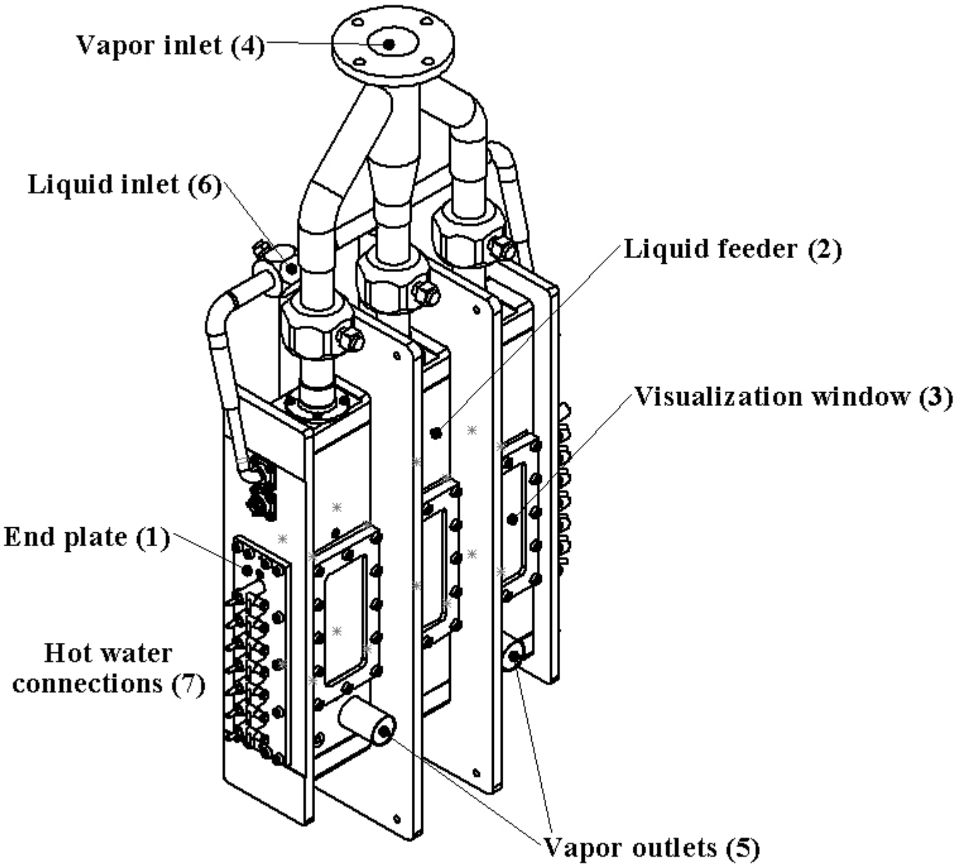

Figure 3.5: 3-D Solidworks drawing of the test Section

tubes.

3.2.1 Liquid distribution

As the liquid distribution is a key parameter for falling film heat transfer, special care has been taken to achieve very uniform distribution of liquid refrigerant along the tubes. The distributor designed for this purpose is a rectangular box (554x200x20mm) positioned in the test section above the tubes. A cross sectional schematic of the liquid feeder is given in Fig. (3.6). This liquid feeder has two main purposes:

- To distribute the nearly saturated liquid refrigerant uniformly along the top tube,
- To mimic the flow of an upper tube onto the top tube.

The liquid refrigerant enters on both sides at the top and is pre-distributed with a 13mm internal diameter stainless steel pipe in which there are holes oriented upwards (1). The holes are 3mm in diameter and spaced 5mm center to center. Then the liquid flows through two layers of foam material compatible with R134a and R236fa. The first is a 150mm-tall layer of soft foam material (2). This is a polyurethane foam with a pore

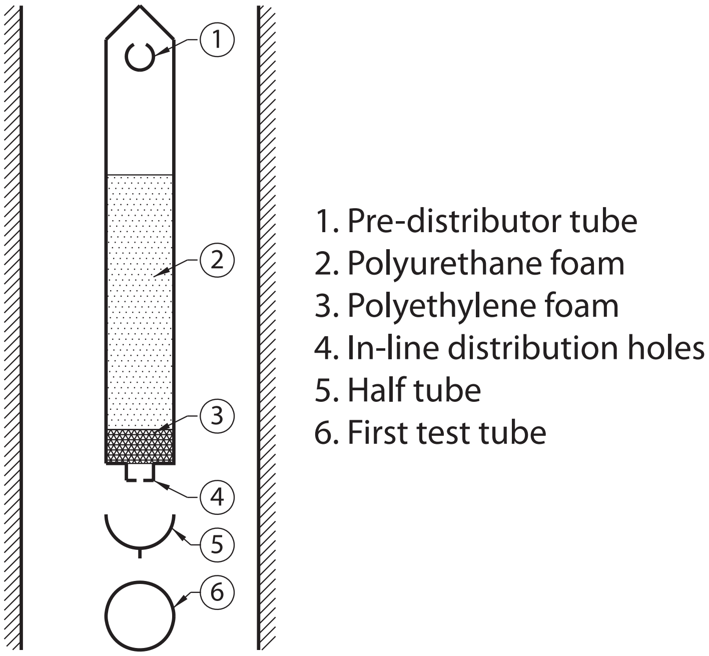

Figure 3.6: Schematic of the liquid distributor

diameter of $200\mu m$ and 60 pores per inch. The second is a 10mm-tall layer of a filter plate (3), which is a polyethylene foam material with a pore diameter of $35\mu m$ and a porosity of 37%. This second layer is more compact and creates a larger pressure drop to force a good lateral distribution of the liquid. After this porous section, the liquid reaches the bottom of the distributor, which is a removable machined brass piece with 268 holes along its centerline (4). The diameter of these holes is 1.5mm and the distance center to center is 2mm. The liquid distributor width is 550mm. At high liquid flow rates a continuous sheet leaves the distributor, but at low flow rates the distribution of the droplets is not uniform. For this reason a half-tube was added just below the distributor (5). It was machined from a plain stainless steel tube 20mm in diameter. The bottom of the half tube was machined to form a sharp edge. The liquid falls locally along in the half-tube and overflows on both sides. The sharp edge forces the liquid to leave at the bottom of the half tube. By rotating the half tube, the direction of the liquid leaving the tube at the edge can be adjusted to ensure that the liquid falls exactly on the center of the top of the first test tube (6). The temperature of the overfeed liquid is controlled by a heater to maintain its subcooling to less than 0.8K.

3.2.2 Tube layout

Two different tube arrangements have been tested in this study: a 10-tube array (1×10) and a 30-tube bundle (3×10) as shown on Fig. (3.7). The dimensions and layout used for this study corresponds to those recommended by the industrial sponsors of the project. The tube pitch center-to-center was 7/8" (22.3mm), allowing ten tubes to be installed.

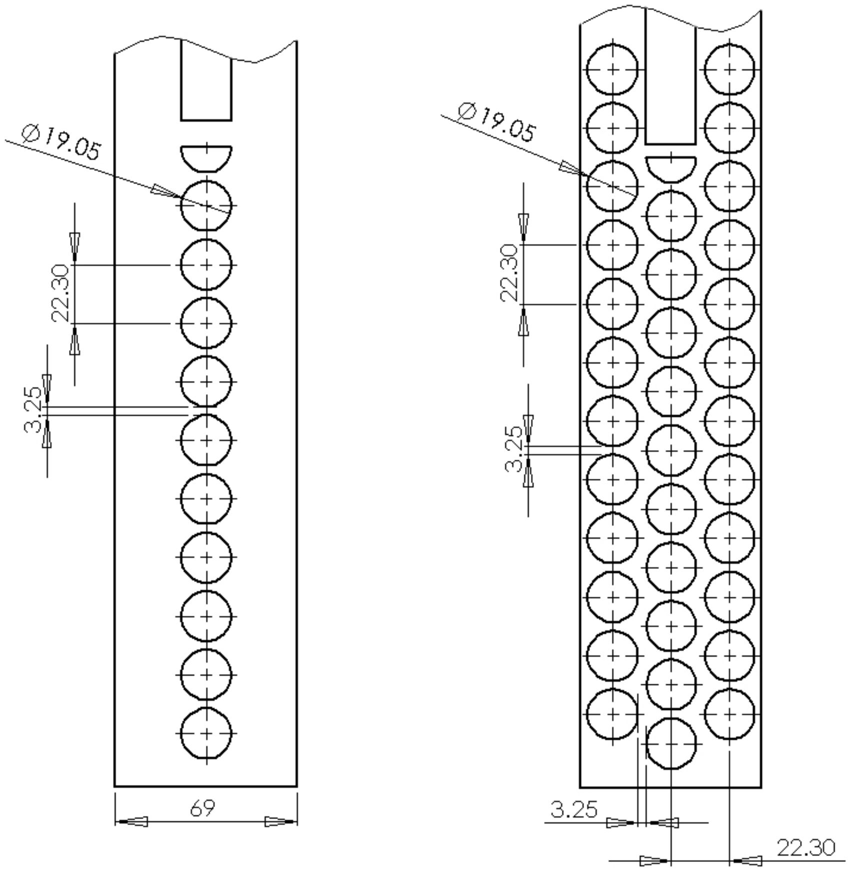

Figure 3.7: Tube array and bundle layout

With a nominal tube diameter of 3/4" (19.05mm), intertube spacings of 3.25mm are obtained. The bundle tests were conducted with triangular-pitch tube bundle. Vertical and horizontal pitches were also chosen to be 7/8" (22.3mm).

3.3 Refrigerants

Many factors affect heat transfer. Several have to do with the refrigeration system itself (piping design, material, flow rate,...). Three key properties of the refrigerant also affect the overall heat transfer capability of the system. These are the viscosity μ, specific heat C_p and thermal conductivity k. The goal is to work with substances that can carry a lot of energy (high specific heat) and can transfer the energy easily (high thermal conductivity), with a minimum pumping work. In order to better understand the effect of fluid properties on the heat transfer performance of falling film evaporators, two HFC refrigerants with different properties were tested: R134a and R236fa. Table 3.2 shows their physical properties.

Fluid Properties (T_{sat}=5°C)	R134a	R236fa	Relative variation [%]
Molar mass [kg/kmol]	102.03	152.04	+49.0
Pressure [kPa]	349.66	131.64	-62.4
Latent heat of vaporization [kJ/kg]	194.74	156.99	-19.4
Surface tension [mN/m]	10.844	12.415	+14.5
Liquid density [kg/m^3]	1278.1	1424.6	+11.5
Vapor density [kg/m^3]	17.131	9.155	-46.6
Liquid specific heat [kJ/kg.K]	1.3552	1.2182	-10.1
Liquid thermal conductivity [mW/m.K]	89.81	79.31	-11.7
Liquid viscosity [μPa.s]	250.11	370.03	+47.9

Table 3.2: Properties of R134a and R236fa and their relative variation at 5°C

3.4 Data acquisition and control

3.4.1 Data acquisition system

All measurements were made using a computer attached to a data acquisition system from National Instrument. The acquisition card is a PCI-MIO-16XE-50 with 16-bits resolution and a maximum acquisition frequency of 10kHz on a single channel. A SCXI-1000 module with four bays is connected to this card. Each of the four bays is equipped with a 32-channel voltage measurement card (SCXI-1102 card). The total number of acquisition channels is thus 128.

Each channel has a computer programmable gain: 1 for 0 to 10V signals (pressure transducers and mass flow meters), and 100 for low voltage signals (thermocouples). The signals can be adjusted to the 0 to 10V range of the acquisition card. A 2Hz low pass frequency filter is also included to reduce the measurement noise without affecting the steady-state measurements. At the end of the acquisition chain, a terminal block with 32 sockets is connected to the SCXI-1102 card. Each card has its own terminal block. The cold junction for every thermocouple is made in the terminal block at the socket. The material for this socket is copper for both poles (+ and -), the continuity of the two different specific materials of the thermocouple is then broken at this point located inside the terminal block. The temperature of the 32 cold junctions is maintained uniform with a metallic plate and is measured via a RTD element installed in the middle. Additionally, all the terminal blocks are isolated in an electrical cupboard to avoid any external thermal influence.

During a test, 100 acquisitions were made at a frequency of 50Hz to measure a test parameter in a channel and the average of these 100 values was calculated during the acquisition. The result is the measured value of the channel. In this way, any noise from alternating current on the measured signal is removed. This value is stored and the system goes to the next channel. With this measurement method, the theoretical channel measurement frequency is 50 channels/s, but due to the switching time between channels, the actual frequency is 30 channels/s. In total it takes 4.3s to measure all the channels of the acquisition system once. To obtain one experimental point, 30 such acquisition cycles are recorded and averaged.

3.4.2 Control system

A second computer is used to control the test facility with an identical SCXI system as on the data acquisition computer. The four bays of the SCXI-1000 module contain two cards for voltage measurement (SCXI-1102 cards), one card for the current measurement (SCXI-1102 card) and one card with six output channels (SCXI-1124 card). These outputs are used to control the three-way valve for the glycol, the valve for the hot water, the two electric heaters in the evaporator, the liquid heater and the vapor superheater. Two PID controllers are programmed on this computer: one for the electrical heating of the evaporator to control and maintain stable the saturation pressure in the test facility, and one for the hot water valve to control and adjust the hot water temperature flowing through the test section. All the parameters are displayed online on the computer screens and experimental parameters are calculated and displayed, such as the water temperature profile, local heat fluxes, heat transfer coefficients, PID status, etc.

3.5 Measurements and accuracy

The major objective of the experimental part of this work was to measure local external heat transfer coefficients over a range of liquid film flow rates. Local heat transfer coefficients were obtained using a modified Wilson plot method from the water temperature profile inside the tubes (see Chapter 4). Meanwhile, to completely establish the experimental conditions, some others parameters need to be measured directly or calculated from measured values.

3.5.1 Instrumentation of the test section

The test section was instrumented in order to estimate the degree of subcooling and check the homogeneity of the saturation conditions from top to bottom. The vapor pressure in the test section is measured with two absolute pressure transducers. One is connected to the test section above the array of tubes and one below. The vapor temperature above the tubes is measured with six thermocouples. Three are situated on the front and three on the rear of the test section. They are 1mm in diameter and the junction is located in the middle between the test section wall and the distributor. The temperature of the liquid entering the test section is measured with one thermocouple inserted in each inlet. Below the array of tubes, three thermocouples 2mm in diameter are installed on the front of the test section. The junctions of these thermocouples are situated in the middle between the front and rear side. The temperature of the vapor leaving the test section is measured with one thermocouple in the vapor pipe on the front after the two vapor outlets on the front joined and one at the same position on the rear. The temperature of the liquid leaving the test section is measured with a thermocouple inserted in the liquid outlet.

The wall temperature of the test section is measured with one thermocouple attached on the outside.

3.5.2 Physical properties estimation

All the physical properties for water and refrigerants, R134 and R236fa, were estimated using REFPROP 7.0 [69]. A look-up table with a step size of 0.05K was built with the desired physical properties for each fluid; intermediate values were determined by linear interpolation. This is a very precise and easy method to define the needed two-phase physical properties.

3.5.3 Saturation temperature

The saturation temperature T_{sat} of the refrigerant was calculated using the pressure measurements at the top and bottom of the test section and by the assumption of a linear pressure distribution over the height of the test section; a common assumption for heat exchangers. Then knowing the saturation pressure P_{sat}, the saturation temperature was obtained based on the vapor pressure curve. Two absolute pressure transducers (0 - 10 bars) are connected to the test section as described before with an accuracy of 0.1% of full scale corresponding to 1 kPa. The transducers were calibrated in the laboratory with a calibration balance. The deviation after calibration was always smaller than the one specified by the supplier.

3.5.4 Mass flow meters

Three Coriolis mass flow meters are installed on the test facility (0 - 1.667 kg/s for the water and glycol circuits, and 0 - 0.167 kg/s for the refrigerant circuit). The uncertainty in the measurement is provided by the constructor using the following equation:

$$\delta\dot{m}/\dot{m} \leq \pm(0.15 + S/\dot{m})\% \tag{3.1}$$

where S is a constant depending on the mass flow meter. The values are S=8.3 10^{-3} kg/s for the large mass flow meters and S=8.3 10^{-4} kg/s for the small one.

3.5.5 Water temperature profile

In most of the published heat transfer studies using water heated (or cooled) tubes, people only measure the inlet and outlet temperatures of the water. Using this type of measurement, only a mean heat transfer coefficient can be obtained for each tube. In this study another heat transfer measurement strategy was used to obtain local values for each tube: a modified Wilson Plot Method based on the local water temperature profile. The instrumentation of the tube was adapted to be able to measure the temperature variation along the tube. A stainless steel tube with a diameter of 8mm was inserted inside each copper tube, changing the intube flow to an annulus flow. This tube is instrumented with 6 thermocouples. A schematic of this instrumentation set-up is depicted in Fig. (3.8).

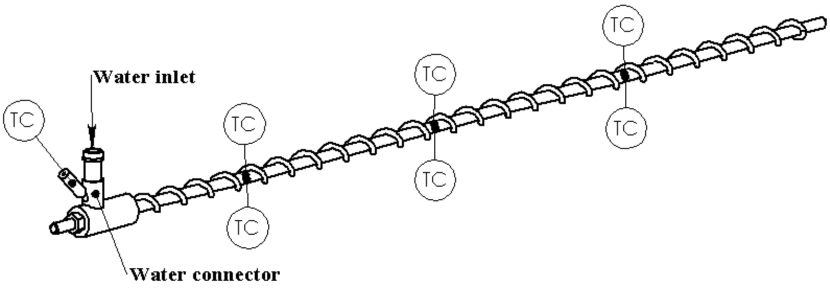

Figure 3.8: Tube instrumentation

The thermocouples are located at three positions axially along the tube. The thermocouple leads are all brought out at one end on the inside of the tube and are mounted on the stainless steel pipe where they are fixed. They were initially tin soldered but this did not last, due to the abrasive action of water, so they were glued in and protrude out through holes into the water flow. The distance between the thermocouples is 185mm and the distance to the wall end approximately 92mm. The distance to the wall ensures that no entrance effects are measured. The thermocouples are 0.5mm in diameter and have a length of 400 to 750mm.

In addition, at each location, one thermocouple faces upwards and one faces downwards to improve the precision of the measurement and also to check the mixing of the water in the annulus. The stainless tube helps to increase the water side heat transfer coefficient as the flow area for the water is reduced. To increase the accuracy of the measurement of the water temperature, a copper wire with a rectangular cross section (0.9×2.8mm) was wound helically (12mm pitch) around the stainless steel tube. This promotes better mixing, minimizes any entrance effect, and further increases the water side heat transfer coefficient.

The measured temperatures are between $3°C$ and $30°C$. Type-K thermocouples (Ni-Cr/Ni-Al) are used because they offer good precision in this range. The working principle of a thermocouple is based on the Seebeck effect. When two wires made of two different metallic materials are welded together at each end, a voltage appears if the two welded ends (or junctions) are at different temperatures. This voltage can be correlated to the temperature difference between the two ends. Measuring the temperature with a thermocouple consists of measuring the temperature of one junction (called cold junction) and the voltage that results. With these two values, the temperature of the other junction (measurement point of the thermocouple) can be calculated. In our case, the system measures the temperature of the cold junction and the voltage. It calculates the temperature of the thermocouple with standard polynomials of type K thermocouples. In order to improve accuracy of the temperature measurement, a calibration is required.

To take into account the thermal resistance due to the thermocouple fixation and the acquisition chain uncertainty, an on-site calibration is necessary to optimize the calibration uncertainty. The calibration set-up is described on Fig. (3.9).

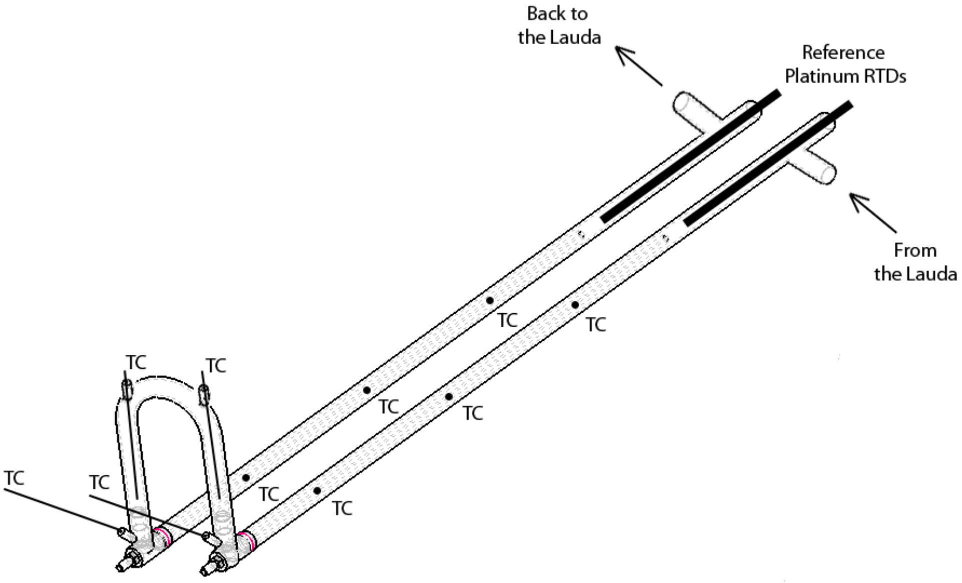

Figure 3.9: Schematics of the calibration set-up

Two instrumented tubes were simultaneously calibrated with their inlet and outlet thermocouples. A thermally insulated 2-pass circuit was connected to a thermo-controlled bath to set and stabilize the temperature inside the calibration rig. The reference temperature was measured using two platinum RTDs, both with a precision of 0.025K. For each calibration point, a stabilization period of 30 minutes was used once the difference between the two reference probes was smaller than 0.05K. The temperature step was 3K and the calibration was made with increasing and decreasing temperature to average hysteresis effects. Between calibration and measurement, the acquisition system was maintained turned at all times and the connections were never unplugged. A new calibration was made after changing the fluid or the type of tube. On a regular basis, the deviation between two calibrations was controlled and little variation between calibrations was observed.

The results of this careful calibration is a maximum deviation of 0.03K between the reference and the temperature reading from the thermocouple. Assuming that the thermocouples have the same uncertainty, the error on the calibration temperature measured by 2 sensors is estimated to be within $\Delta T_{wat} = \pm 0.03/\sqrt{2}K = \pm 0.02K$ as it is measured by two thermocouples at the same location.

3.5.6 Local heat flux

Heat is transferred from the hot water to the refrigerant. The 6 thermocouples described previously give the local water temperature profile in the axial flow direction as a function of the distance x along the tube. The enthalpy of the flowing water, assuming that the pressure drop along the annulus is negligible, is given for any location x by the following equation.

$$H_{wat}(x) = C_{p,wat}(x)T_{wat}(x) \tag{3.2}$$

Assuming that axial conduction along the tube is negligible, an energy balance on a differential element dx gives:

$$dq = \dot{m}_{wat} dH_{wat} \tag{3.3}$$

The derivative of Eq. (3.3) gives the local heat flux on the outside of the tube as:

$$q_o = \frac{\dot{m}_{wat} C_{p,wat}}{\pi D_o} \frac{dT_{wat}}{dx} \tag{3.4}$$

Thus, knowing the temperature profile $T(x)$, the local heat flux can be estimated at any point along the tube; to avoid any end effect, the local heat flux and local heat transfer coefficient will be determined in the middle of each tube.

The uncertainty analysis on the local heat flux measurement will be presented in Chapter 4.

3.5.7 Film Reynolds number

The onset of local dryout is a key parameter for the design of falling film evaporators. Therefore, the amount of liquid refrigerant reaching the top of each tube has to be evaluated. Some assumptions need to be made to estimate, with precision, the local film Reynolds number based on the measurement of the total mass flow rate delivered by the pump. An ideal flow between the tubes has been considered; assuming that all the liquid leaving the bottom of one tube reaches the top of the tube below it: $\Gamma_{bottom,tube(i)} = \Gamma_{top,tube(i+1)}$. Assuming the liquid refrigerant reaches the first tube at its saturation condition, the amount of liquid evaporated on the outside of the tube can be locally calculated by an energy balance:

$$\Gamma_{top,i} = \Gamma_{ref} - \sum_{n=1}^{i-1} \frac{q_{o,i} \pi D_o}{2H_{LV}} \tag{3.5}$$

where Γ is the flow rate on one side of the tube per unit length. The film Reynolds number on the top of each tube can then be calculated as:

$$Re_{film,i} = \frac{4\Gamma_{top,i}}{\mu_L} \tag{3.6}$$

Chapter 4

Wilson plot method

The main objective of this work is to determine the local external heat transfer coefficient. Measurement of evaporation heat transfer coefficients for smooth or enhanced tube surfaces requires recourse to Wilson plot techniques when using a single-phase fluid for heating/cooling inside the tube and the refrigerant on the outside, especially if direct wall temperature measurements cannot be made. This method was adapted at LTCM to allow repeatable, precise and accurate heat transfer measurements and to overcome some limitations of the conventional method.

4.1 Heat transfer calculation principles

Enhanced heat transfer coefficients are measured either utilizing a heated fluid test section or electric heaters. The latter presents significant disadvantages compared to real conditions and therefore the former has been used in the present study.

The overall thermal resistance of a heated tube R_{tot} is the sum of the convective resistance of the water $R_{conv,i}$, the tube wall conduction resistance $R_{cond,wall}$ and the convective resistance of the refrigerant $R_{conv,o}$:

$$R_{tot} = R_{conv,i} + R_{cond,wall} + R_{conv,o} \tag{4.1}$$

Fig. (4.1) shows the overall thermal resistance diagram with the temperature distribution for the local heat transfer measurement.

The overall thermal resistance R_{tot} can also be expressed as:

$$R_{tot} = \frac{T_{wat} - T_{sat}}{q_o} \tag{4.2}$$

Using heat transfer coefficients, equation Eq. (4.1) gives locally:

$$\frac{1}{U_o A_o} = \frac{1}{h_o A_o} + \frac{1}{h_i Ai} + r_{wall} \tag{4.3}$$

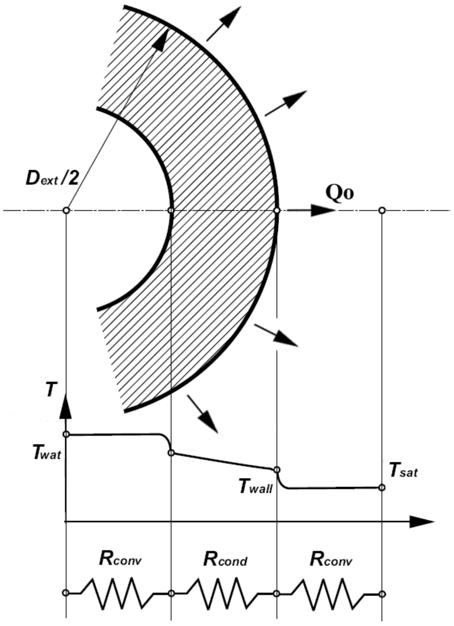

Figure 4.1: Thermal resistance diagram and temperature distribution during falling film evaporation

Reducing Eq. (4.3), the external heat transfer coefficient h_o can be expressed as:

$$h_o = \left[\frac{1}{U_o} - \frac{1}{h_i}\left(\frac{D_o}{D_i}\right) - R_{wall}\right]^{-1} \tag{4.4}$$

R_{wall} can be expressed based on radial conduction in a cylindrical wall:

$$R_{wall} = \frac{D_o}{2k_{wall}} \ln(\frac{D_{or}}{D_i}) \tag{4.5}$$

D_{or} represents the outside root diameter of the enhanced tube, measured by removing the structured surface on the outside. The presence of fins on the outside or ribs on the inside is encompassed in the internal and external heat transfer coefficients. For the plain tube, D_{or} corresponds to D_o.

The overall heat transfer coefficient U_o was calculated following:

$$U_o = \frac{q_o}{T_{wat} - T_{sat}} \tag{4.6}$$

where T_{wat} is the temperature of the water measured in the middle of the tube.

In the above set of equations α_i and α_o are the only unknowns while the other values are obtained from experimental measurements, geometric dimensions and fluid physical properties. One of the major problems in flow-heated test sections compared to electrically heated ones is the difficulty in accurately determining the heating fluid heat transfer coefficient (i.e. hot water). This becomes particularly difficult when dealing with an annular cross section and internally ribbed geometries. In order to reduce the uncertainties on the measurement of h_o, it is necessary to characterize the water side heat transfer coefficient as accurately as possible. A Wilson plot method approach was adapted to take into account the internal augmentations on the water side and achieve accurate measurements on the refrigerant side.

4.2 Wilson plot method

Historically the Wilson plot technique was developed by Wilson [70] in 1915 to determine individual heat transfer resistances from an overall resistance. Wilson expressed the tube-side resistance proportionally to the reduced velocity v_r, including effects of both property variations with temperature and tube diameter. Using the reduced velocity v_r, today known as the Reynolds number, Wilson wrote the resistance balance as:

$$\underbrace{\frac{1}{UA}}_{x} = C \underbrace{\frac{1}{(v_r)^{0.82}}}_{y} + R_{wall} \tag{4.7}$$

where C is a constant and R is the sum of the shell-side and wall resistances. If the shell-side resistance is kept fixed, which is difficult to achieve in practice, Eq. (4.7) takes the form of a straight line $y = mx + b$. During evaporation the wall temperature and consequently the external thermal resistance change only when the heating water velocity is varied. Under these conditions, the saturation temperature or heating water temperature has to be adjusted to maintain a constant external thermal resistance. It should be pointed out that Wilson's shell-side resistance was provided by condensing steam. The heat flux was not the same for all data points, which meant that there was a non-constant shell-side resistance.

The general Wilson plot technique equation for turbulent flow is given on the basis of the Dittus-Boelter equation by:

$$\frac{1}{U_o} - R_{wall} = \frac{1}{C_o Re_o^{0.8} Pr^{1/3}} + \left(\frac{D_o}{D_i}\right) \frac{1}{C_i Re_i^{a_i} Pr^{0.4}} \tag{4.8}$$

Shah [71] outlined the limitations of the original method, since it generally requires:

- Constant mass flow rates and log-mean average temperatures on the water side,
- Reynolds and Prandtl exponents presumed to be known,
- All test data must be in one flow regime for the test fluid,
- The fin/rib thermal resistance is not taken into account in the analysis,
- Same order of magnitude between shell- and tube-side thermal resistance.

Different authors have modified the original approach and proposed various modifications in which correlations were assumed known for both shell- and tube-side heat transfer coefficients, apart from certain constants.

4.3 Modified Wilson plot method

The original Wilson plot technique leads to 5 unknowns in the equations (C_i, C_o, a_i, a_o, r_{wall}) and there is no general solution method to solve it. However, Briggs and Young [72] proposed a method to solve this equation after reducing the number of unknowns to three (r_{wall} is known). They assumed the tube-side Reynolds exponent a_i to be known and equal to 0.8 for turbulent flow, and the three remaining unknowns C_i, C_o, a_o are then determined iteratively by means of two successive linear regressions. A value of the Reynolds number exponent a_o is assumed. The parameters C_i and C_o are obtained using a linear fit; the values of a_o and C_o are recomputed through a second linear regression closing the iterative loop. a_o is the parameter of convergence.

Khartabil and al [73] pointed out there are situations where no heat transfer information is available, typically for heat exchangers with enhanced tubes. Neither heat transfer correlations, nor wall resistance expressions are available for this type of application. Different approaches can be used to determine all three resistances when appropriate laws (with unknown constants) are assumed for the tube- and shell-side heat transfer coefficients. The authors also underline the importance of the method accuracy and present an iterative scheme to extend the method to four or five unknowns.

Different strategies can be applied to minimize the uncertainty on the method by playing with the data-reduction procedure or simply improving the measurement accuracy. Rose [74] considered directly the temperature differences rather than the thermal resistances. He further amplified the effect of thermal accuracy on Wilson plot results and presented general guidelines for assessing the accuracy of data using a residual minimization method. Another strategy, proposed by Sherbini et al. [75], uses a statistical approach based on a Chi-square analysis for minimizing the uncertainty.

The conceptual basis of the LTCM approach is the method developed by Briggs and Young. To ensure high accuracy in the measured heat transfer coefficients, it is very important to accurately define the inside heat transfer coefficient.

4.3.1 Calculation principles

In the approach used in LTCM, pool boiling tests are performed on the outside of the tube, taking advantage of their large values to characterize precisely the internal correlation. For a fixed saturation temperature, the outside pool boiling heat transfer coefficient was correlated using a nucleate pool boiling correlation [30]:

$$h_o = C_o q_o^n \tag{4.9}$$

The value of the exponent was choosen equal to $n = 0.7$. This value is used as a first step and the influence of this value on the constant C_i will be discussed later.

The more precise single-phase Gnielinski correlation was used rather than the Dittus-Boelter form for the internal heat transfer coefficient. The Gnielinski correlation [65] is a modification of the very accurate Petukhov turbulent flow correlation which extends its application domain to the transition flow regime. The Gnielinski correlation is given by:

$$Nu_{gni} = \frac{(f/8)(Re_{wat} - 1000)Pr_{wat}}{1 + 12.7(f/8)^{1/2}(Pr_{wat}^{2/3} - 1)} \tag{4.10}$$

where the friction factor f is defined by Petukhov [76]:

$$f = (0.79 \log(Re_{wat}) - 1.64)^{-2} \tag{4.11}$$

with

$$Re_{wat} = \frac{4\dot{m}_{wat}}{\pi(D_i + D_{inox})\mu_L} \tag{4.12}$$

The application domain is $3000 < Re_{wat} < 10^6$ and thus covers both the transition and turbulent flow regimes for a wide range of fluids. Its accuracy for determining heat transfer coefficients is quoted to be within 10%. The Petukhov relation for the friction factor is strictly only valid for a smooth internal tube surface. However, this correlation was used for all measurements. The effect of all internal enhancement is taken into account by the leading constant C_i, to be determined experimentally:

$$h_i = C_i h_{gni} \tag{4.13}$$

The leading constant C_i characterizes the influence of the inside surface enhancement on the heat transfer. It also includes the influence of the copper wire wound around the inner stainless steel tube to increase mixing and improve the accuracy and uniformity of water temperature measurements.

Rearranging Eq. (4.3) using Eq. (4.13) and Eq. (4.4):

$$\left(\frac{1}{U_o} - R_{wall}\right) q_o^n = \frac{1}{C_o} + \frac{1}{C_i}\left[\frac{q_o^n}{h_{gni}}\left(\frac{D_o}{D_i}\right)\right] \tag{4.14}$$

This equation has a simple linear form:

$$Y = \frac{1}{C_i}X + \frac{1}{C_o} \tag{4.15}$$

With a change of the water velocity, the values of X and Y are altered. The modified Wilson plot technique consists of measuring a set of points of this linear relation and performing a linear regression on these points. The inverse slope of this fit gives the value of C_i and the inverse of the Y-axis intercept yields C_o. Our main interest is the value of C_i, as in combination with the Gnielinski correlation the water side coefficient can be determined according to Eq. (4.13).

4.3.2 Measurement system validation

Before beginning with the experimental campaign, the entire measurement system needed to be validated using a reference method. Actual falling film heat transfer prediction methods are mainly analytical or semi-empirical approaches based on experimental tests, which makes the comparison even more difficult. The Nüsselt falling film analysis [18] was among the first heat transfer problems to be successfully solved from a fundamental point of view, giving excellent results. To be sure that the measurement system was working correctly, condensation tests on a single horizontal plain tube were conducted and compared to Nüsselt theory. Nüsselt expressed the average heat transfer coefficient as:

$$h_o = 0.728 \left[\frac{g\rho_L(\rho_L - \rho_V)k_L^3 H_{LV}}{\mu_L(T_{sat} - T_{wall})D} \right]^{1/4} \tag{4.16}$$

For a detailled description of the falling film condensation measurement procedure, refer to Gstoehl [4]. The comparison between the measured data and the prediction using Nüsselt theory for a horizontal plain tube are given in Fig. (4.2). An agreement of 100% of the data within ±20% was obtained, confirming the validity of the measurement system. The repeatability was also tested and gave excellent results.

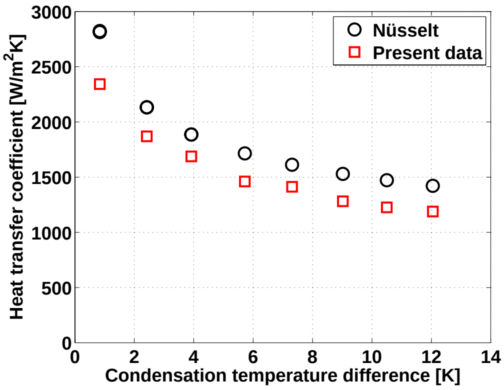

Figure 4.2: Measurement system validation using Nüsselt theory

4.3.3 Measurement procedure

The experimental procedure for the modified Wilson plot technique described above is the following:

1. The tube to test is connected to the water loop as a 1-pass circuit. To maintain the external thermal resistance constant, a pool boiling configuration was used. The test section was insulated and partially filled with refrigerant; 2 tubes at the top of the test section were connected to a thermally-controlled bath. They are used to compensate the amount of refrigerant evaporated from the tested tube by recondensing the vapor and maintain a fixed saturation condition. All other tubes are inactive.

2. The temperature and the flow rate of the water are adjusted to reach the desired heat flux on the tube while the thermally-controlled bath controls the saturation conditions.

3. The internal thermal resistance is gradually increased in the transition flow regime by adjusting the hot water mass flow rate. For each step, the temperature has to be changed to keep the same heat flux on the outside.

4. When steady-state is reached, data are acquired and processed using Matlab. The water mass flow rates are chosen to cover the planned experimental conditions for the water side.

Repeatability and stability of the method have been tested using different heat fluxes, tubes, saturation temperatures and refrigerants. The value of C_i should be independent of these parameters.

4.3.4 Results and accuracy

The modified Wilson tests were conducted over a water side Reynolds number range from 6000 to 16000 that will be used in the evaporation tests. For the plain tube, different instrumented stainless steel tubes inside different plain tubes were tested to verify the reproducibility of the measurements. To check the reliability of the method, tests were performed also at different heat fluxes and different saturation temperatures, implying different water temperatures and refrigerants. In order to calculate the uncertainty on the estimation of C_i, a T-Student approach was preferred as only five experimental points were taken for each tested tube. A confidence interval of 97.5% was chosen and the uncertainty was estimated by:

$$\bar{C}i \pm t_{df,0.975}\left(\frac{s}{\sqrt{n}}\right) \tag{4.17}$$

where s represents the estimated variance, n the number of measurements, $df = n - 1$ the degree of freedom and where $t_{df,0.975}$ is given by the T-student law (tabulated values).

Modified Wilson plots for each type of tube are shown in Fig. (4.3). The value of C_i corresponds to the inverse of the slope of the linear regression and are listed for each type of tube in Tables 4.1 to 4.4.

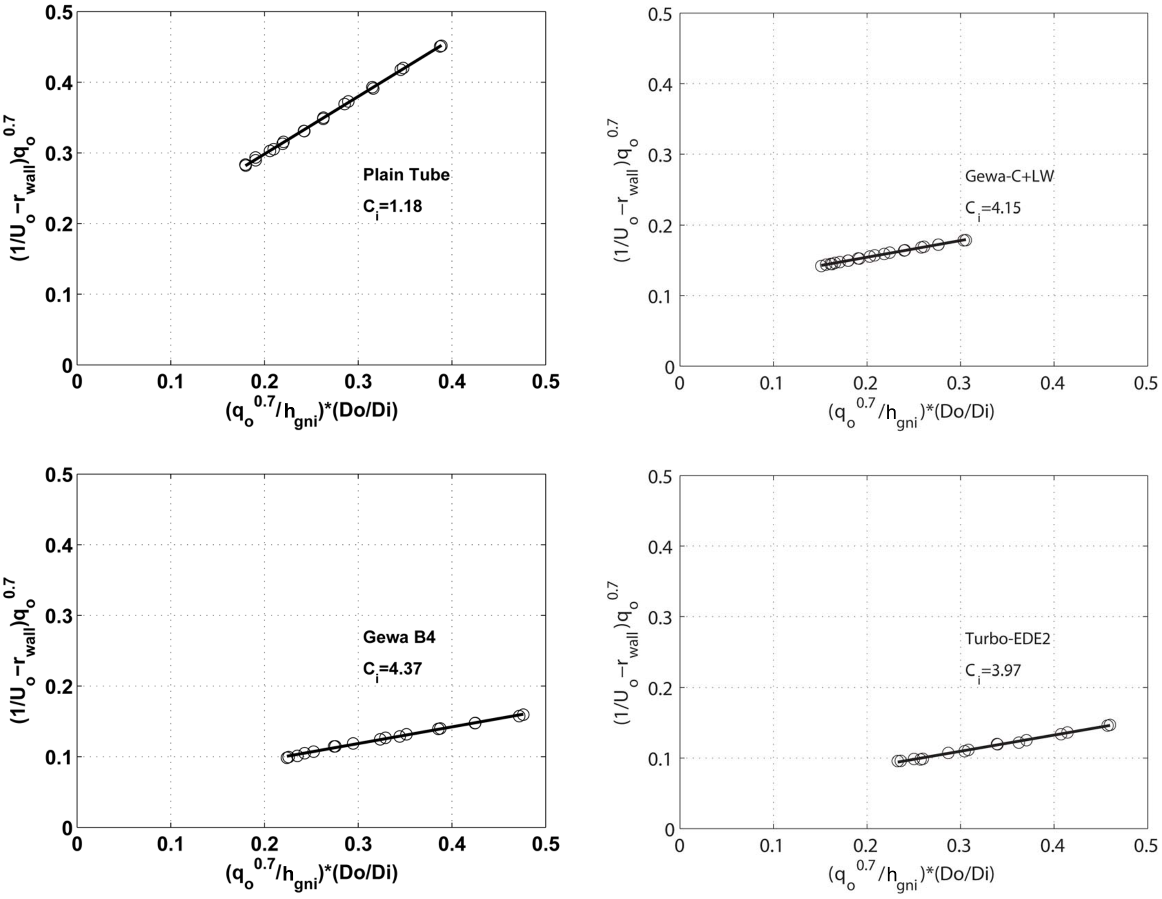

Figure 4.3: Modified Wilson plots for all types of tubes in pool boiling

instrumented rod	T_{sat} [K]	q_o $[kW/m^2]$	C_i [-]
1	303	20	1.21
1	303	20	1.18
4	303	20	1.14
4	293	20	1.19
6	293	40	1.17
average value for Plain Tube			1.18
T-Student deviation			0.07

Table 4.1: Measurements of the corrective multiplier of the water side coefficient for the plain tube.

4.3.5 Summary

The water side heat transfer coefficients were determined experimentally for all tubes using a modified Wilson plot technique. The Wilson plot procedure was implemented using nucleate boiling on the outside of the tube. The external heat transfer coefficient was

instrumented rod	T_{sat} [K]	q_o [kW/m^2]	C_i [-]
10	293	40	4.21
10	293	40	4.22
2	303	40	4.03
2	303	60	4.07
2	303	20	4.20
average value for Gewa-C+LW			4.15
T-Student deviation			0.22

Table 4.2: Measurements of the corrective multiplier of the water side coefficient for the Gewa-C+LW.

instrumented rod	T_{sat} [K]	q_o [kW/m^2]	C_i [-]
10	293	40	4.37
10	293	40	4.33
9	278	40	4.43
9	293	60	4.34
average value for Gewa B4			4.37
T-Student deviation			0.12

Table 4.3: Measurements of the corrective multiplier of the water side coefficient for the Gewa B4.

instrumented rod	T_{sat} [K]	q_o [kW/m^2]	C_i [-]
10	293	40	3.93
10	303	40	3.99
6	288	40	3.97
6	293	60	3.99
average value for Turbo-EDE2			3.97
T-Student deviation			0.07

Table 4.4: Measurements of the corrective multiplier of the water side coefficient for the Turbo-EDE2.

thus only a function of the heat flux. During the measurements, the water flow rate and temperature were changed to obtain a variation of the water side heat transfer coefficient but the heat flux was maintained constant. The water-side heat transfer multipliers C_i for the various tubes to be experimentally tested were accurately obtained, which include the characteristics of the experimental setup. This means mainly the influence of the instrumented stainless steel tube with its spiral wound wire and also the internal enhancement of the copper tubes. With these corrective multipliers and the Gnielinski correlation, the water side coefficient can be accurately calculated. A known water side coefficient allows the determination of the local external heat transfer coefficient during pool boiling and falling film evaporation based on measurement of the water temperature inside the tube and its profile to get the local heat flux. It will be found in Chapter 5 that in nucleate pool boiling conditions, $h = q_o^n$ with values of n different than the one used in Eq. (4.9) ($n = 0.7$). However, the influence of this parameter on the constant C_i was found negligible; the difference is thus covered by the uncertainty estimated on the C_i coefficient.

The average values of the multipliers for all tubes are listed in Table 4.5. Note that these multipliers for the internally enhanced tubes do not correspond to their normal multipliers in evaporators without the inserted tube inside.

Tube	C_i [-]
Plain Tube	1.18 ± 0.07
Gewa-C+LW	4.15 ± 0.22
Gewa B4	4.37 ± 0.12
Turbo-EDE2	3.97 ± 0.07

Table 4.5: Corrective multipliers for internal heat transfer coefficient

4.4 Heat transfer measurement accuracies

4.4.1 Local heat flux

According to Eq. (3.4), the heat flux is a direct function of the axial temperature profile derivative. It can be shown mathematically that the derivative of a second order polynomial fit through thermocouples at 3 different locations is equivalent to the mean value over that tube length:

$$q_o = \frac{\dot{m}_{wat} C_{p,wat}}{\pi D_o} \frac{T_{wat,out} - T_{wat,in}}{L} \tag{4.18}$$

The local heat flux measurement uncertainty, based on the general definition of Kline and McClintock [77] and applied to Eq. (4.18) is:

$$\delta q_o = \sqrt{\left(\frac{\partial q_o}{\partial \dot{m}} \cdot \Delta \dot{m}\right)^2 + \left(\frac{\partial q_o}{\partial T_{wat,out}} \cdot \Delta T_{wat,out}\right)^2 + \left(\frac{\partial q_o}{\partial T_{wat,in}} \cdot \Delta T_{wat,in}\right)^2} \tag{4.19}$$

Evaluation of the partial derivatives and substitution of the temperature uncertainties by $\Delta T_{wat} = \Delta T_{wat,in} = \Delta T_{wat,out}$ leads to:

$$\delta q_o = \sqrt{\left(\frac{C_{p,wat}}{\pi D_o L}(T_{wat,out} - T_{wat,in}) \cdot \Delta \dot{m}\right)^2 + 2\left(\frac{\dot{m} C_{p,wat}}{\pi D_o L} \cdot \Delta T_{wat}\right)^2} \tag{4.20}$$

The thermo-physical properties and the geometric quantities were assumed to be known exactly. The uncertainty of the total water mass flow is given by Equation Eq. (3.1), giving a relative error smaller than 0.18% for all measurements. The total water mass flow is split into five sub-circuits during the measurements; taking into account the possible maldistribution, the uncertainty of the water flow rate in each tube was considered to be the same as the one on the total mass flow.

The uncertainty on the local heat flux was mainly governed by the second term of Equation Eq. (4.20), corresponding to the water temperature measurement. The uncertainty on the local heat flux logically decreased with increasing heat flux, where the water temperature differences become larger. The propagation of error also depends on the tube performance and on the tested fluid: the higher the heat transfer coefficient, the smaller the water temperature difference. The values of the mean relative errors in local heat flux for all principal tests are presented in Tables 4.6 and 4.7.

Tube	$q_o = 20kW/m^2$	$q_o = 40kW/m^2$	$q_o = 60kW/m^2$
Plain Tube	4.7%	4.6%	4.6%
Gewa-C+LW	6.8%	6.4%	6.3%
Gewa-B4	10.4%	8.8%	7.9%
Turbo-EDE2	10.2%	8.1%	7.4%

Table 4.6: Mean relative errors of the local heat fluxes with R134a

Tube	$q_o = 20kW/m^2$	$q_o = 40kW/m^2$	$q_o = 60kW/m^2$
Plain Tube	6.1%	5.8%	5.5%
Gewa-C+LW	8.0%	7.6%	7.5%
Gewa-B4	12.1%	10.1%	9.4%
Turbo-EDE2	11.7%	9.7%	9.2%

Table 4.7: Mean relative errors of the local heat fluxes with R236fa

4.4.2 Local heat transfer coefficient

The local heat transfer coefficient measurement uncertainty is given by:

$$\Delta h_o = \sqrt{(\frac{\partial h_o}{\partial \dot{m}} \cdot \Delta \dot{m})^2 + (\frac{\partial h_o}{\partial T_{wat}} \cdot \Delta T_{wat})^2 + (\frac{\partial h_o}{\partial T_{sat}} \cdot \Delta T_{sat})^2 + (\frac{\partial h_o}{\partial q_o} \cdot \Delta q_o)^2 + (\frac{\partial h_o}{\partial C_i} \cdot \Delta C_i)^2} \tag{4.21}$$

Tube	$q_o = 20kW/m^2$	$q_o = 40kW/m^2$	$q_o = 60kW/m^2$
Plain Tube	20.4%	16.9%	15.0%
Gewa-C+LW	28.8%	28.6%	28.2%
Gewa-B4	19.6%	14.8%	12.6%
Turbo-EDE2	18.2%	15.3%	10.4%

Table 4.8: Mean relative errors of the local heat transfer coefficients with R134a

Tube	$q_o = 20kW/m^2$	$q_o = 40kW/m^2$	$q_o = 60kW/m^2$
Plain Tube	25.3%	17.4%	15.8%
Gewa-C+LW	32.9%	32.3%	31.3%
Gewa-B4	–	19.8%	14.2%
Turbo-EDE2	–	18.7%	15.4%

Table 4.9: Mean relative errors of the local heat transfer coefficients with R236fa

The uncertainty on the local heat transfer was mainly governed by the uncertainties on the local heat flux and on the water temperature measurement. As was the case for the local heat flux, the uncertainty of the local heat transfer coefficient logically decreases with increasing heat flux, where the water temperature differences become larger. The propagation of error also depends on the tube performance and on the tested fluid: the higher the local external heat transfer coefficient, the smaller the superheat. The values of the mean relative errors in local heat transfer coefficients for all principal tests are presented in Tables 4.8 and 4.9.

Chapter 5

Single Row Falling Film Evaporation

In this chapter, an analysis of the local heat transfer data is presented for single row falling film evaporation. Since it is clear that nucleate boiling is a one of the major mechanisms in the process, the falling film multiplier $K_{ff} = h_o/h_{pb}$ defined by Roques [3] allows an easy comparison between the falling film and the pool boiling heat transfer performances. In this ratio, h_o is the falling film heat transfer coefficient and h_{pb} is the nucleate pool boiling heat transfer coefficient at the same heat flux. Thus, nucleate pool boiling experiments were required to obtain the values of h_{pb}.

5.1 Plain tube results

5.1.1 Pool boiling results

The same data reduction procedure described in Chapter 4 was used for running pool boiling experiments. In this configuration, the test section is isolated and partially filled up with liquid refrigerant to cover the boiling tube. The saturation condition in the test section was maintained constant using a cooling source to condense the vapor generated at the top of the test section. The heat flux was changed by adjusting the water temperature and flow rate inside the tube. The pool boiling curves obtained for plain tube for both R134a and R236fa are depicted in Fig. (5.1).

The plain tube performances observed with R134a are almost twice as high as those obtained with the lower pressure R236fa. The heat transfer coefficients increase in the order of vapor pressure for a given heat flux for R134a, confirming the typical nucleate boiling trend, where the wall superheat required to activate given size cavities becomes smaller as the pressure is increased [30]. Tests at $20°C$ with R236fa could not be performed with the test facility and only a slight effect of pressure was observed at 5 and $10°C$ (perhaps due to the propagation of errors). Jung et al. [78] showed that nucleate boiling heat transfer coefficients are directly proportional to the reduced pressure. Simple correlations of the form $h_{pb} = C \cdot q^n$ for experimental results in nucleate boiling can be easily obtained at

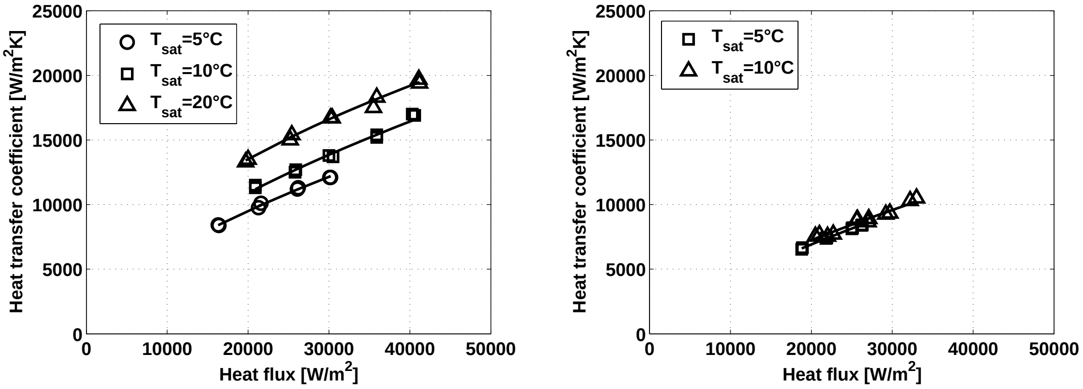

(a) R134a (b) R236fa

Figure 5.1: Pool boiling measurement on plain tube for R134a and R236fa

one specific reduced pressure but often exhibit a wide scatter in the values of the constant and the exponent among different authors. The database obtained here for the plain tube in pool boiling allows us to correlate both fluid and saturation condition effects, which is not possible using the simple expression described previously. A nucleate pool boiling correlation was obtained for the present pool boiling database (48 points):

$$h_{pb} = 35 p_r^{0.42} q_o^{0.67} \tag{5.1}$$

In Fig. (5.2), the experimental vs. predicted data for both fluids are presented, which depict very good agreement to Eq. (5.1).

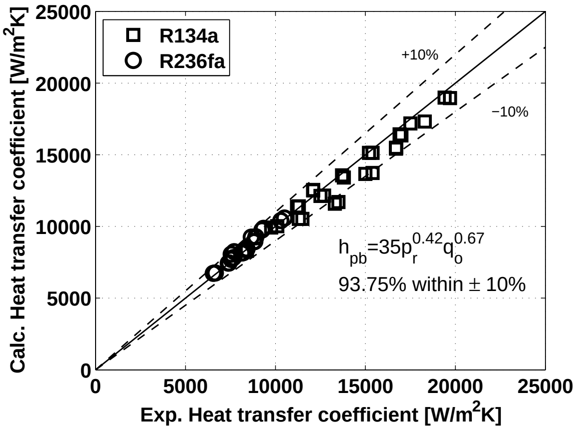

Figure 5.2: Comparison of experimental versus predicted values for pool boiling on a plain tube

These experimental results are next compared to the prediction methods reported in section 2.2.2 and the results are depicted on Fig. (5.3). The peak roughness of the tube's external surface R_p needed for the Cooper correlation was measured by means of a laser profilometer. Different samples were measured and the resulting roughness was $R_p = 2.30 \mu m$. The tested copper surface has a relatively high surface roughness and the heat transfer coefficient is underpredicted by all the existing correlations. Table 5.1 shows the ability of these correlations to predict the 5°C plain tube data for both refrigerants. For the present plain tube data, the Cooper correlation gives the best prediction within the tested correlations with an average error for all of the data of -35% for R134a and -40% for R236fa.

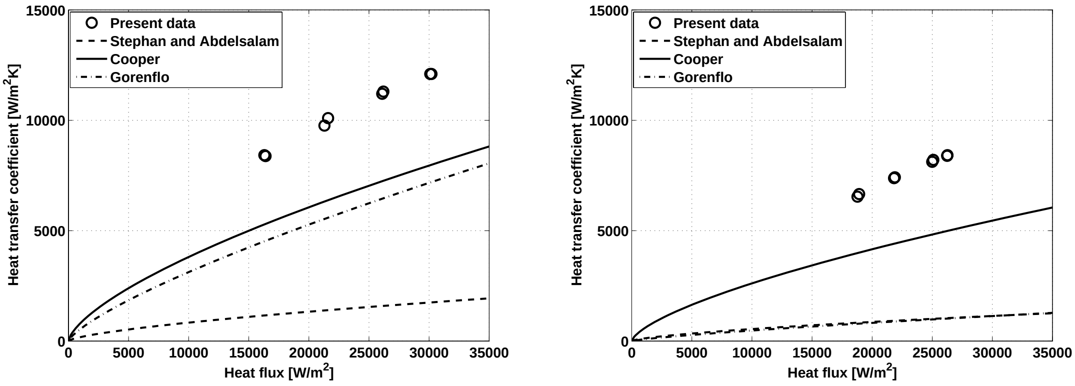

(a) R134a

(b) R236fa

Figure 5.3: Comparison of pool boiling measurements with prediction methods on plain tube at $T_{sat} = 5°C$ for R134a and R236fa

	Relative error (%)	
Correlation	R134a	R236fa
Stephan and Abdelsalam	-86	-65
Cooper	-35	-40
Gorenflo	-43	-65

Table 5.1: Comparison of experimental results with existing correlation

The pool boiling databases of Webb and Pais [79] and Hsieh and Hsu [80] for R134a yield a wide scatter when compared to one another. With respect to the previous data obtained by Roques [3] using the same test facility but different tube samples and Robinson [81] using a different test facility and tube sample in the LTCM lab, the present data for R134a are about $10-15\%$ higher, which are within the propagation of error of the measurements.

5.1.2 Falling film evaporation results

Falling film evaporation heat transfer results are presented for R236fa on the plain surface tubes of 18.9mm actual diameter at nominal heat fluxes of 20, 40 and $60kW/m^2$ in Fig. (5.4). The local heat transfer coefficients for all tubes are presented as a function of the film Reynolds number, the latter calculated as always assuming the liquid remains on the tube, i.e. no liquid slinging effect. Fig. (5.4) shows that the heat transfer performance is dependent upon the heat flux, indicating that nucleate boiling is present in the heat transfer process. In fact, the measured heat transfer coefficients were dominated by the boiling heat transfer contribution. The heat transfer performances from tube to tube agreed to within ±20%, corresponding to the range of uncertainty in h_o. As also observed by Roques [3], the boiling region is characterized by a large plateau where boiling occurs in the liquid film and the partial dryout region is characterized by a rapid decrease of the heat transfer coefficient with the liquid overfeed due to the onset of dry patch formation. The heat transfer performances from tube to tube agreed to within ±20%, corresponding to the range of uncertainty.

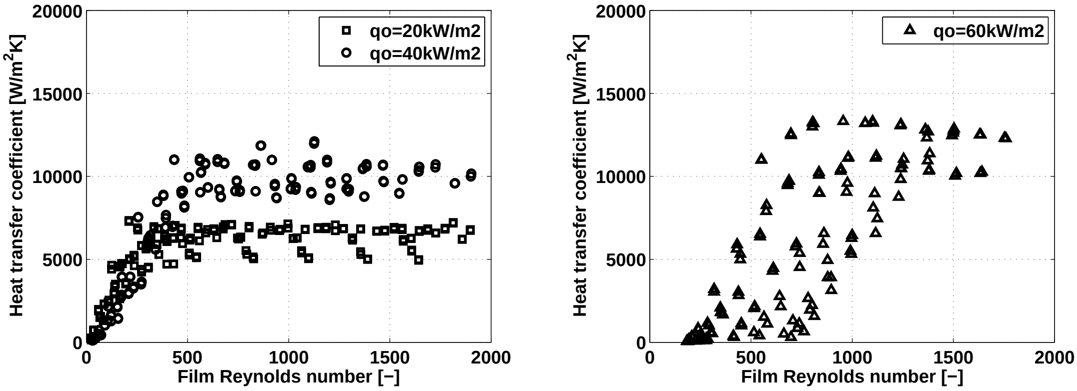

(a) $q_o = 20$ and $40kW/m^2$ (b) $q_o = 60kW/m^2$

Figure 5.4: Falling film evaporation on plain tube at $T_{sat} = 5°C$ with R236fa

The performance observed with a heat flux of 60 kW/m^2 are very scattered. The assumption of ideal liquid film flow was not verified anymore in these conditions since liquid in the film was leaving from the side of the tube array due to droplet/column deflection and liquid splashing, thus creating premature dry patch formation (that is, if a lot of liquid leaves the array, the actual Re is much less than the ideal Re assumed to present the data).

The threshold Reynolds number corresponding to the onset of dryout is logically a function of the heat flux: it increased from 330 for $20kW/m^2$ to 500 for $40kW/m^2$, similar to the values observed by Roques for R134a. The results he obtained for R134a are presented on Fig. (5.5) for comparison purposes.

The heat transfer performance measured for R236fa are 20 to 30% lower than that of R134a, corresponding approximately to the difference observed under pool boiling conditions. The difference in latent heat of vaporization and reduced pressure between R134a and R236fa explain the higher performance obtained with R134a. At 60 kW/m^2, the R134a data do not exhibit much scatter and the estimation of the film Reynolds number is accurate; the hydrodynamics of the film was more stable and the amount of liquid leaving the tube array appeared to be negligible. The “plateau” of uniform heat transfer for a wide range of Re and the fall-off in heat transfer with the progressive dryout as $Re \rightarrow 0$ is quite evident here.

For the plain tube, the falling film multiplier K_{ff} was calculated based on a reference pool boiling correlation to get a reasonable comparison between the two tested fluids. The Cooper correlation was chosen using the measured surface roughness because it is the closest one to the present pool boiling results. The Cooper correlation was chosen to

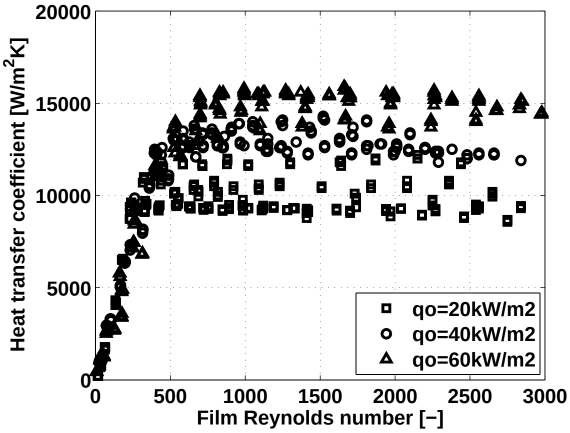

Figure 5.5: Falling film evaporation on plain tube at $T_{sat} = 5°C$ with R134a (Roques [3])

obtain a more general approach rather than a fluid/study specific approach that would result using Eq. (5.1) and thus in order to get a better comparison between the two fluids. The falling film multipliers for the plain tube are presented in Fig. (5.6).

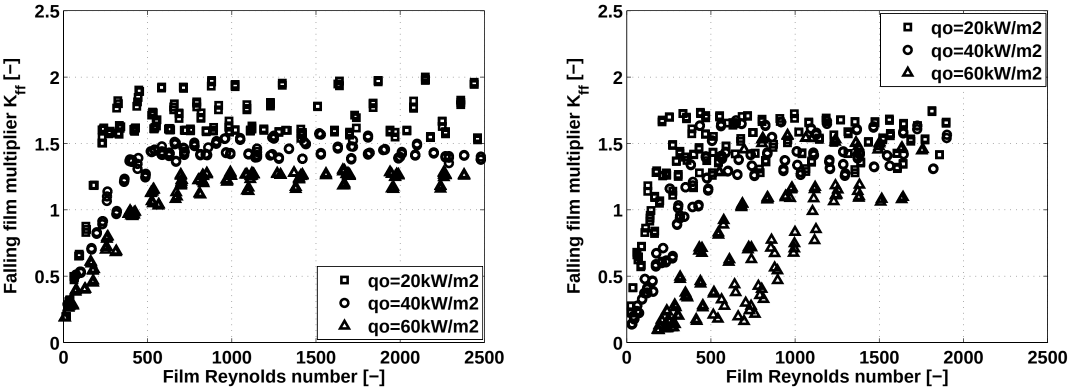

(a) R134a

(b) R236fa

Figure 5.6: Falling film multiplier K_{ff} on plain tube at $T_{sat} = 5°C$ for R134a and R236fa

For the plain tube, the heat flux has an influence on the falling film multiplier. The performance in falling film evaporation with R134a and R236fa conditions is thus respectively between 20 and 100% and between 10 to 70% higher than in pool boiling, neglecting the values of R236fa with premature dry patch formation for $q_o = 60kW/m^2$ due to liquid slinging. The highest ratio was obtained for $q_o = 20kW/m^2$ with falling film heat transfer coefficients almost twice the pool boiling one, which confirms the advantage of using falling film technology for low heat flux applications. For comparison, Zeng et al. [82] found values of the falling film multiplier between 1.5 and 2 for ammonia with a square-pitch plain tube bundle and Danilova et al. [52] got K_{ff} values of 1.33, 1.4 and 1.5 for R22 at $q_o = 16kW/m^2$ at saturation temperatures of -45, -25 and 0°C.

5.2 Enhanced surface results

5.2.1 Pool boiling results

The data for the three tube geometries and two refrigerants are presented on Fig. (5.7) through Fig. (5.9). The comparison with other authors was not possible as no publications with the present enhanced tube geometries are currently available in the literature.

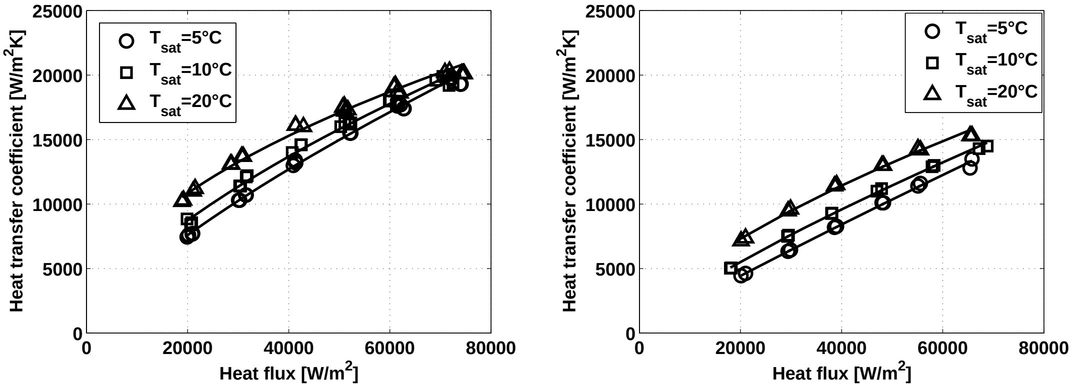

(a) R134a (b) R236fa

Figure 5.7: Pool boiling measurement on the Gewa-C+LW for R134a and R236fa

The Gewa-C+LW enhanced condensing tube from Wieland shows a similar behavior as the plain tube when operated in pool boiling conditions. The fins of this enhanced condensing tube did not seem to have a significant effect on the pool boiling performance relative to the plain tube. It is important to note that the increase of heat transfer area due to the presence of fins was not taken into account in the calculation; the diameter at the top of the fins was chosen for the outside area estimation. The lower heat transfer coefficient observed compared to the plain tube is probably due to fact that this enhanced tube will tend to retain vapor between the fins and hence only the outer fin tip surface is available for boiling. A nucleate pool boiling correlation was obtained for the present pool boiling database (95 points) with an agreement of 91.6% within ±10%:

$$h_{pb} = 28 p_r^{0.42} q_o^{0.67} \tag{5.2}$$

The Gewa-B4 tube from Wieland-Werke gives two very different pool boiling heat transfer trends. With R134a for which it is normally applied, the heat transfer performance was not significantly affected by the variations of heat flux or saturation pressure with a mean value over the tested range of about $45000 W/m^2K$ with a standard deviation of only 6.8%. With R236fa, the heat transfer performance was higher and decreased with increasing heat flux, particularly at low saturation pressures. This decreasing trend might correspond to the progressive dryout of the channel within the enhancement structure but the heat transfer coefficients are so high that this does not seem reasonable. Hence, it is more likely a throttling effect of the pore opening on the inflow of liquid and the escape of water. It is remarkable to see that the saturation pressure effect is high at low heat

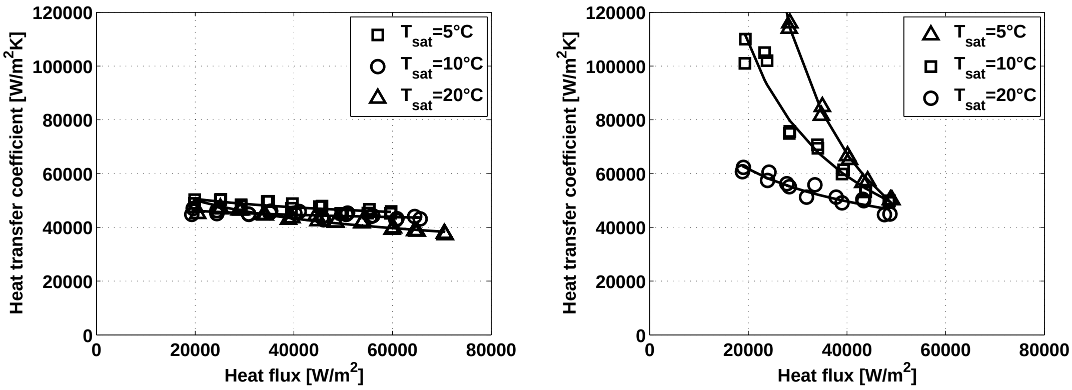

(a) R134a (b) R236fa

Figure 5.8: Pool boiling measurement on Gewa-B4 for R134a and R236fa

flux and decreases with increasing heat flux. It is also important to mention that the uncertainty related to the estimation of the heat transfer coefficient is higher at lower heat fluxes due to the small temperature differences involved in these conditions.

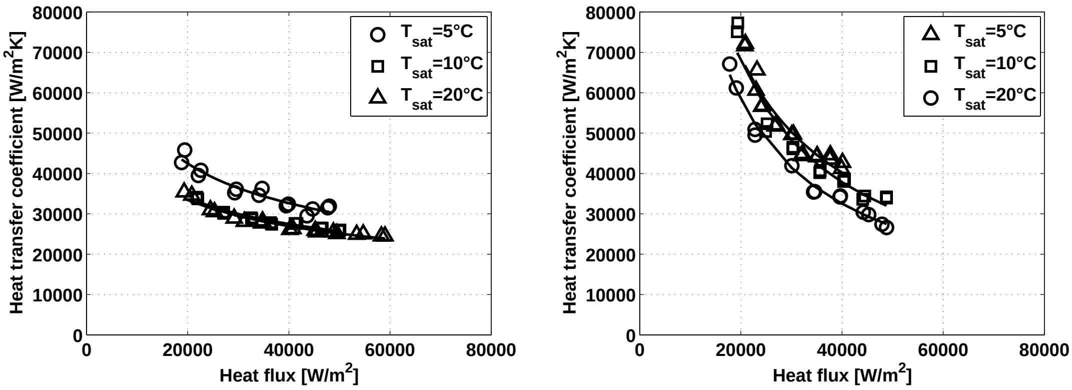

(a) R134a (b) R236fa

Figure 5.9: Pool boiling measurement on Turbo-EDE2 for R134a and R236fa

The Turbo-EDE2 tube from Wolverine (normally utilized for R134a) presents somewhat similar trends as the Gewa-B4. The R134a data exhibit a slowly decreasing trend with an optimized performance for a saturation temperature of 5°C. With R236fa again heat transfer was higher and a steep decreasing trend was observed but only a small saturation pressure effect was noticed. Thome [2] showed that at high reduced pressure, the relative advantage of using enhanced boiling surfaces is diminished since nucleation sites are already activated due to a decrease in required nucleation superheat. Furthermore the pore sizes are optimized for the standard operating condition of 5°C. This was verified with the two boiling enhanced tubes.

As the heat transfer mechanisms involved in the enhanced pool boiling heat transfer process are still not well understood with respect to the characteristics of the enhancement geometry, and as parameters such as the nucleation site density, the bubble frequency,

	R134a		R236fa	
Tube	C	n	C	n
Plain	24,01	0.604	4.82	0.734
Gewa-C+LW	4.30	0.754	0.461	0.926
Gewa-B4	$1.260 \cdot 10^5$	-0.092	$651.9 \cdot 10^9$	-1.519
Turbo-EDE2	$1.833 \cdot 10^6$	-0.380	$1.506 \cdot 10^8$	-0.776

Table 5.2: Empirical coefficients for pool boiling at $T_{sat} = 5°C$

etc. are difficult to measure and obtain precisely, the data for each type of tube were correlated using a simple expression of the form $h_{pb} = C \cdot q^n$. The values of C and n at $5°C$ are given in Table 5.2 for all tubes. The values of n for the plain tube are similar to those of most plain tube boiling correlations that are typically from 0.67 to 0.7. The negative values of n for the two enhanced boiling were also found in the study of Roques and Thome [83] and Robinson and Thome [84].

5.2.2 Falling film evaporation results

Gewa-C+LW tube

Fig. (5.10) shows the falling film evaporation heat transfer performance of the enhanced condensing Gewa-C+LW tube. The heat transfer trend emphasizes clearly the threshold between the all wet and the partially wet regions. There is a distinct presence of a peak at the lowest heat flux. This peak disappears when the heat flux is increased. The onset of boiling is shifted depending on the heat flux. The comparison between the two fluids shows similar performance at $q_o = 60kW/m^2$. At $q_o = 20$ and $40kW/m^2$, the difference in performance between the two fluids was respectively 42% and 23%, decreasing with increasing heat flux.

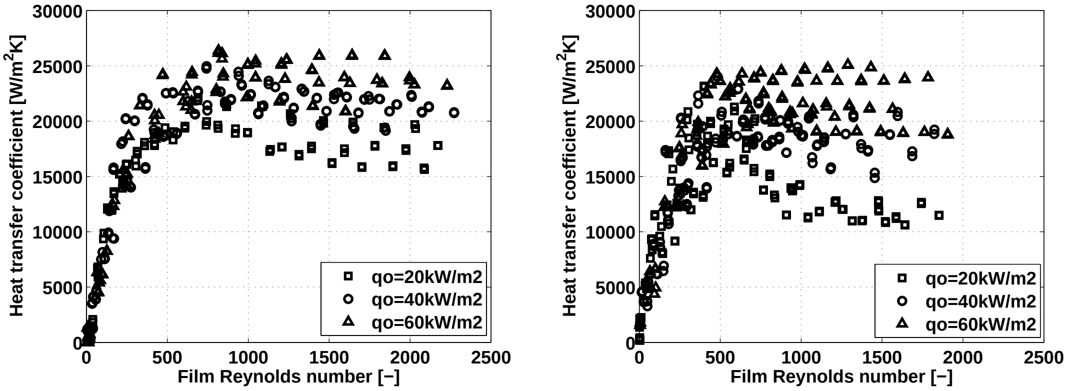

(a) R134a (b) R236fa

Figure 5.10: Falling film evaporation on Gewa-C+LW at $T_{sat} = 5°C$ for R134a and R236fa

The falling film multipliers for this tube are presented in Fig. (5.11); the pool boiling correlation used for the calculation of K_{ff} was based on the coefficients located in Table

5.2. The variation of the falling film multiplier with film Reynolds number presents a different trend that the usual trend observed by Roques [3] at low heat flux. At $q_o = 40$ and $60kW/m^2$ an enhancement similar to the plain tube was observed, with K_{ff} values ranging between 1 and 1.7. At $q_o = 60kW/m^2$, the falling film multiplier presents a maximum value between 2.5 and 3 at low film Reynolds number and then decreases to reach values between 1 and 2. The prediction method developed by Roques for the falling film multiplier is not sufficient to accurately predict such a trend and needs to be modified for this type of surface. The heat transfer coefficient enhancement provided here is only high near the onset of dryout (where the coefficients fall off with decreasing film Reynolds number) but tends to disappear in the boiling-dominated region, with K_{ff} values then on the order of 1-1.2. Thus, the film flow apparently has a beneficial influence on enhancing the nucleate boiling process only in this range. However, it is not clear why.

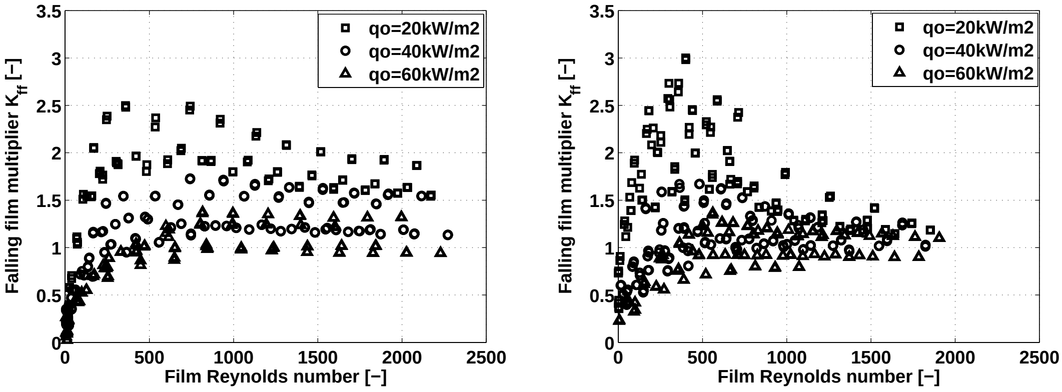

(a) R134a (b) R236fa

Figure 5.11: Falling film multiplier K_{ff} on Gewa-C+LW at $T_{sat} = 5°C$ for R134a and R236fa

Gewa-B4 tube

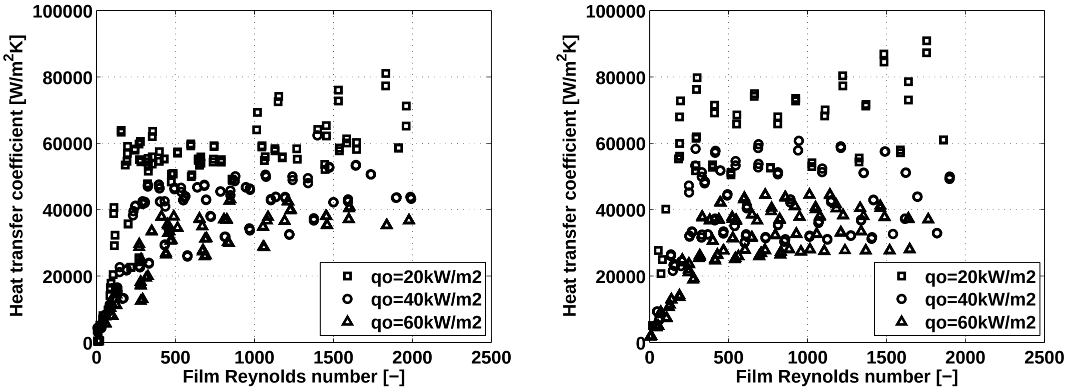

(a) R134a (b) R236fa

Figure 5.12: Falling film evaporation on Gewa-B4 at $T_{sat} = 5°C$ for R134a and R236fa

Fig. (5.12) shows the falling film evaporation heat transfer performance of the enhanced boiling Gewa-B4 tube. This 3D-structured surface is a new version of the Gewa-B enhanced surface tested by Roques [3] whose results for R134a are depicted in Fig. (5.13). The trend observed with the Gewa-B4 is a little different from the other tubes: the heat transfer coefficient presents a non-constant behavior and increases with increasing film Reynolds number. The heat transfer performances obtained with the Gewa-B4 tube are largest for $q_o = 20kW/m^2$ (reaching values as high as $80000W/m^2K$) and are 100 to 200% higher compared to the Gewa-B tube.

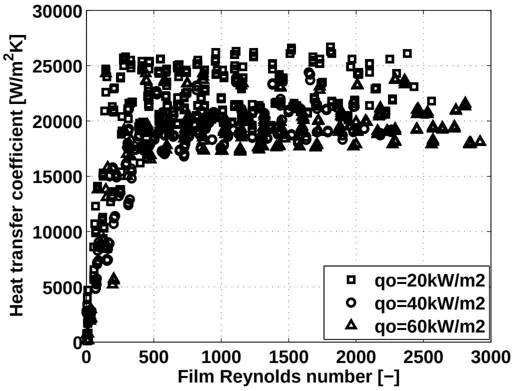

Figure 5.13: Falling film evaporation on Gewa-B at $T_{sat} = 5°C$ for R134a [3]

The falling film multipliers displayed in Fig. (5.14) show clearly that this structured surface gives better performance in falling film conditions than in pool boiling only for a heat flux of $q_o = 20kW/m^2$. For higher heat fluxes, the values of K_{ff} fall to between 0.5 and 1, apparently because for the lower values, some dryout inside the enhancement is occuring. This results in more scatter for R236fa, with K_{ff} values between 0.5 and 2. This may be explained by the steep slope of the pool boiling curve obtained for R236fa.

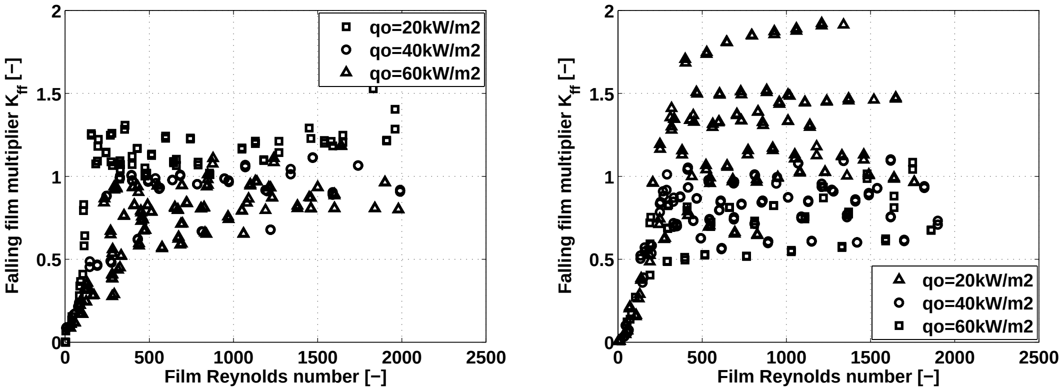

(a) R134a

(b) R236fa

Figure 5.14: Falling film multiplier K_{ff} on Gewa B4 at $T_{sat} = 5°C$ for R134a and R236fa

Turbo-EDE2 tube

Fig. (5.15) shows the falling film evaporation heat transfer performance of the enhanced boiling Turbo-EDE2 tube. This 3D-structured surface is a new version of the Turbo-BII enhanced surface tested by Roques [3]. As a first observation, this surface gives optimized performance for R134a at $q_o = 20kW/m^2$ with heat transfer coefficient values up to $80000W/m^2K$; the heat transfer coefficients obtained for 40 and $60kW/m^2$ represent only half of this value, with no apparent reason. Certain flow/heat flux conditions seem to greatly improve the performance. For R236fa, similar performance was observed for high heat fluxes with heat transfer coefficients around $40000W/m^2K$; the optimization for $q_o = 20kW/m^2$ is not as clear for R236fa, but values up to $60000W/m^2K$ were measured.

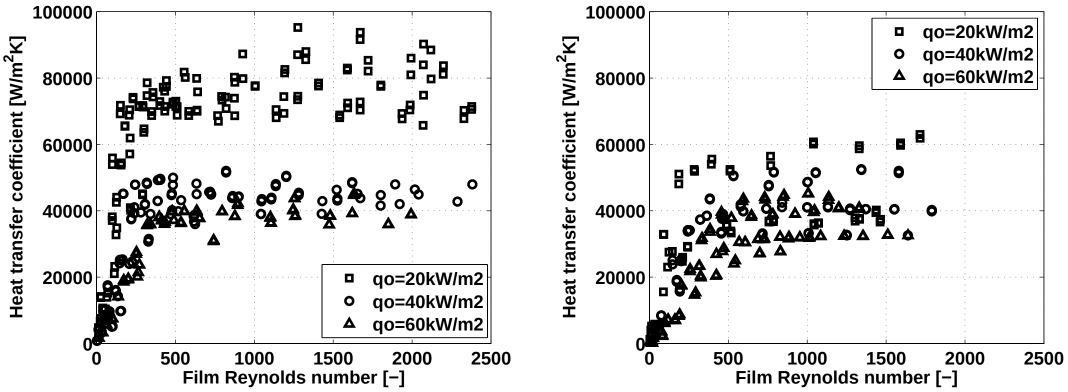

(a) R134a (b) R236fa

Figure 5.15: Falling film evaporation on Turbo-EDE2 at $T_{sat} = 5°C$ for R134a and R236fa

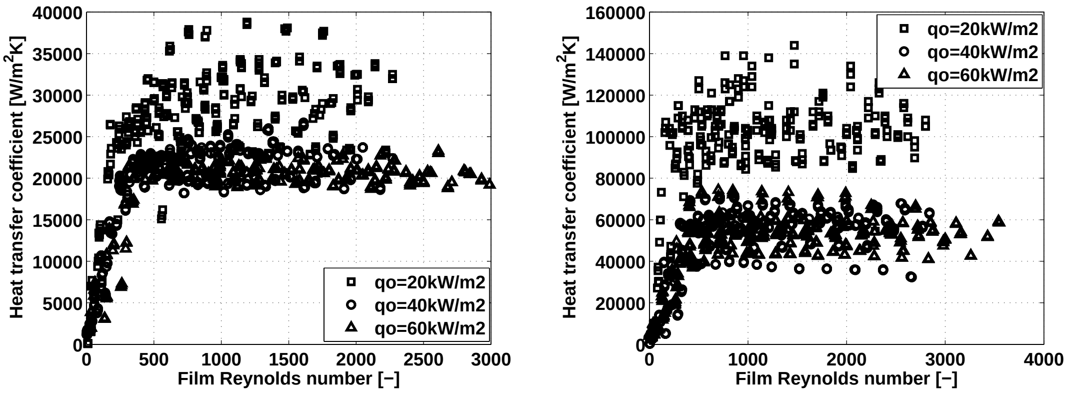

(a) Turbo-BII tube (b) High Flux tube

Figure 5.16: Falling film evaporation on Turbo-BII and High-Flux tubes at $T_{sat} = 5°C$ for R134a [3]

The Turbo-BII tube was also optimized for R134a and $q_o = 20kW/m^2$ as depicted in Fig. 5.16(a). The new version of this surface gave twice the performance of the previous one in falling film conditions, showing a large improvement of the enhanced boiling process by the new design with values at the lower heat flux surpassing $80000W/m^2K$. The

High-Flux tube tested by Roques is shown in Fig. 5.16(b) and gave similar performance to the Turbo-EDE2, which means that the performance of the Turbo-EDE2 surface can be said to mimic that of a metallic porous coated surface under falling film conditions. The enhanced boiling mechanisms involved in both surfaces present some similarities.

The falling film multipliers for this tube are displayed on Fig. (5.17). For R134a, the Turbo-EDE2 tube provided falling film heat transfer coefficients between 1.4 and 2.2 times larger than in pool boiling; the lower the heat flux density, the higher the falling film multiplier. For R236fa, the K_{ff} values were between 1.4 and 2 at 40 and $60kW/m^2$, but for $20kW/m^2$ the tube performed better in pool boiling conditions. Thus, there is strong evidence of an influence of falling film flow on the enhanced boiling heat transfer mechanisms.

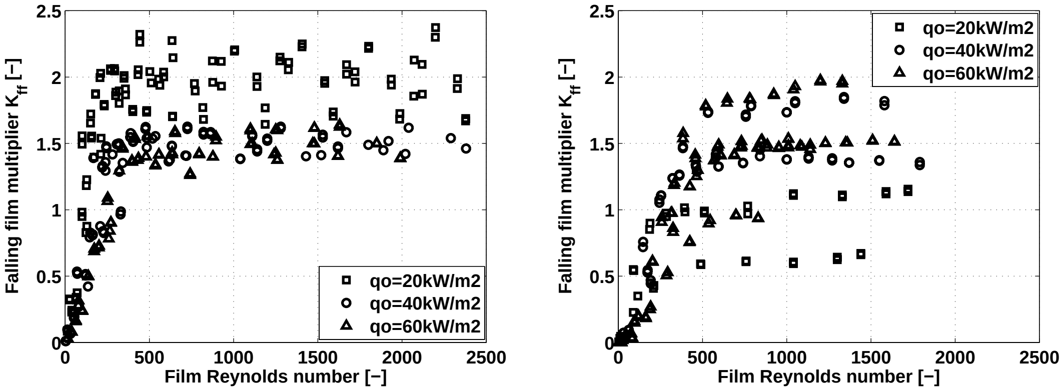

(a) R134a (b) R236fa

Figure 5.17: Falling film multiplier K_{ff} on Turbo-EDE2 at $T_{sat} = 5°C$ for R134a and R236fa

Visual observations

The three windows on the front of the test section were used during tests to make some visual observations regarding the liquid film flow, flow patterns and onset of dryout. Some of these observations are given in the present section.

Some bubbles are generated on the tube wall and are observed within the liquid film as shown in Fig. (5.18); their size increased with the heat flux. The bubble generation is also more intense on the two boiling enhanced tubes. As these surfaces are optimized for one fluid and one particular range of operating conditions, different characteristics were observed on the structured surfaces:

- small bubbles from one cavity site
- big bubbles on several cavity sites
- bubble collapsed due to jet impingement
- slinging bubbles

- film breakdown
- bubbly film flow, etc.

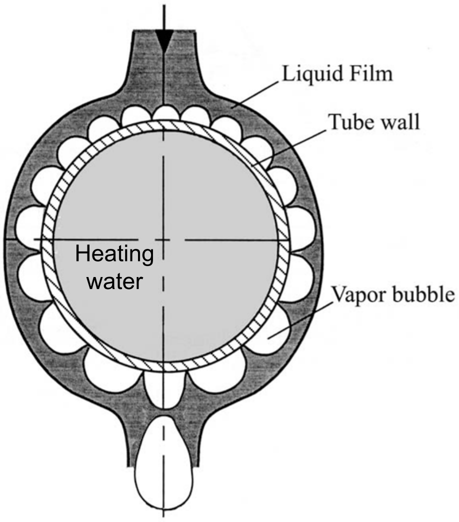

Figure 5.18: Schematic of the formation of the bubbly liquid film around the tube

The structure of enhanced tubes modifies the liquid flow. The structured tubes apparently give more stable, regular liquid columns and liquid films and the transition thresholds between the different flow modes are modified. The amplitude of this lateral movement and the liquid splashing out of the tube is reduced compared to the plain tube. Using R134a, the amount of liquid leaving the tube array is almost negligible. Liquid column/film deflection were observed mostly using R236fa, particularly at high heat fluxes.

Falling film evaporation needs further insight in order to relate experimental trends to local physical phenomena. Bubbles being carried by the film and the bubble nucleation on the upper region of the tubes promote a complex "two-phase" film flow between tubes as suggested by Ribatski and Thome [51].

5.3 Conclusions and remarks

Falling film evaporation measurements in a single-row tube array have been made with four different type of tubes for heat fluxes ranging from 20 to $60kW/m^2$. The same general trend as Roques [3] was observed with a mostly constant heat transfer coefficient for a given heat flux in the plateau region until the onset of dryout is reached, followed by increasing dryout of the surface with a rapid decrease of the heat transfer towards the vapor-phase heat transfer value at complete dryout. The heat transfer coefficients are strongly dependant on the heat flux and as expected, both enhanced boiling structured surfaces yielded significantly higher heat transfer performance compared to the plain surface at the same conditions.

Single tube pool boiling heat transfer data have been correlated for each enhanced surface and were used to determine the falling film multiplier for those tubes. Based on the estimation of K_{ff}, the choice of the structured surface can be adapted to the best application: falling film for low heat fluxes and pool boiling for high heat fluxes. The film Reynolds number at which film breakdown occurs is not only an important design parameter for the optimization of falling film heat exchangers, but also an important parameter for accurately predicting heat transfer in falling film evaporation. This aspect is investigated further in Chapter 7.

It should be pointed out here, however, that the enhanced falling film heat transfer coefficients become so large that the limits of the existing temperature measurement technology have been reached. For example, in Fig. 5.15(a), heat transfer coefficients as high as $80kW/m^2K$ were measured at a heat flux of $20kW/m^2$. This means that the temperature difference from the outside surface of the tube to the local saturation temperature is only 0.25K. However, even with very good calibrations and instrumentation, these values have a propagation of error on the order of ±20 to 30%. All the data presented in this chapter had a propagation of error less than 35%. Nonetheless, the data in most graphs are consistent and define definite trends.

Chapter 6

Results on falling film bundle evaporation

In this chapter, an analysis of the local heat transfer data is presented for the falling film evaporation on a small bundle. Some modifications were made on the original test rig to approximate the conditions of a falling film evaporator with a small bundle. Tests were run to determine the bundle effect on the local heat transfer coefficient. Tests were run using a plain tube bundle and three enhanced tube bundles for R134a and R236fa. Local heat transfer coefficients were measured at the center of each tube in the middle row of the small bundle. These are the first such local values obtained for falling film evaporation in a tube bundle (others have published tube length averaged values).

6.1 Bundle Modifications

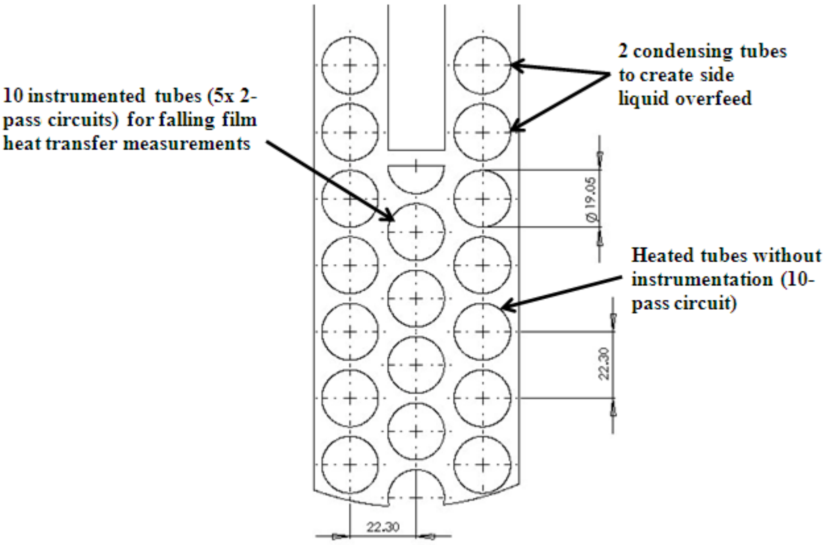
10 instrumented tubes (5x 2-pass circuits) for falling film heat transfer measurements
2 condensing tubes to create side liquid overfeed
Ø 19.05
Heated tubes without instrumentation (10-pass circuit)
22.30
22.30

Figure 6.1: Working principle of the bundle

The test facility was modified from its single row configuration to a tube bundle configuration, as shown in Fig. (6.1). The requirements were to create a variable liquid refrigerant overfeed on both side rows of the bundle (using two enhanced condensing tubes on either side), generate a bubbly liquid film by heating the side tubes (with a 10-pass circuit on each side row) and make sure that all these tubes on the side rows were wetted correctly. Due to space constraints in the stainless steel test section vessel, it was not possible to install a liquid feeder for all three rows of tube. Instead of that, two enhanced condensing tubes were installed on top of each side row to create a liquid film by condensing the saturated vapor. The two side columns each consist of a 10-pass circuit to heat the film, creating falling film evaporation with boiling similar to that of the middle row. The local heat transfer coefficient measurements were made only on the 10 instrumented tubes in the middle row as described in Chapter 4. For the side arrays, only the inlet and outlet temperatures were measured to control the amount of heat transferred.

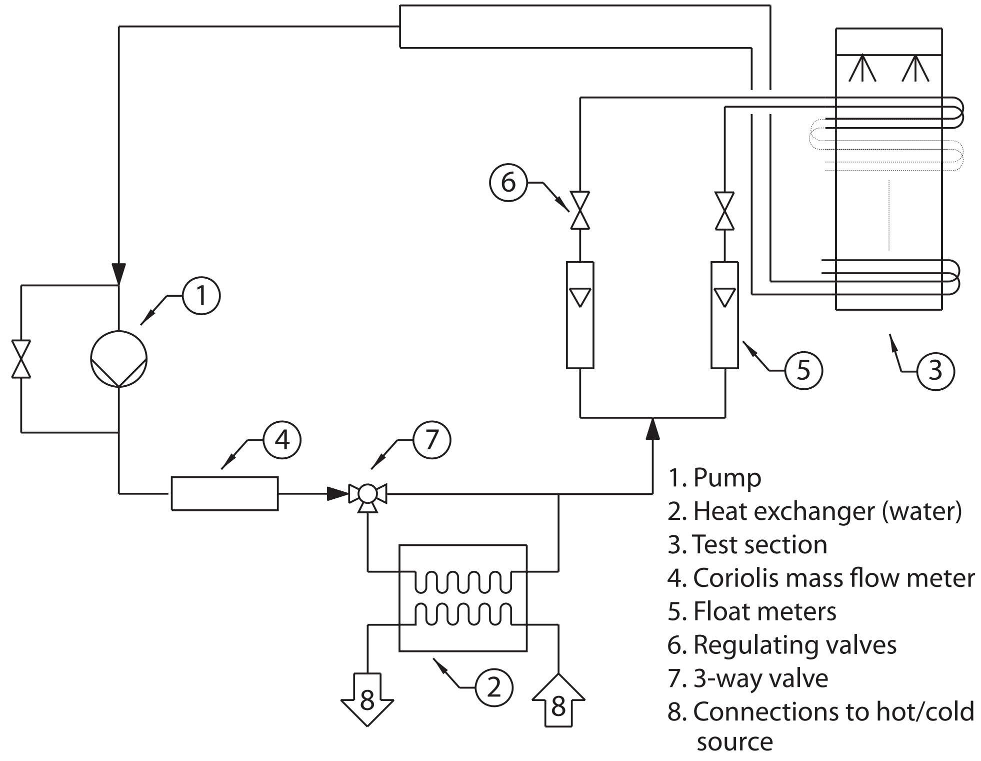
⑥
①
⑤
③
④
⑦
②
8
8
1. Pump
2. Heat exchanger (water)
3. Test section
4. Coriolis mass flow meter
5. Float meters
6. Regulating valves
7. 3-way valve
8. Connections to hot/cold source

Figure 6.2: Schematic of the new circuits used for the bundle

To achieve these test conditions, two new circuits were designed and added to the test facility: a glycol/water loop to supply an adjustable cooling power to the two condensing tubes on top of each side row and a water loop to supply a controlled heating power to heat up the 10-pass circuits on each side. Both circuits are based on the same principle as depicted in Fig. (6.2). The circuit starts with a centrifugal pump. The water/glycol or water then goes into a liquid-liquid plate heat exchanger, exchanging heat with a $15kW$ heating/cooling source. An adjustable valve with a bypass allows good precision in the temperature and mass flow rate control. The main flow is then split to two subcircuits before entering the test section. After the test section, the water/glycol or water flows from the sub-circuits merge and go back to the pump to complete the circuit. The total mass flow rate was measured with a Coriolis mass flow mater. Depending on the tubes used for the side rows (always the same as in the middle test row), side film Reynolds numbers up to 500 and heat rates up to $4000W$ could be reached based on the heating/cooling power available. It was not be possible to set the same conditions on the three rows, but symmetry was respected between the two side rows.

6.2 Measurement procedure

The experimental procedure for the falling film evaporation measurements on the vertical tube row was kept the same for the middle row in the bundle tests. The liquid overfeed on the side rows was obtained using the cooling circuit; the amount of refrigerant condensed on both sides was controlled by the flow rate and the inlet temperature of the water/glycol mixture. The 10-pass circuit was heated using the heating circuit; the heat flux on both sides was controlled by the flow rate and the inlet temperature of the water. A non-negligible difference in temperature between the top and the bottom of the test section was found with the bundle in the test section due to the pressure drop. The estimation of the saturation temperature was thus adapted accordingly: a linear interpolation was made between the temperatures obtained at the top and bottom to obtain the local saturation temperature at each tube elevation. This assumption is commonly used in bundle heat exchanger analysis.

In order to maximize the chances of analyzing the bundle effect on the heat transfer performance and trying to identify those parameters that are playing an important role, three different test conditions were made to decompose the bundle contribution as follows:

- no liquid film on the two side rows,
- adiabatic liquid films on the two side rows(i.e. no heat applied),
- “two-phase” liquid films on the two side rows (i.e. falling film evaporation similar to the middle row).

The measurement system used for the bundle tests was the same as before, including the new measurements (temperatures and flow rates for both circuits). To check the reliability and the reproducibility of the tests, different preliminary sets of measurements were performed and gave a very good agreement. Wilson plot and pool boiling measurements were also conducted and the results were found in agreement with the results shown previously in Chapter 5.

No significant differences were observed between the three different cases described before. The main contribution to the local bundle heat transfer coefficient seems to be due to the presence of a “two-phase” liquid film. The amount of vapor generated in the bundle increases significantly the pressure drop. In the following sections, only the tests with a “two-phase” liquid film on the two sides will be displayed and discussed.

6.3 Plain tube results

Falling film evaporation heat transfer results on a plain tube bundle are presented for R134a and R236fa with heat fluxes of 20, 40 and 60 kW/m^2 in Fig. (6.3) and Fig. (6.4). Local heat transfer coefficients for each tube are presented as a function of the film Reynolds number and the tube position (assuming ideal film flow down the row). The data points for each tube (numbered from top to bottom) were linked together to better visualize the trends.

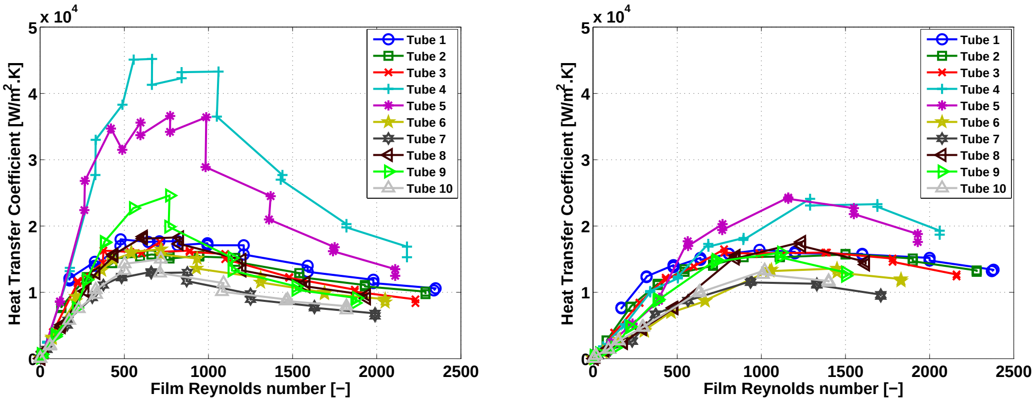

(a) $q_o = 20kW/m^2$ (b) $q_o = 40kW/m^2$

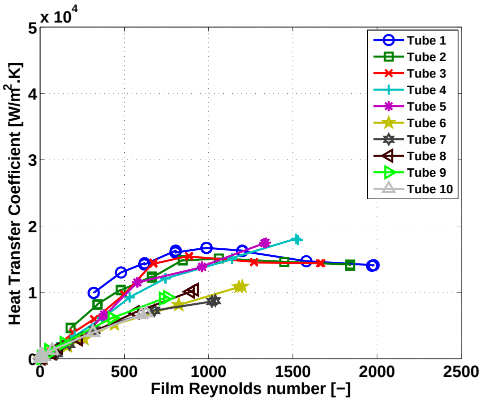

(c) $q_o = 60kW/m^2$

Figure 6.3: Bundle falling film coefficient on plain tube at $T_{sat} = 5°C$ for R134a

The heat transfer coefficients depicted in Fig. (6.3) are similar in magnitude to the results obtained by Roques [3] for his single row tube array. The heat transfer trend differs in some cases from the behavior observed with the single row; some of the data still illustrate the "plateau" and "fall-off" at the onset of dry patch formation, others have a distinct maximum and others even show a monotonic variation. These trends are particularly clear for $q_o = 20kW/m^2$ in Fig. 6.3(a), where the peak occurs at a film Reynolds number of about 650. A large scatter was found between the tubes: tubes 4 and 5 exhibit extremely high values despite a careful calibration, while the variation between the other tubes is about ±25%. This may be due to the liquid distribution within the bundle (e.g.: a lot of liquid splashes out onto the windows after the 3rd tube from the top, making the liquid film on the 4th and 5th tube thinner). The heat transfer coefficient decreases for large film Reynolds numbers and this effect tends to disappear when increasing the heat flux.

Therefore, it seems that liquid distribution within the bundle becomes an important issue: some liquid splashes out of the bundle; while some is transferred sideways between the 3 rows. The "liquid film" is in fact a two-phase bubbly layer flowing down over the tubes. Furthermore, the bundle layout is extremely compact because of the limited width of the test section, with a spacing of only 1.5mm between the 3 rows of tubes creating some interactions between the side and middle liquid films. The tube pitch and bundle layout was as recommended by our industrial sponsors.

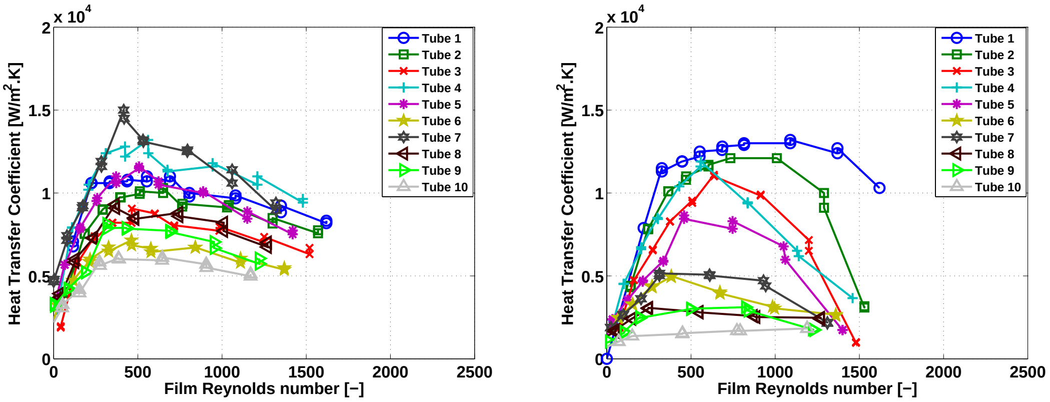

(a) $q_o = 20kW/m^2$ (b) $q_o = 40kW/m^2$

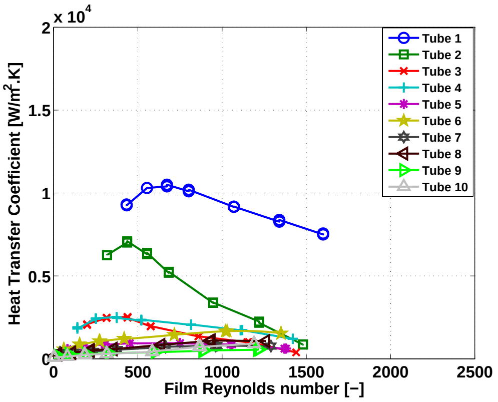

(c) $q_o = 60kW/m^2$

Figure 6.4: Bundle falling film coefficient on plain tube at $T_{sat} = 5°C$ for R236fa

The bundle measurements for R236fa are displayed in Fig. (6.4) and show first that the liquid distribution problems are even more important for R236fa than for R134a. When the heat flux is increased, dryout appears early at the bottom of the middle row and thus the performance of the bundle falls dramatically. For $q_o = 20kW/m^2$, the heat transfer coefficients vary significantly among the different tubes and tubes 4 and 7 give better performance than the others. For higher heat fluxes, the trends observed for R134a are amplified: the heat transfer first increases to a maximum before decreasing gradually and for the highest heat flux, most of the tubes appeared to be progressively dry (even though the liquid overfeed is more than sufficient to wet all tubes at this heat flux). Potentially this means that a significant part of the liquid is transported without contracting the tube surface (i.e. by the bubbly layer) and hence early dryout can be encountered. The falling film heat transfer performance using R236fa seems to be enhanced compared to the single array (refer to Chapter 5 on Fig. 5.4(a)), which was not the case using R134a. The fluid properties are an important parameter to consider; the hydrodynamics is strongly dependant on these physical properties.

The visualization windows on the test section were not sufficient to see the liquid distribution within the bundle on the middle row: only the amount of liquid leaving the bundle from the side could be observed. The films are in fact two-phase with numerous bubbles entrained, which greatly increases the film thickness. Fig. 6.5(a) shows a ideal distribution of the liquid film through the bundle. This ideal behavior does not seem to be verified by the heat transfer coefficients measured in the 3-row bundle configuration.

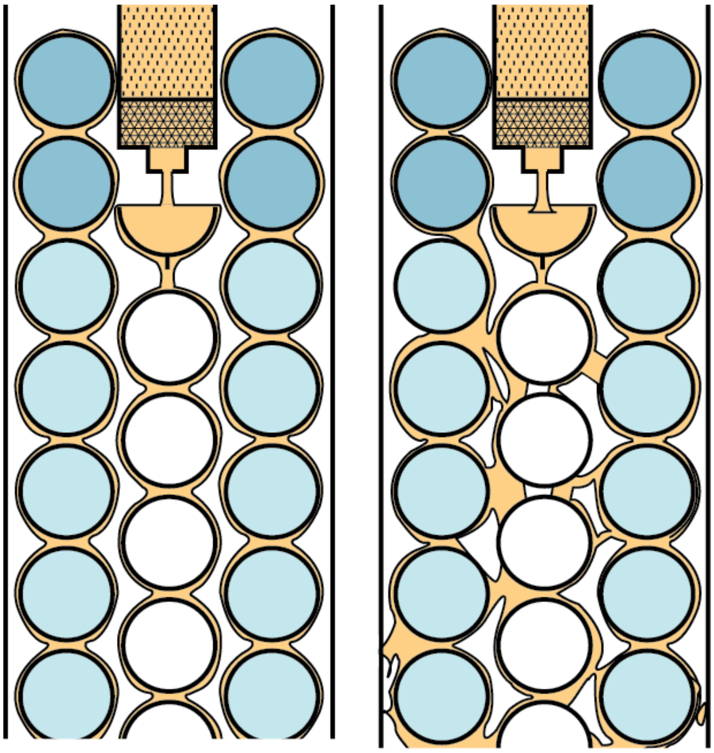

(a) ideal case (b) real case

Figure 6.5: Liquid distribution within the tube bundle

The compactness of the bundle may also play a role in this distribution; because of the close spacing between the tube rows, the two-phase films will probably create a bubbly flow regime within the bundle. In practice, the film may also be transferred from one row to another. For example, if the liquid bridges onto the two side rows, the tube directly below could be starved of liquid and have premature dry patches, greatly affecting its heat transfer coefficient (Fig. 6.5(b)). The shear at the liquid/vapor interface is increased in the bundle because of the confinement, which can also have an impact on the results.

6.4 Enhanced surface results

The falling film evaporation bundle experiments using enhanced surface tubes gave very large propagations of error because of their very large heat transfer coefficients, often greater than $50000W/m^2K$. The modified Wilson Plot method developed at LTCM reached its limits as will be explained in Section 6.5. In order to provide only relevant data, only the measurement points with an uncertainty lower than 35% have been retained for the analysis.

6.4.1 Gewa-C+LW

Fig. (6.6) and Fig. (6.7) show the results obtained for the Gewa-C+LW tube bundle for R134a and R236fa. The results obtained for $q_o = 20kW/m^2$ were few because of their high propagation of errors. Tube 1 results have also been removed for $q_o = 40kW/m^2$ because of an apparent high impinging jet effect.

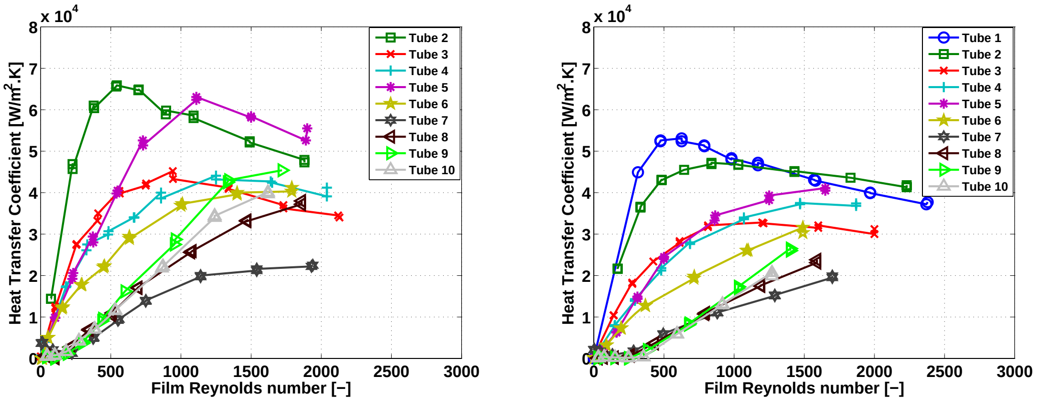

(a) $q_o = 40kW/m^2$ (b) $q_o = 60kW/m^2$

Figure 6.6: Bundle falling film coefficient on Gewa-C+LW at $T_{sat} = 5°C$ for R134a

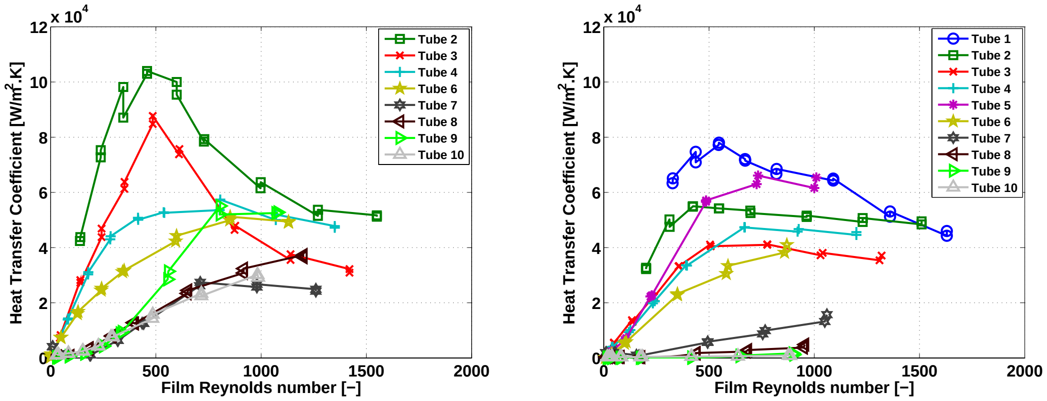

(a) $q_o = 40kW/m^2$ (b) $q_o = 60kW/m^2$

Figure 6.7: Bundle falling film coefficient on Gewa-C+LW at $T_{sat} = 5°C$ for R236fa

Similar trends are observed for both fluids: h_o increases and then decreases with bundle depth. The top-most tubes always show a higher performance (with a maximum peak around Re=500) before declining. The single-row tests in Chapter 5 did not display such a large decreasing trend as in the bundle and hence this can be defined as a bundle effect. All the tubes' performance seem to converge for increasing Re to a value close to the single array plateau value; that is, the bundle tends to perform better that the single row at intermediate film Reynolds number. The performance also decreases with increasing heat flux. Surprisingly, the tube performed better with R236fa than with R134a. From this results, it can only be said that this tube was optimized for R134a condensation, not falling film evaporation.

6.4.2 Gewa B4

The results obtained with the Gewa-B4 tube bundle for R236fa were quite scattered due to their very high uncertainties (> 35%). Thus, for the same reason only R134a results are represented in Fig. (6.8) for the higher two heat flux levels.

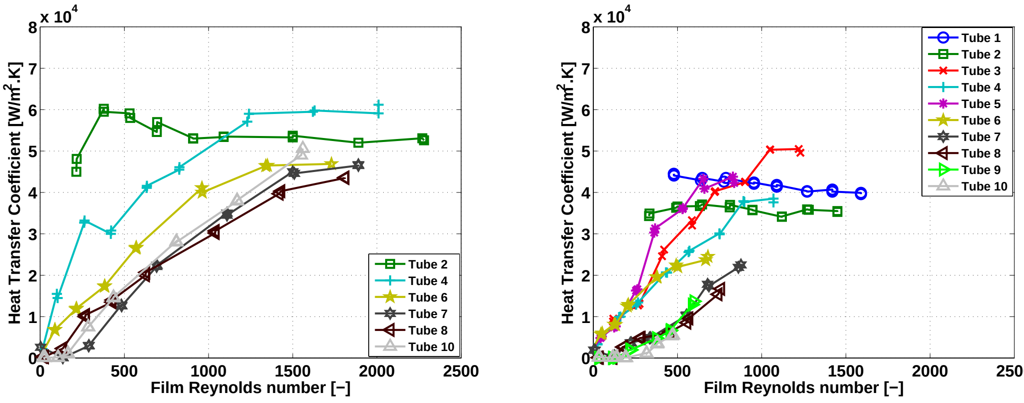

(a) $q_o = 40kW/m^2$ (b) $q_o = 60kW/m^2$

Figure 6.8: Bundle falling film coefficient on Gewa-B4 at $T_{sat} = 5°C$ for R134a

Similar comments as for the previous tube can be made here. The most remarkable result here is that the enhanced condensing tube (Gewa-C+LW) gave similar performance as the enhanced boiling tube (Gewa-B4), probably because of the poor wetting of the fins. The measured heat transfer coefficients in the bundle in Fig. (6.8) are in some cases as large as those on the single-row tests shown in Fig. 5.15(a) but many are smaller, thus again illustrating a pronounced negative bundle effect.

6.4.3 Turbo-EDE2

Fig. (6.9) and Fig. (6.10) show the results obtained for the Turbo-EDE2 tube bundle with respectively R134a and R236fa. The results obtained for $q_o = 20kW/m^2$ were not relevant because of their large propagation of errors and are not shown. The results obtained with R236fa for tubes 2, 4 and 6 were removed for the same reasons.

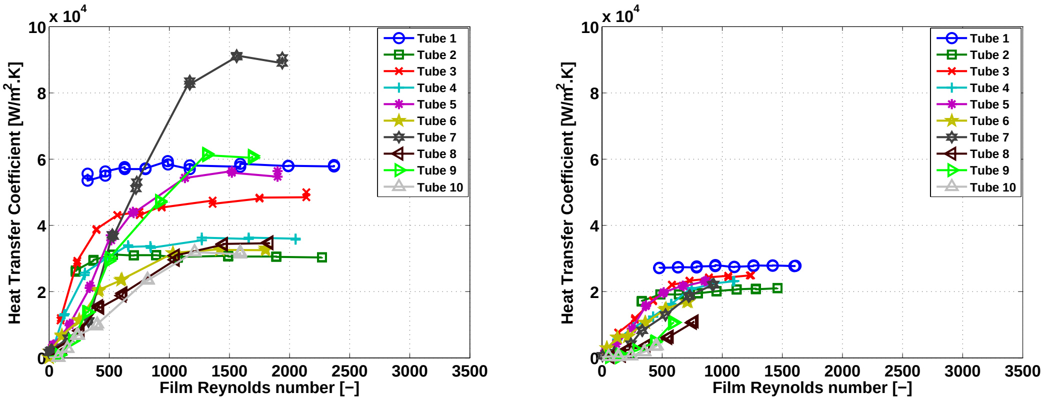

(a) $q_o = 40kW/m^2$ (b) $q_o = 60kW/m^2$

Figure 6.9: Bundle falling film coefficient on Turbo-EDE2 at $T_{sat} = 5°C$ for R134a

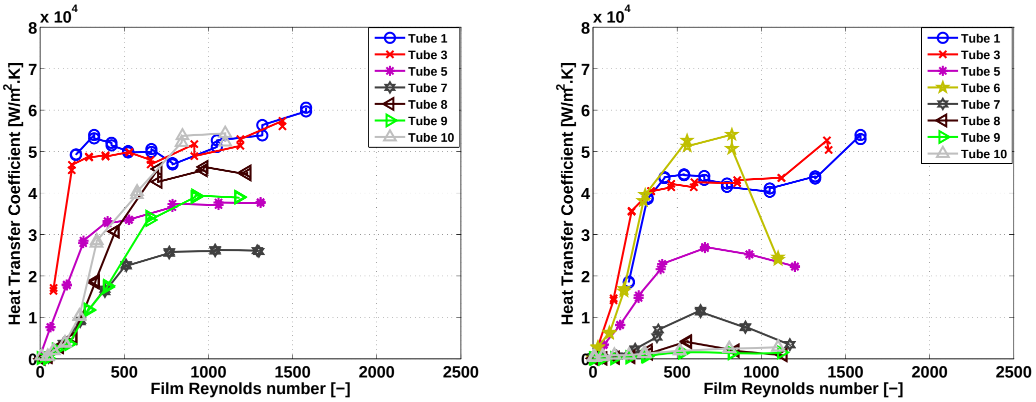

(a) $q_o = 40kW/m^2$ (b) $q_o = 60kW/m^2$

Figure 6.10: Bundle falling film coefficient on Turbo-EDE2 at $T_{sat} = 5°C$ for R236fa

Different trends are observed for the two fluids. For R134a, all the tubes seem to approximately converge to a plateau for Re increasing with a value corresponding to the single array plateau value. For R236fa, the bundle performance is more adversely affected and for $q_o = 60kW/m^2$, the tubes located at the bottom of the bundle apparently are mostly dry. The onset of dryout prediction becomes difficult because of the apparently poor liquid distribution or because of a large fraction of liquid transported in the bubbly flow that in effect is not available on the tube surface. The upper tubes always show a higher performance (with a maximum peak around $Re = 500$). The heat transfer performance decreases with increasing heat flux. Similar or higher performance was measured using R236fa depending on the heat flux.

6.5 Critical analysis of the Wilson plot method

As noted earlier, the propagation of error limits the accuracy of the measurements made on the enhanced surfaces. The external heat transfer coefficients were often extremely high, inducing high uncertainties in our modified Wilson plot method, with uncertainties often surpassing 35%. The following comments can be made regarding the measurement method utilized here:

1. The Wilson plot method is accurate when the value of the external heat transfer coefficient is smaller or equal to the inside one. For the enhanced tubes here, instead, usually $h_i \ll h_o$,

2. Using the LMTD method to estimate the overall heat transfer coefficient becomes untenable due to the small temperature difference between the heating water and the saturation temperature,

3. $(T_{wat,in} - T_{wat,out})$ also becomes too small to be accurately measured and obtain accurate heat duty, increasing the uncertainty in the U_o calculation,

4. The pressure drop over the tube bundle induces a variation of T_{sat} within the bundle. A linear saturation temperature profile was assumed between top and bottom, which induces some additional uncertainties when LMTDs are so small.

Several solutions might improve the experimental set-up for more precise measurements in the future. A much higher internal heat transfer coefficient is required to get a good estimation of the external one. However, the internal enhancement for the water-side is already at the limit of what the tube producers can obtain. The internal heat transfer coefficient could be increased by a higher flow rate by adding another stage on the pump but then the water temperature difference becomes too small to measure with adequate precision. The test section could be extended in length to allow tests on longer tubes; this would increase the water temperature difference to be measured but would be a very expensive solution (in fact, the refrigeration system of the lab would not be large enough to handle the heat duty of such a test bundle). Presently, a compromise was found between the internal heat transfer coefficients and the water temperature differences.

6.6 Trend analysis

The decrease in local heat transfer coefficients is explainable by reasoning about the appearance of premature local dryout in the bundle due to non-uniform liquid flow within the bundle. With the creation of a bubbly flow regime in the bundle, it may be that so much liquid is held in the bubbly film between the tubes that there is not sufficient liquid to continuously wet the tubes on a local basis, thus creating another mechanism for premature local dryout. With respect to the enhanced boiling tubes, this lack of sufficient liquid will lead to dryout of the re-entrant channels and thus very poor performance.

On the other hand, the results showed very high thermal performance trends occurring on the upper tube rows of the enhanced tube bundles. Hence, it should be possible to create favorable conditions in the entire bundle to obtain uniformly good performance.

6.7 Conclusions and remarks

Falling film evaporation measurements on a tube bundle have been made with four different type of tubes for heat fluxes 20 to $60kW/m^2$ for two different refrigerants. Different trends were observed depending of the type of tube, but bundle effects were quite evident with respect to the single-row test results in Chapter 5. In general, the bundle effects were detrimental to thermal performance. The hydrodynamics of the liquid film appear to be the key parameter. The assumption of ideal liquid flow has to be reconsidered to take into account the non-uniformities of flow occurring in the bundle. In the future, a visualization technique should be developed to investigate film hydrodynamics on the heat transfer coefficient. This visualization technique could be inspired by the flow pattern instrumentation and visualization systems developed by Agostini [85] for bundle boiling.

Chapter 7

Heat transfer models

In this chapter, the falling film evaporation results were processed to obtain empirical prediction methods for the onset of dry patch formation and heat transfer. As a premise, the methods should be capable of providing accurate thermal designs of a falling film evaporator based on a single pool boiling curve as the starting point. According to the trends observed with the different surfaces, the falling film evaporation prediction will be decomposed into four steps, following the method proposed by Ribatski and Thome [64]:

1. Prediction of the onset of film Reynolds number Re_{onset} characterizing the onset of film breakdown/dryout to define the limit between all-wet and partially-wet tube operation;
2. Prediction of the heat transfer coefficient for the all-wet region characterized by a large plateau on a single-row;
3. Prediction of the heat transfer coefficient for the partially-wet region characterized by a rapid decrease of the heat transfer coefficient with increasing dry area fraction on a single-row;
4. Prediction of the bundle effect with respect to the single-row performance.

Focus will be made primarily on the all-wet data, as they are the most important for actual applications. It is important to mention that a general agreement was reached with the tube companies sponsoring the project not to give any close-up diagrams, photographs or descriptions of the enhanced tubes.

7.1 Onset of film breakdown prediction

To characterize the onset of dryout the following approach was adopted: it was assumed that by decreasing the film flow rate in small steps from a high value at a fixed heat flux, the transition from no-dryout to dryout would occur at a film flow rate just at the first dryout patch formation. The criterion defined by Ribatski (see Eq. (2.36)) was used to determine the onset of the film breakdown formation. The results obtained for all four surfaces are shown on Fig. (7.1), where it was found that the characteristic film Reynolds number was primarily a function of heat flux for all types of tubes for the two fluids, i.e. 8 fluid/surface combinations. The onset of film breakdown Reynolds number increases with increasing heat flux for all tested surfaces following a similar trend for both fluids. The fluid physical properties do not seem to affect the onset of film breakdown for the plain tube and the two enhanced boiling tubes, as they have similar values of Re_{onset}. A single form of prediction can be used for these tubes, as the Turbo-EDE2 and Gewa-B4 can be compared to a smooth tube with a high roughness. The Gewa-C+LW tube gives a higher Re_{onset} than the other enhanced tubes for R134a but is quite similar for R236fa. For example, at $q_o = 60kW/m^2$ the Re values are either about 400-430 or about 580-620. Since some of the liquid is used to wet the inside of the enhanced surface tubes (i.e. more surface area to wet), it is not surprising that the onset of dryout happens at a lower heat flux for five out of six conditions for the enhanced tubes relative to the plain tube..

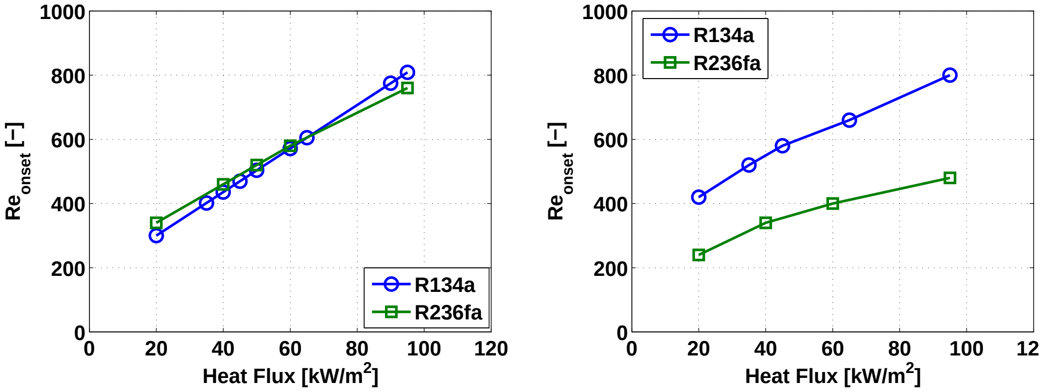

(a) Plain tube (b) Gewa-C+LW tube

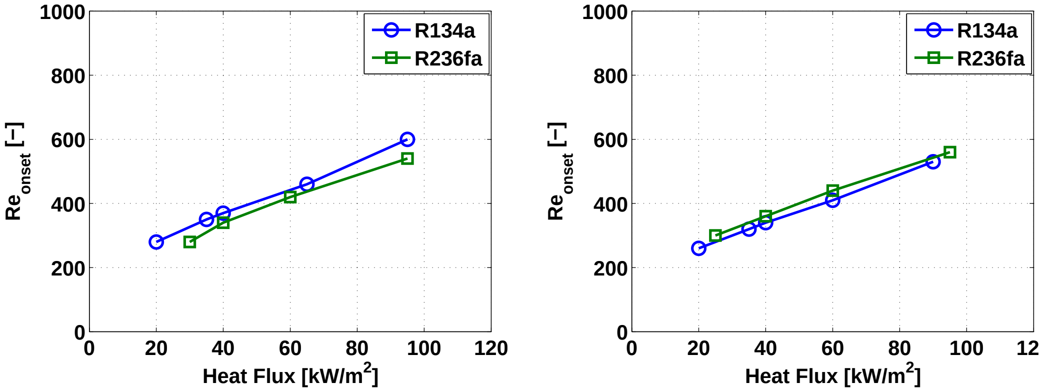

(c) Gewa-B4 tube (d) Turbo-EDE2 tube

Figure 7.1: Film breakdown Reynolds number as a function of heat flux for each tube

The onset of film breakdown was defined empirically by Roques [3] as as a linear function of the heat flux (see Eq. (7.1)):

$$Re_{onset} = cq_o + d \qquad (7.1)$$

	R134a		R236fa	
Tube	c	d	c	d
Plain	3.39e-3	82.3	8.42e-3	569.2
Gewa-C+LW	4.92e-3	340.0	3.10e-3	198.2
Gewa-B4	4.18e-3	159.0	3.90e-3	175.7
Turbo-EDE2	3.54e-3	144.5	3.71e-3	211.0

Table 7.1: Coefficients for the film breakdown correlation from Roques (Eq. (7.1))

The values of c and d are given in Table 7.1 for all four tubes. Roques' prediction method does not take into account any fluid property effect, except for the viscosity in Re. For adiabatic measurements, when the heat flux is equal to zero, the value of Re_{onset} should be equal to zero. The previous method works well within the range of experimental conditions but not when extrapolated to adiabatic conditions. Based on a parameter analysis, Ribatski and Thome [64] proposed the following expression for the plain tube with R134a as a function of the heat flux and the fluid properties:

$$Re_{onset} = a\left(\frac{q_o}{(\rho_L-\rho_V)H_{LV}^{3/2}}\right)^b \tag{7.2}$$

This method, originally developed only with a R134a database, does not thus reflect the fluid effect. However, the form of the equation can be adapted to both diabatic and adiabatic conditions. The resulting coefficients applied to the present data are shown in Table 7.2.

	R134a		R236fa	
Tube	a	b	a	b
Plain	$3.237 \cdot 10^6$	0.647	$6.474 \cdot 10^6$	0.649
Gewa-C+LW	$2.327 \cdot 10^5$	0.408	$2.200 \cdot 10^5$	0.445
Gewa-B4	$9.249 \cdot 10^5$	0.534	$1.228 \cdot 10^6$	0.560
Turbo-EDE2	$6.691 \cdot 10^5$	0.522	$3.503 \cdot 10^5$	0.470

Table 7.2: Coefficients for the film breakdown correlation from Ribatski (Eq. (7.2))

The experimental parameters and fluid properties that significantly vary between the two fluids and that could affect the onset of dryout are q_o, the liquid viscosity μ_L, the latent heat of vaporization H_{LV} and the tube diameter D. A parameter analysis leads to the following dimensionless expression:

$$Re_{onset} = e\left(\frac{q_o D}{\mu_L H_{LV}}\right)^f \tag{7.3}$$

Applied to the plain, Gewa-B4 and Turbo-EDE2 tubes for both fluids, the following expression predicts 81.2% of the data within ±20% for the whole database:

$$Re_{onset} = 95.3 \left(\frac{q_o D}{\mu_L H_{LV}} \right)^{0.5364} \tag{7.4}$$

While the new prediction method performs well at low and moderate heat fluxes, when reaching higher heat fluxes the method loses some precision as the estimation of the film Reynolds dryout location becomes less accurate. Further experimental research is suggested here in order to investigate tube diameter effects, which probably affect, in some manner, the onset of dryout.

Using a similar expression, a prediction for the Gewa-C+LW tube was found with a precision of 100% of the data within ±20% (see Eq. (7.5)). The reduced pressure was added to take into account the fluid effect observed on this finned tube. It could be interesting to apply this shape of equation to a larger database of different fluids.

$$Re_{onset} = 2573.1 p_r \left(\frac{q_o D}{\mu_L H_{LV}} \right)^{0.389} \tag{7.5}$$

Eq. (7.3) was used to fit the onset of dryout data obtained and presented by Roques [3] with the Turbo-BII HP, Gewa-B and High-Flux tubes for R134a. As previously, a single equation was sufficient for both the Gewa-B and Turbo-BII tubes, with the assumption that there is no reduced pressure effect:

$$Re_{onset} = 29 \left(\frac{q_o D}{\mu_L H_{LV}} \right)^{0.83} \tag{7.6}$$

Eq. (7.6) gives an agreement of 100% of the data within ±15% for both enhanced tubes. The onset of dryout for the High-Flux tubes can be described with a similar precision by Eq. (7.7):

$$Re_{onset} = 6.4 \left(\frac{q_o D}{\mu_L H_{LV}} \right)^{1.26} \tag{7.7}$$

The new expression proposed for the onset of film breakdown takes into account fluid properties and heat flux effects and gives a good agreement based on a large database. For the plain and enhanced tubes tested here, excluding only the R134a data for the Gewa-C+LW tube, the following expression (Eq. (7.8)) was found with an agreement of 81.6% of the data within ±30% for 10 tube/fluid combinations out of 11 total (including the High-Flux tube, the Turbo-BII tube and the Gewa-B tube). Utilizing this expression, the location of the onset of dryout in a tube bundle can be determined from a row by row energy balance starting at the top of the bundle and the rate of overfeed required to avoid the onset of dryout can be calculated or the number of tubes adjusted.

$$Re_{onset} = 65.8 \left(\frac{q_o D}{\mu_L H_{LV}} \right)^{0.63} \tag{7.8}$$

7.2 New heat transfer prediction method for single-array

The method proposed by Ribatski and Thome [64] and described in Chapter 2.6.1 gives good agreement for both dryout and non-dryout conditions for the plain tube with R134a, and is a good starting point for a prediction method for falling film evaporation on a single-row array. Here, the idea was to extend this method to other surfaces and other fluids and simplify it.

According to that method, the falling film heat transfer coefficient is given by Eq. (2.37). The heat transfer coefficient for the dry region h_{dry}, obtained using the natural convection equation defined by Churchill and Chu [24], has a negligible contribution to the calculation of h_o. As $h_{dry} \ll h_{wet}$, the heat transfer coefficient can be simply expressed using a linear expression:

$$h_o = F h_{wet} \tag{7.9}$$

where F represents the fraction of the tube surface covered by liquid.

Optimally, F and h_{wet} should be predicted with a minimum of empirical constants. The prediction method should also be as simple as possible and based only on the pool boiling curve for a given tube.

7.2.1 Apparent wet fraction area

The apparent wet fraction area F defined in [64] is backed out from the non-linear system of equations represented by Eq. (7.10):

$$\begin{cases} h_o = h_{wet} F + h_{dry}(1 - F) \\ q_o = q_{wet} F + q_{dry}(1 - F) \end{cases} \tag{7.10}$$

Following carefully the prediction method originally developed for the plain tube with R134a, the following coefficients were obtained for the new database (see Table 7.3). Depending on the initial conditions and on the solver, the resolution of this system can be quite erratic and lead to different results. Thus, this method also requires a large database to implement and the values of F have to be sorted carefully because of the scatter given by the system resolution.

The method gives good results for the prediction of F, but requires two fluid/surface dependent empirical constants to be determined for each combination. Based on the values of F backed out from the partially-wet experimental data, it is clear that a linear shape can also be used for the prediction of the onset of dryout. With an aim of simplification, a new prediction for the apparent wet fraction area is proposed using Eq. (7.11), taking into account both the heat flux and fluid property effects:

	R134a		R236fa	
Tube	a	b	a	b
Plain	0.0024	0.91	0.0011	1.19
Gewa-C+LW	0.0003	1.51	0.0160	0.68
Gewa-B4	0.0114	0.80	0.0591	0.46
Turbo-EDE2	0.0016	1.21	0.0206	0.67

Table 7.3: Coefficients for the apparent wet fraction area F from Ribatski (Eq. (2.39))

$$F = \begin{cases} Re_{top}/Re_{onset} & \text{for } Re < Re_{onset} \\ 1 & \text{for } Re \geq Re_{onset} \end{cases} \tag{7.11}$$

This method has the advantage of being simple to use and is based on Re_{onset} that is already given by Eq. (7.8). No additional empirical constant is needed and the value of F can be directly calculated. For values of film Reynolds numbers higher than Re_{onset}, F is then equal to 1 (no dry patches) as was the case for the previous prediction method. Knowing now how to predict F, an accurate prediction method is thus needed for h_{wet}.

7.2.2 Wet heat transfer coefficient

The local heat transfer coefficients were segregated using Ribatski's criterion (see Eq. (2.36)). The wet heat transfer coefficients h_{wet} were correlated as a power function of q_{wet}, leading to the predictions represented on Fig. (7.2) to Fig. (7.5). A good agreement was found for each tube and fluid, with a precision of 80% of the data being predicted within ±30% or better. Optimally, h_{wet} should be obtained directly from the pool boiling curve of the particular enhanced tube (for which no general method is available), and which can be easily measured by the manufacturing companies themselves.

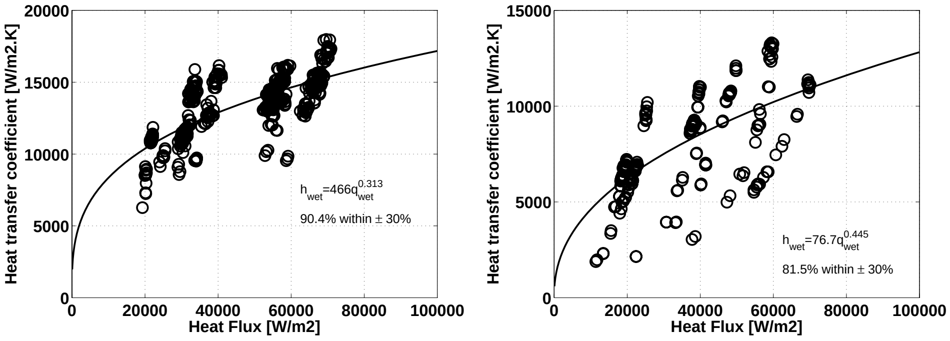

(a) R134a (b) R236fa

Figure 7.2: Falling film evaporation wet data on plain tube at $T_{sat} = 5°C$

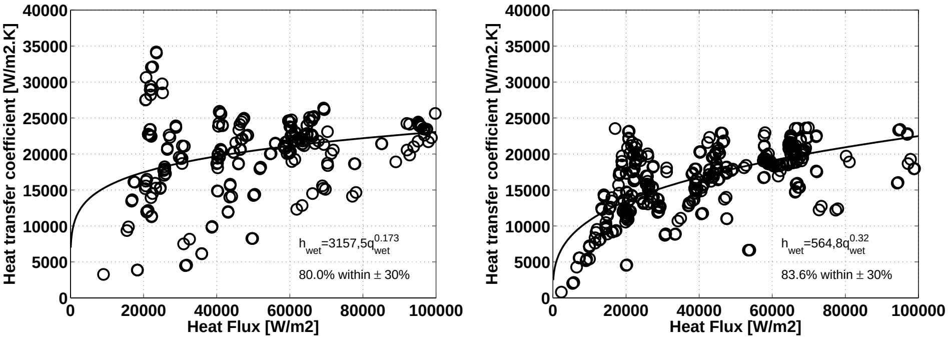

(a) R134a (b) R236fa

Figure 7.3: Falling film evaporation wet data on Gewa-C+LW at $T_{sat} = 5°C$

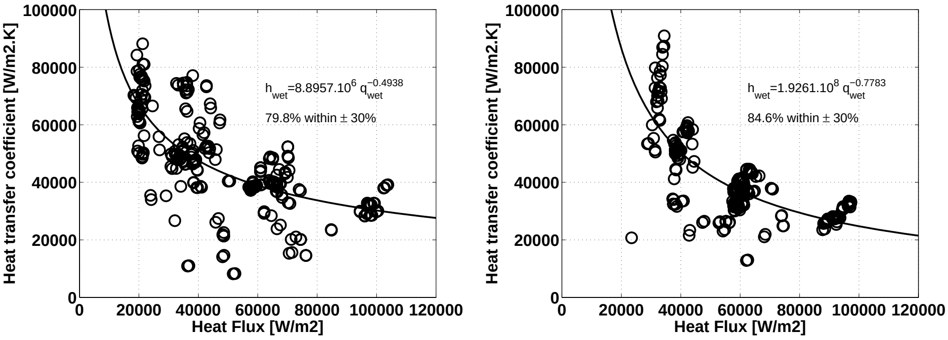

(a) R134a (b) R236fa

Figure 7.4: Falling film evaporation wet data on Gewa-B4 at $T_{sat} = 5°C$

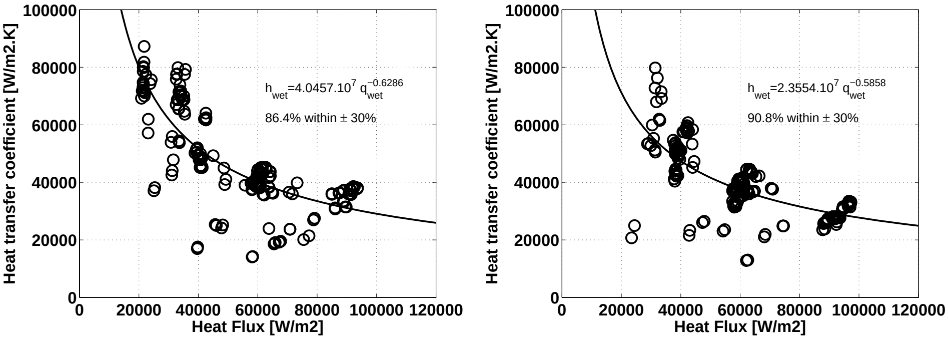

(a) R134a (b) R236fa

Figure 7.5: Falling film evaporation wet data on Turbo-EDE2 at $T_{sat} = 5°C$

Roques [3] proposed a prediction method of $K_{ff,wet}$ (see Eq. (2.32)) as a polynomial function of the ratio of the local heat flux to Kutateladze's critical heat flux. This method requires 5 empirical constants, in part to take into account the tube pitch effect. As this effect is quite limited and the present database was made for a fixed tube pitch typical of eventual applications, a simplified empirical prediction was found with two empirical constants, and which has the advantage of being non-dimensional:

$$K_{ff,wet} = c\left(\frac{q_o}{q_{crit}}\right)^d \tag{7.12}$$

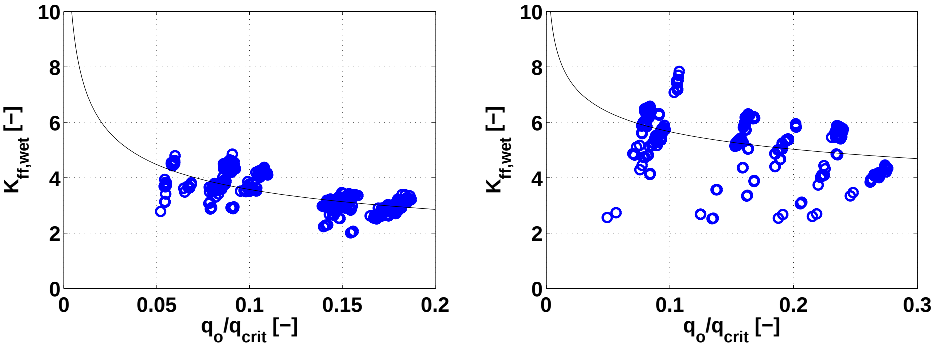

(a) R134a (b) R236fa

Figure 7.6: $K_{ff,wet}$ vs q_o/q_{crit} on plain tube at $T_{sat} = 5°C$

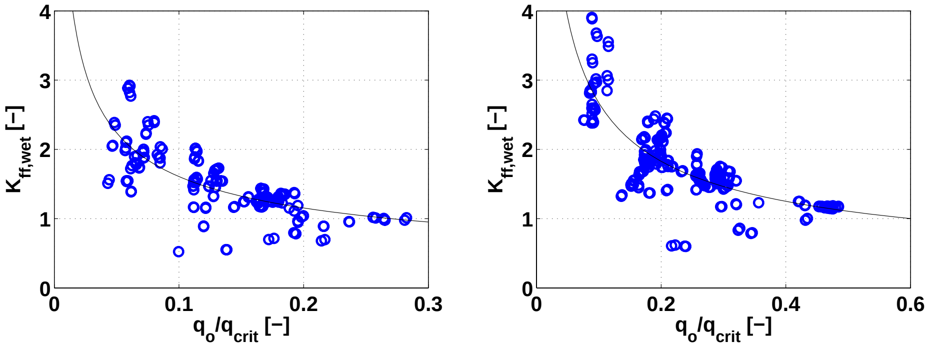

(a) R134a (b) R236fa

Figure 7.7: $K_{ff,wet}$ vs q_o/q_{crit} on Gewa-C+LW at $T_{sat} = 5°C$

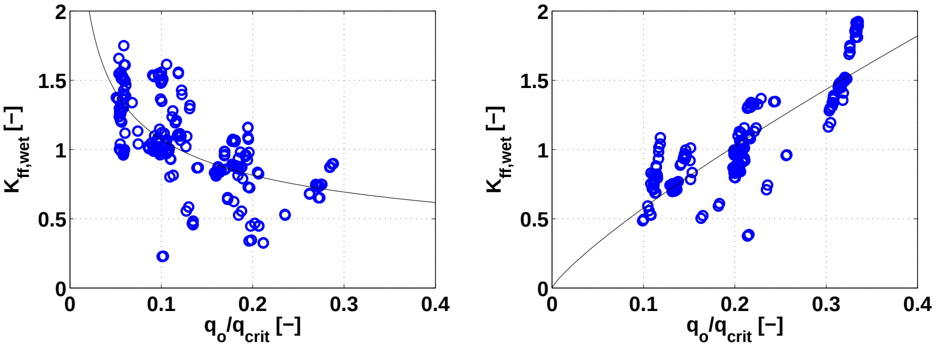

(a) R134a (b) R236fa

Figure 7.8: $K_{ff,wet}$ vs q_o/q_{crit} on Gewa-B4 at $T_{sat} = 5°C$

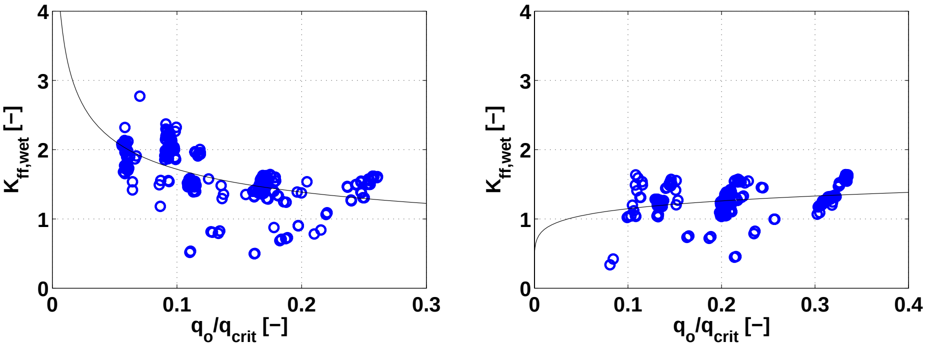

(a) R134a (b) R236fa

Figure 7.9: $K_{ff,wet}$ vs q_o/q_{crit} on Turbo-EDE2 at $T_{sat} = 5°C$

Fig. (7.6) to Fig. (7.9) show the evolution of the wet falling film multiplier with the non-dimensionalized heat flux. The corresponding empirical coefficients c and d are given in Table 7.4.

	R134a		R236fa	
Tube	c	d	c	d
Plain	1.6951	-0.324	3.8124	-0.172
Gewa-C+LW	0.3097	-0.774	0.7599	-0.533
Gewa-B4	0.4288	-0.396	3.8898	0.828
Turbo-EDE2	0.8497	-0.306	1.5650	0.135

Table 7.4: Coefficients for $K_{ff,wet}$ for the new database

It was not possible to collapse all the data onto one set of constants c and d. As such, further investigations will be necessary to develop a method that includes the effect of fluid properties and surface geometry in an expression with one set of constants apparently reflects how the particular surface interacts with the falling bubbly film.

The present method can be generalized and gives also good agreement when applied to the database of Roques [3] using the empirical constants displayed in Table 7.5 (see Fig. (7.10)). While the data can thus be approximately captured, the large propagation of error (up to 35%) in these database results are still responsible for a part of the scatter. Local film flow and distribution effects are responsible for the rest of the scatter.

Tube	c	d
Gewa-B	0.8252	-0.118
Turbo-BII	1.1453	0.037
High-Flux	2.0508	0.234

Table 7.5: Coefficients for $K_{ff,wet}$ for Roques' R134a-database [3]

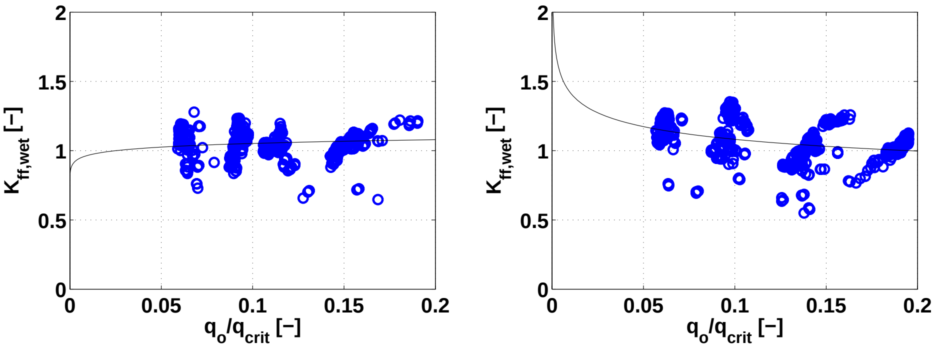

(a) Turbo-BII (b) Gewa-B

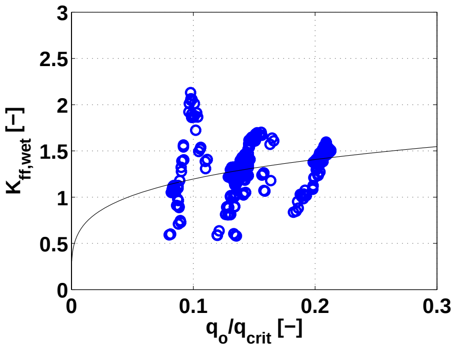

(c) High-Flux

Figure 7.10: $K_{ff,wet}$ vs q_o/q_{crit} on Roques' database [3]

Finally, using the empirical prediction method described in this section, it is possible to obtain a good prediction of the local heat transfer coefficient for non-dryout conditions with the pool boiling correlation for each given surface and 2 empirical constants:

$$h_{wet} = a h_{pb} \left(\frac{q_o}{q_{crit}} \right)^b \tag{7.13}$$

Knowing F and h_{wet} it is now possible to predict the local heat transfer coefficient in partial dryout conditions using Eq. (7.9) and Eq. (7.11).

7.2.3 Local heat transfer coefficient prediction statistics

The local heat transfer coefficients were calculated for each tube with the method presented above for heat fluxes between 20 and $60 kW/m^2$ and film Reynolds number up to 2500. The relative error between measured and predicted heat transfer coefficients was calculated for each data point with the following equation:

$$\epsilon = \frac{h_{predicted} - h_{measured}}{h_{measured}} \tag{7.14}$$

Table 7.6 and Table 7.7 give a comparison between the predicted and measured values within an interval of ±30% for each surface and fluid. The prediction of the local heat transfer coefficient for partially dry and wet conditions is also given within ±20% as the prediction method should in practice be performing for wet data. In Fig. (7.11) to Fig. (7.15), experimental vs. predicted data for R134a and R236fa are presented, giving a visual representation of the experimental conditions where the prediction method gives good results.

Tube	All	Wet	Dry	Uncertainty
Plain	$89.9\% \pm 30\%$	$94.6\% \pm 20\%$	$61.2\% \pm 20\%$	$10 - 20\%$
Gewa-C+LW	$84.8\% \pm 30\%$	$70.8\% \pm 20\%$	$78.2\% \pm 20\%$	$20 - 25\%$
Gewa-B4	$73.1\% \pm 30\%$	$79.2\% \pm 20\%$	$32.4\% \pm 20\%$	$25 - 35\%$
Turbo-EDE2	$77.6\% \pm 30\%$	$75.5\% \pm 20\%$	$35.6\% \pm 20\%$	$25 - 35\%$
Gewa-B	$94.1\% \pm 30\%$	$92.7\% \pm 20\%$	$83.2\% \pm 20\%$	$10 - 20\%$
Turbo-BII	$90.7\% \pm 30\%$	$95.8\% \pm 20\%$	$36.1\% \pm 20\%$	$10 - 20\%$
High-Flux	$72.2\% \pm 30\%$	$81.5\% \pm 20\%$	$30.3\% \pm 20\%$	$25 - 35\%$

Table 7.6: Accuracy of the prediction method for R134a

Tube	All	Wet	Dry	Uncertainty
Plain	$82.1\% \pm 30\%$	$87.1\% \pm 20\%$	$28.9\% \pm 20\%$	$15 - 25\%$
Gewa-C+LW	$76.9\% \pm 30\%$	$71.2\% \pm 20\%$	$39.8\% \pm 20\%$	$20 - 25\%$
Gewa-B4	$79.2\% \pm 30\%$	$68.2\% \pm 20\%$	$42.1\% \pm 20\%$	$25 - 30\%$
Turbo-EDE2	$81.2\% \pm 30\%$	$80.6\% \pm 20\%$	$34.2\% \pm 20\%$	$25 - 30\%$

Table 7.7: Accuracy of the prediction method for R236fa

The accuracy of the prediction method is strongly dependent on the measurement uncertainties. The predictions for some of the tube/fluid combinations (the plain tube, the Turbo-BII and the Gewa-B tube) with R134a present similar accuracy, namely equal or above 90% of the data predicted within ±20%. The Gewa-B4, Turbo-EDE2 and High-Flux tubes exhibit higher heat transfer coefficients and thus 70 to 80% of the data are predicted within ±20%. This is mainly due to their higher experimental uncertainties.

Regarding the R236fa data, the prediction for the plain tube is in part penalized by the error made for the film Reynolds number estimation at $q_o = 60kW/m^2$ by assuming ideal downward flow (a significant fraction of the liquid appeared to leave the array); thus the prediction of the partially dry data falls from 87.1% for R134a to 28.9% for R236fa. The prediction for the Gewa-C+LW tube, particularly for partially dry data, falls when using R236fa because of the peak in the heat transfer data found at $Re = Re_{onset}$. The reason for this peak is still not well understood and a larger database of falling film evaporation results involving enhanced condensing tubes will be needed to develop an explanation for this kind of evolution.

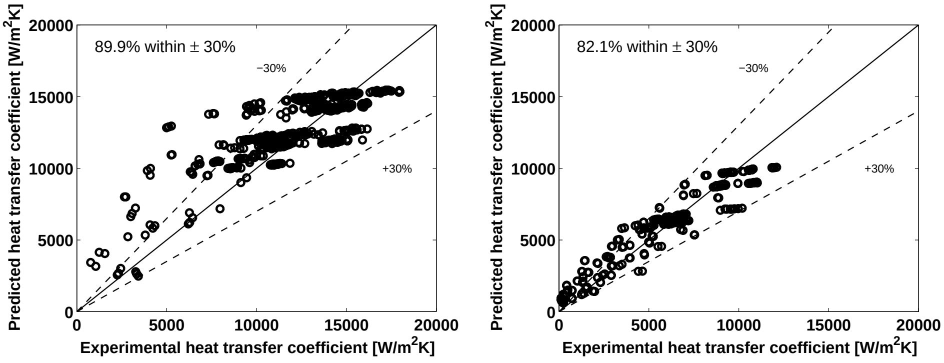

(a) R134a

(b) R236fa

Figure 7.11: Local heat transfer coefficient, experimental vs. predicted on plain tube

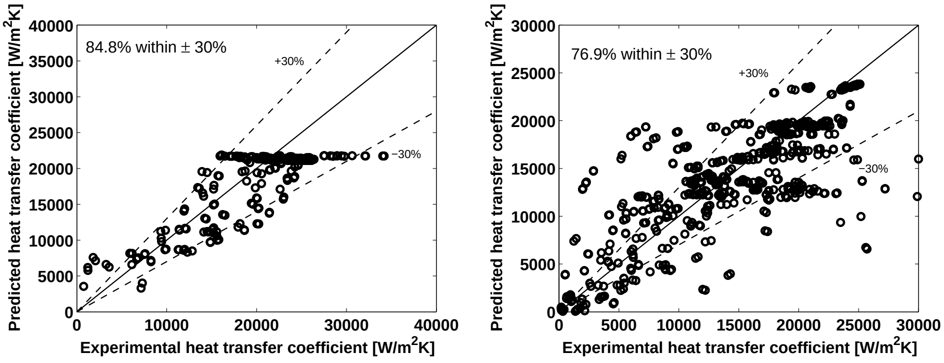

(a) R134a

(b) R236fa

Figure 7.12: Local heat transfer coefficient, experimental vs. predicted on Gewa-C+LW

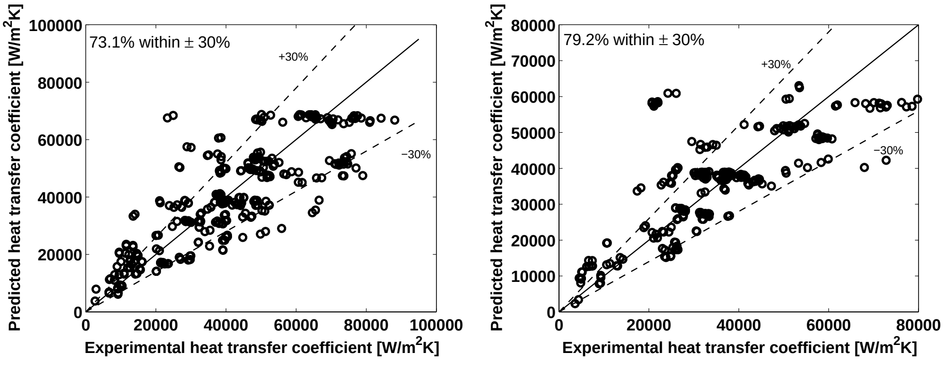

(a) R134a

(b) R236fa

Figure 7.13: Local heat transfer coefficient, experimental vs. predicted on Gewa-B4

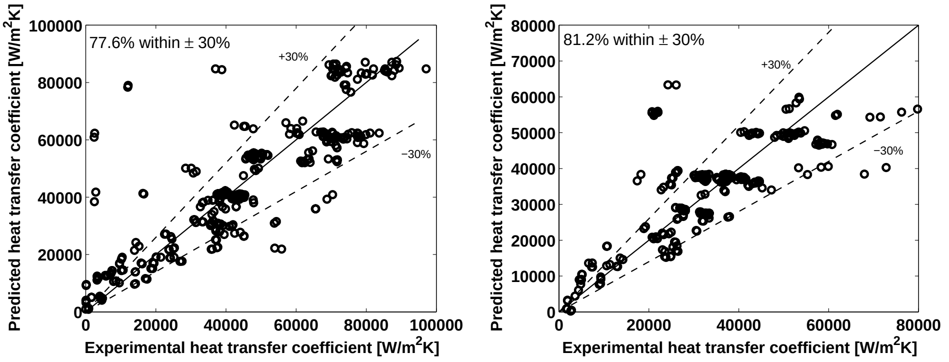

(a) R134a

(b) R236fa

Figure 7.14: Local heat transfer coefficient, experimental vs. predicted on Turbo-EDE2

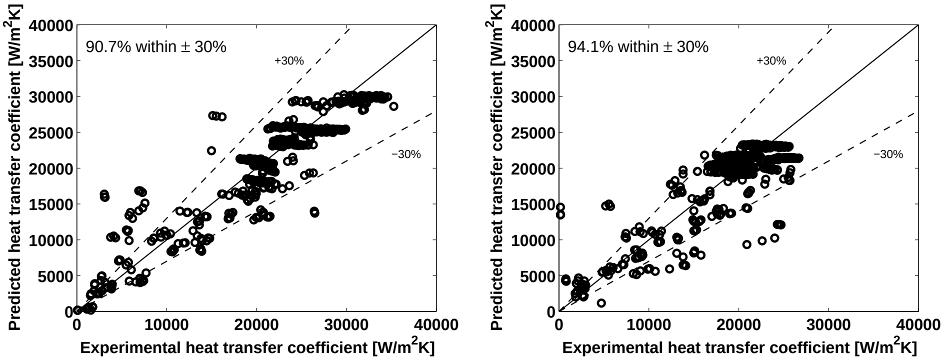

(a) Turbo-BII

(b) Gewa-B

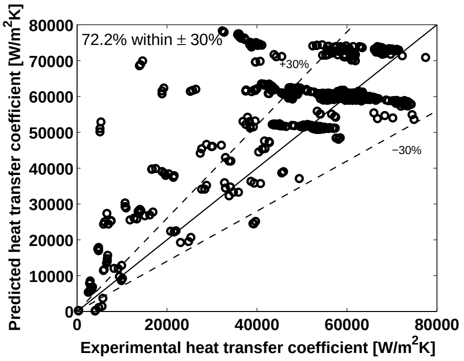

(c) High-Flux

Figure 7.15: Local heat transfer coefficient, experimental vs. predicted on Roques' database [3]

In summary, the proposed empirical approach performs well for predicting the all-wet data, but less so for the more difficult partially-wet data, particularly for the highest performing tubes. This method has the advantage of being simple to use and apply, while requiring a minimum of empirical constants. It can be further improved using more accurate pool boiling data, particularly for low heat fluxes. A unified approach was not yet able to be developed with only one set of empirical constants for all tube/fluid combinations. Such a model will require a thin film evaporation model adapted to handle the particular surface geometry and its dimensions. So far no such model exists even for nucleate pool boiling for the tubes tested here.

Direct comparison of the present method with other authors' data in the literature is not appropriate as those data are tube length averaged data (not local data), which includes local areas of dryout along the tube in the average and have variation of Re along the tube, making it impossible to analyze such data. Furthermore, no other database with the enhanced surfaces and fluids tested here is available in the literature.

7.3 Prediction of bundle heat transfer

As mentioned in Chapter 6, the falling film evaporation bundle results are scattered in part because of a large error propagation on the measurements of such large heat transfer coefficients. Furthermore, the liquid maldistribution within the tube bundle can induce very poor performance locally on the lower part of the bundle by prematurely tripping the onset of dryout. Due to this, the prediction method will be restricted to data only for the top three tubes, as they are less affected by any non-ideal liquid distribution and perform relatively well.

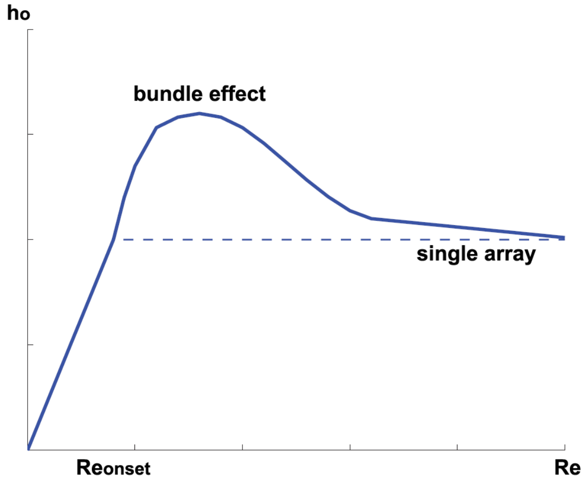

Figure 7.16: Bundle effect

The typical bundle effect observed on these three tubes is shown schematically in Fig. (7.16): with decreasing film Reynolds number as for a film flowing from the top of a bundle towards the bottom, the heat transfer coefficient begins at a plateau corresponding to approximately the single-row array plateau value, then increases to a peak, then falls off again to the single-plateau value, and then falls off rapidly below the onset of dryout threshold. The lack of information on the mechanistic effect of liquid/ bubbly film flow on the boiling process makes prediction of heat transfer quite difficult. Due to the complexity of the flow inside of the bundle, it was thus not possible to present a physically-based model that would adequately predict the data. Instead, an empirical bundle factor B was defined that satisfactorily predicts the results from the database as follows:

$$F = \begin{cases} h_{bundle} = B h_{array} \\ B = 1 + e \exp^{-f(Re - Re_{peak})^2} \end{cases} \tag{7.15}$$

7.3.1 Plain Tube prediction

Eq. (7.15) was applied successfully to the plain tube results for all the database excluding the R236fa results at $60kW/m^2$, in which almost all the tubes were partially dry or nearly completely dry. Fig. (7.17) to Fig. (7.21) show the predictions for R134a and R236fa with the respective precision of the method. Table 7.8 shows the values of e, f and Re_{peak}. The method predicts both partially dry and wet data reasonably well. The bundle factor satisfactorily predicts the peak and the subsequent decrease in heat transfer coefficient. Predicting the partially dry data becomes less precise when increasing the heat flux, due to an increase in bubble generation causing premature local dryout. The single array prediction method (B=1) was used for the R134a data at $60kW/m^2$, giving good prediction of the wet data. This suggests that the bundle effect tends to disappear with increasing heat flux. Using R236fa at high Reynolds numbers, there is a sudden decrease in the heat transfer performance using tubes 1 to 3 (see Fig. (7.21)). In this region, the proposed method does not adequately predict the experimental data, perhaps because the violent boiling for this low pressure fluid tends to throw the liquid film off the surface. The method is presently not general, except in format, since empirical values are required for each heat flux level. Future tests with more extensive data are required for refinement.

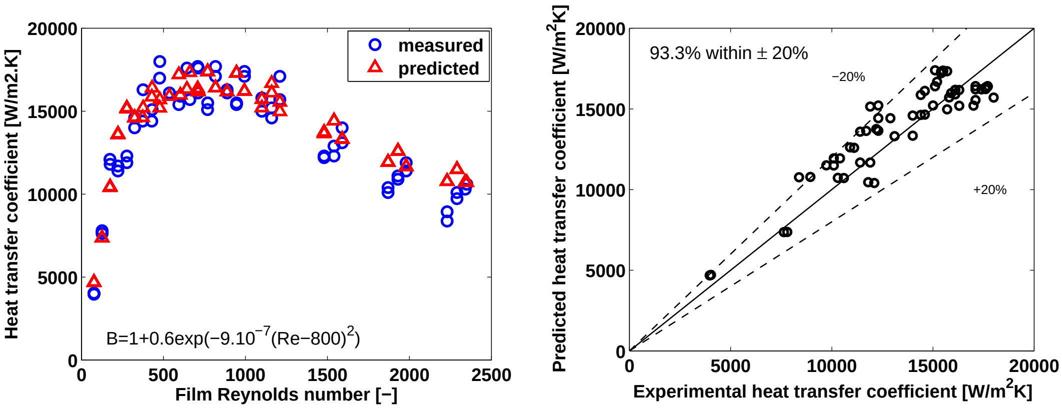

(a) (b)

Figure 7.17: Prediction of the bundle heat transfer coefficient for a plain tube with R134a at $20kW/m^2$

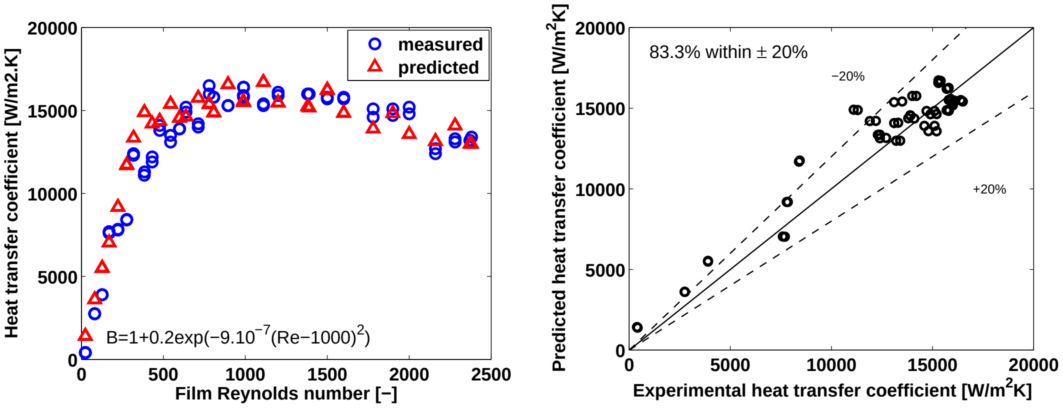

(a) (b)

Figure 7.18: Prediction of the bundle heat transfer coefficient for a plain tube with R134a at $40kW/m^2$

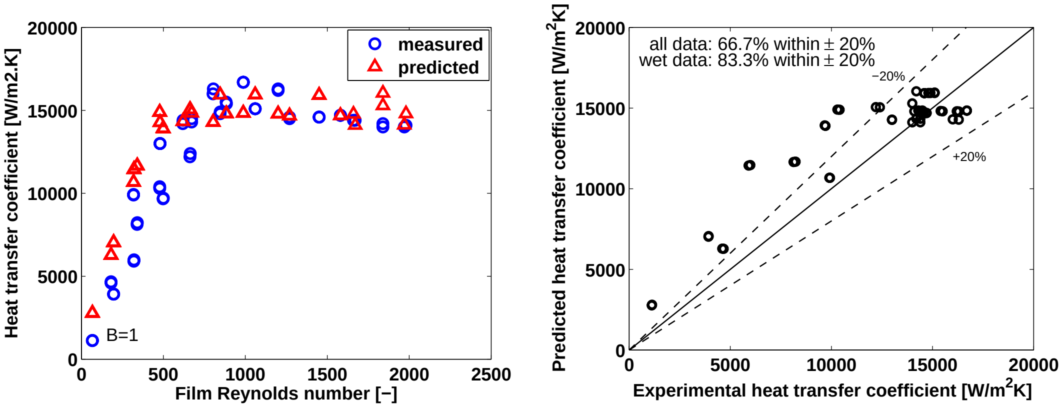

Figure 7.19: Prediction of the bundle heat transfer coefficient for a plain tube with R134a at $60kW/m^2$

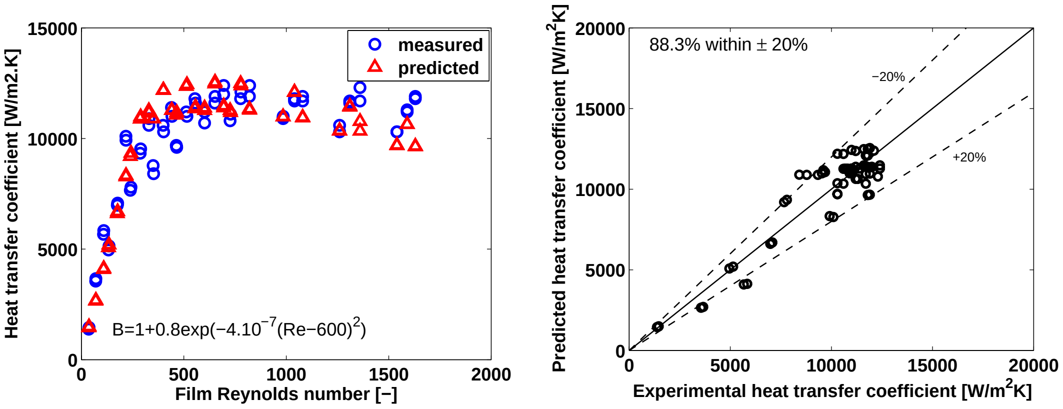

Figure 7.20: Prediction of the bundle heat transfer coefficient for a plain tube with R236fa at $20kW/m^2$

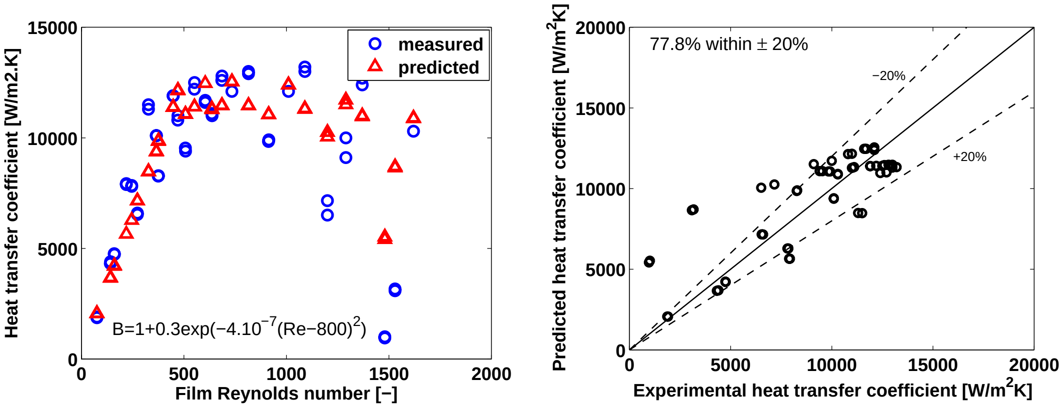

Figure 7.21: Prediction of the bundle heat transfer coefficient for a plain tube with R236fa at $40kW/m^2$

	R134a			R236fa		
Heat Flux	e	f	Re_{peak}	e	f	Re_{peak}
$20kW/m^2$	0.6	9.10^{-7}	800	0.8	4.10^{-7}	600
$40kW/m^2$	0.2	9.10^{-7}	1000	0.3	4.10^{-7}	800

Table 7.8: Empirical constants e, f and Re_{peak} for the plain tube

7.3.2 Enhanced tube prediction

Next, an attempt was made to correlate the experimental data gathered for the enhanced tubes; however, due to the difficulty in obtaining accurate measurements with these tubes, the prediction method defined previously does not work as well as for the plain tube data.

Based on the plain tube results, the assumption was made that the peak seen in the results is wholly a function of the bundle configuration and is actually a bundle effect. It is very improbable that the peak observed on tubes 1 and 2 is a result of an impingement effect from the central distributor, due to the fact that, in the same configuration, this peak is not seen in the single-array results. This is shown in Chapter 5.

Fig. (7.22) to Fig. (7.25) show the comparison between the prediction method and the results obtained for the Gewa-C+LW using both R134a and R236fa at heat fluxes of 40 and $60kW/m^2$. The values of c, d and Re_{peak} are given in Table 7.9. Using R134a, the prediction method and the measurements agree rather well. Neglecting the larger amount of scatter in the R236fa data, it can be seen that the prediction method also fits the experimental data well, albeit with a larger prediction error.

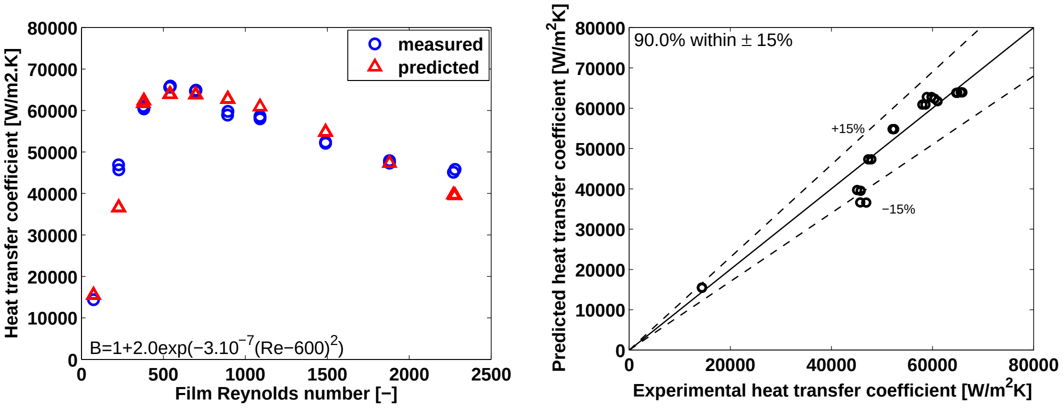

(a) (b)

Figure 7.22: Prediction of the bundle heat transfer coefficient for Gewa-C+LW with R134a at $40kW/m^2$ (Tube 2)

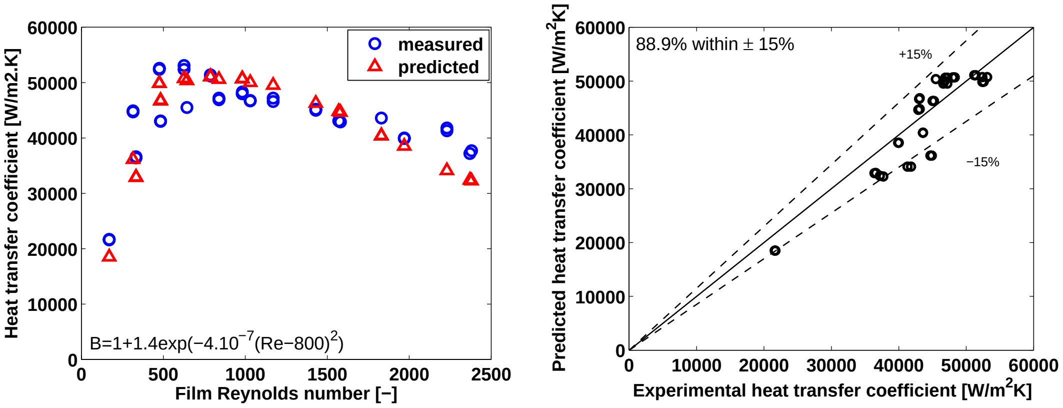

(a) (b)

Figure 7.23: Prediction of the bundle heat transfer coefficient for Gewa-C+LW with R134a at $60kW/m^2$ (Tubes 1 and 2)

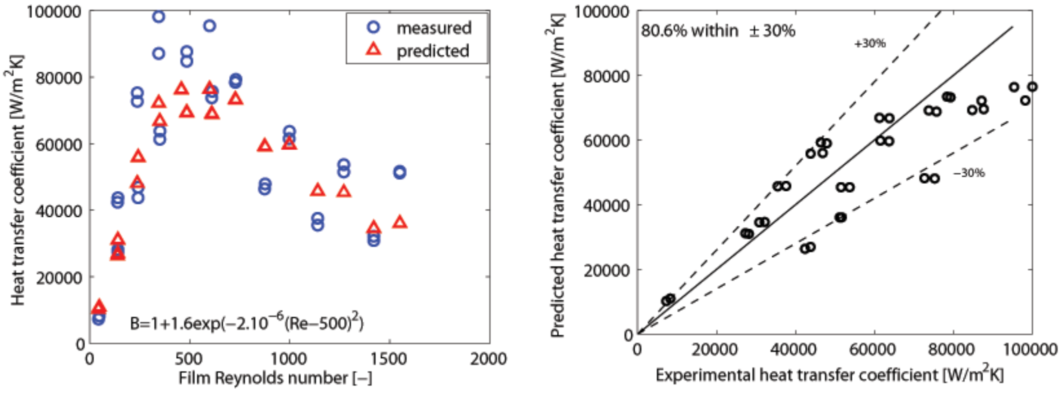

(a) (b)

Figure 7.24: Prediction of the bundle heat transfer coefficient for Gewa-C+LW with R236fa at $40kW/m^2$ (Tubes 2 and 3)

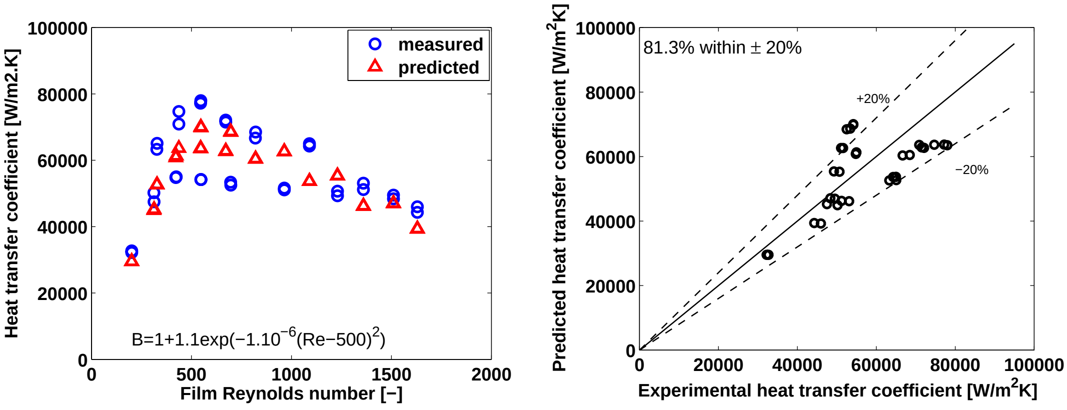

(a) (b)

Figure 7.25: Prediction of the bundle heat transfer coefficient for Gewa-C+LW with R236fa at $60kW/m^2$ (Tubes 1 and 2)

	R134a			R236fa		
Heat Flux	e	f	Re_{peak}	e	f	Re_{peak}
$40kW/m^2$	2.0	3.10^{-7}	600	1.6	2.10^{-6}	500
$60kW/m^2$	1.4	4.10^{-7}	800	1.1	1.10^{-6}	500

Table 7.9: Empirical constants e, f and Re_{peak} for the Gewa-C+LW

Due to the higher propagation of error on the very large heat transfer coefficients for the Gewa-B4 and Turbo-EDE2 tubes, only tubes 1 and 2 will be correlated as they are the less disturbed by the non-uniformity of the liquid flow. For these tubes, the range of film Reynolds numbers tested was not wide enough to characterize the onset of dryout. For these data, the heat transfer performance does not show any large dependance on the film Reynolds number, thus the bundle factor B collapses to a non-unity constant. Table 7.10 gives the values of the bundle factor B for each tube at different heat flux conditions with their respective precision. The data for the Gewa-B4/R236fa data even for the top two tubes was too scattered to fit a method, apparently due to a high sensitivity to the liquid/ bubbly film flow on this enhancement.

	R134a		R236fa	
Heat Flux	Gewa-B4	Turbo-EDE2	Gewa-B4	Turbo-EDE2
$40kW/m^2$	B=1.4	B=1.1	-	B=1.1
Precision	77.8% ± 20%	94.5% ± 5%	-	88.9% ± 20%
$60kW/m^2$	B=1.1	B=0.6	-	B=1.1
Precision	93.8% ± 20%	87.5% ± 10%	-	73.5% ± 20%

Table 7.10: Empirical constant B for the Gewa-B4 and Turbo-EDE2 tube bundle prediction

As an example, it is interesting to note that for the Turbo-EDE2 at $60kW/m^2$ for R134a, the factor B effectively degrades the performance with respect to the single-array results by 40% while increasing it by 10% at $20 kW/m^2$. It is also important to underline that the bundle factor decreases with the bundle depth and that the increase due to the bundle for these tubes is usually quite low ($B \approx 1.1$) compared to the single-array case.

7.3.3 Conclusion

New empirical prediction approaches were developed based on the large experimental database obtained during this study, including a new nondimensional prediction method for the onset of dryout, a simplified method for the single array and another method for the bundle factor. The onset of dryout was predicted with good precision for plain and enhanced tubes tested in the study. The prediction of the local heat transfer coefficient works well (most data within ±20%) for the wet data and the method additionally gives a reasonable prediction of the partially dry data. This method can be applied only by knowing the nucleate pool boiling curve of the fluid/tube combination. However, additional information and data may need to be gathered at low heat fluxes to improve the method. A bundle factor was defined to predict the bundle results based on the single-array prediction.

Chapter 8

Conclusion

The present study involved an experimental investigation of two-phase flow and falling film heat transfer on a tube bundle. Boiling refrigerants were obtained in an operating range comparable to an industrial falling film evaporator. Local heat transfer coefficients were measured for a single-row array and and a 3-row bundle to improve the understanding of the physical phenomena taking place. Different manufactured enhanced tubes were tested to increase the knowledge of the effect of enhanced surfaces on the boiling phenomena in falling film evaporators.

The existing LTCM falling film facility was modified and instrumented to run falling film evaporation measurements in a single-row array of 10 horizontal tubes and a 3-row array of 10 horizontal tubes in each row. Four types of tubes were tested: a plain tube, 2 tubes with mechanically enhanced boiling surfaces and an enhanced condensing tube. Measurements were performed at three different heat fluxes and over a wide range of liquid overfeed. For comparison, heat transfer coefficients were also measured in pool boiling conditions and a falling film multiplier was calculated for each type of surface.

A very large experimental local heat transfer coefficient database was obtained in this study. It covers a wide range of test conditions, comprised of about 20000 data points. The same general trend was observed in single-row array with a mostly constant heat transfer coefficient for a given heat flux in the plateau region until the onset of dryout followed by a rapid decrease of the heat transfer when decreasing liquid overfeed, thus for 2 fluids and 4 different surfaces. In the bundle, different trends were observed depending on the type of tube, but bundle effects were quite evident with respect to the single-row tests. In general, the hydrodynamics of the two-phase film appears to be detrimental to thermal performance, due to the non-uniformities of flow occurring in the bundle.

It was found that the onset of dry patch formation could be correlated with a single expression taking into account the influence of heat flux and fluid properties. The local heat transfer coefficient was correlated using a simple expression based on the nucleate pool boiling curve of the fluid/tube combination. This empirical prediction method fits most of the measured data within ±20% in the single-row configuration. A bundle factor correlation was defined to predict the bundle results based on the single-array prediction.

In order to improve the accuracy on local heat transfer measurements for high-performing enhanced surfaces, some modifications of the actual test facility and instrumentation are suggested. The strong effect of flow distribution on local heat transfer coefficients need further investigation. The flow structure could be possibly correlated to the heat transfer behavior using a visualization system to capture the local variations in the flow over the bundle.

Bibliography

[1] A.E. Bergles. ExHFT for fourth generation heat transfer technology. *Experimental Thermal and Fluid Science*, 26:335–344, 2002.

[2] J.R. Thome. *Enhanced Boiling Heat Transfer.* Hemisphere Publishing Corporation, 1990.

[3] J.F. Roques. *Falling Film Evaporation on a Single Tube and on a Tube Bundle.* PhD thesis, École Polytechnique Fédérale de Lausanne, Department of Mechanical Engineering, 2004.

[4] D. Gstoehl. *Heat Transfer and Flow Visualization of Falling Film Condensation on Tube Arrays with Plain and Enhanced Surface.* PhD thesis, École Polytechnique Fédérale de Lausanne, Department of Mechanical Engineering, 2004.

[5] G. Ribatski and A.M. Jacobi. Falling-film evaporation on horizontal tubes - a critical review. *International Journal of Refrigeration*, 28:635–653, 2005.

[6] Y.H. Wei and A.M. Jacobi. Vapor-shear, geometric, and bundle-depth effects on the intertube falling-film modes. *1st Int. Conf. On Heat Transfer, Fluid Mechanics, and Thermodynamics, South Africa*, pages 40–46, 2002.

[7] J.J. Lorenz D. Yung and E.N. Ganic. Vapor/liquid interaction and entrainment in falling film evaporators. *Journal of Heat Transfer*, 77:69–73, 1980.

[8] J. R. Thome. *Engineering Databook III.* http://www.wlv.com/products/databook/db3DataBookIII.pdf, 2006.

[9] R. Bellman and R.H. Pennington. Effects of surface tension and viscosity on Taylor instability. *Q. Appl. Math.*, 12:151–161, 1954.

[10] J. Mitrovic. Vapor/liquid interaction and entrainment in falling film evaporators. *Proc. 8th Int. Heat Tranfer Conf., San Francisco*, 4:1949–1956, 1986.

[11] X. Hu and A.M. Jacobi. The intertube falling film, part 1: Flow characteristics, mode transitions, and hysteresis. *J. Heat Transfer*, 118:616–625, 1996.

[12] R. Armbruster and J. Mitrovic. Patterns of falling film flow over horizontal smooth tubes. *Proc. 10th Int. Heat Transfer Conference, Brighton, U.K.*, pages 275–280, 1994.

[13] D. Gstoehl J.F. Roques and J.R. Thome. Falling film transitions on plain and enhanced tubes. *J. Heat Transfer*, 124:491–499, 2002.

[14] S. Nozu H. Honda and Y. Takeda. Flow characteristics of condensate on a vertical column of horizontal low finned tubes. *Proc. ASME-JSME Thermal Engineering Joint Conference, Honolulu*, 1:517–524, 1987.

[15] M.S. El-Genk and H.H. Saber. Minimum film thickness of a flowing down liquid film on a vertical plate. *Int. Journal of Heat and Mass Transfer*, 44:2809–2825, 2001.

[16] E.N. Ganic and D. Getachew. Effects of surface condition and working fluid on liquid film breakdown during heat transfer. *8th Int. Heat Transfer Conf.*, pages 1931–1936, 1986.

[17] Y. Fujita and M. Tsutsui. Experimental investigation of falling film evaporation on horizontal tubes. *Heat Transfer - Japanese Research*, 27:609–618, 1998.

[18] W. Nüsselt. Die oberflächenkondensation des wasserdampfes. *Zeitschr. Ver. Deutsch Ing.*, 60:541–546 and 569–575, 1916.

[19] S. Sinkunas. Fluid mechanics and heat transfer in film flow down a horizontal cylinder. *3rd European Thermal Sciences Conf.*, pages 265–268, 2000.

[20] S.B.G O'Brien and L.W. Schwartz. Theory and modeling of thin film flows. *Encyclopedy of Surface and Colloid Science*, pages 5283–5297, 2002.

[21] J.P. Hartnett W.M. Rohsenow and E.N. Ganic. *Handbook of heat transfer fundamentals - Chapter 12 P. Thin-Film Heat Transfer.* New York : McGraw-Hill, 1985.

[22] M.C. Chyu and A.E. Bergles. Falling film evaporation on a horizontal tube. *Multiphase Flow and Heat Transfer, ASME HTD*, 43:39–48, 1985.

[23] V.T. Morgan. The overall convective heat transfer from smooth circular cylinders. *Advances in Heat Transfer*, 11:199–264, 1975.

[24] S.W. Churchill and H.H.S. Chu. Correlating equations for laminar and turbulent free convection from a vertical plate. *Int. J. of Heat and Mass Transfer*, 18:1323–1329, 1975.

[25] W.M. Rohsenow. A method of correlating heat transfer data for surface boiling liquids. *Transactions of ASME*, 74:969–976, 1952.

[26] E. Ishibashi and K. Nishikawa. Saturated boiling heat transfer in narrow spaces. *Int. J. of Heat and Mass Transfer*, 12:863–894, 1969.

[27] K. Stephan. *Heat transfer in condensation and boiling.* Springer, Berlin, 1992.

[28] K. Stephan and M. Abdelsalam. Heat transfer correlation for natural convection boiling. *Int. J. of Heat and Mass Transfer*, 23:73–87, 1980.

[29] W. Fritz. Berechnung des maximalvolumes von dampfblasen. *Physik Zeitschr.*, 36:379Ű384, 1935.

[30] M.G. Cooper. Heat flow rates in saturated nucleate pool boiling. A wide-range examination using reduced properties. *Advances in Heat Transfer*, 16:157–239, 1984.

[31] D. Gorenflo. *Pool boiling in VDI Heat Atlas.* VDI- Verlag GmbH, Düsseldorf, Germany, 1993.

[32] M. Cerza and V. Sernas. A bubble growth model for nucleate boiling in thin, falling, superheated, laminar, water films. *Int. J. Heat and Mass Transfer*, 28:1307–1316, 1985.

[33] A.E. Bergles. Heat transfer augmentation. *Two-Phase Flow Heat Exchangers*, pages 343–373, 1988.

[34] L.H. Chien and R.L. Webb. A parametric study of nucleate boiling on structured surfaces, part I: Effect of tunnel dimensions. *Journal of Heat Transfer*, 120:1042–1048, 1998.

[35] L.H. Chien and R.L. Webb. A parametric study of nucleate boiling on structured surfaces, part II: Effect of pore diameter and pore pitch. *Journal of Heat Transfer*, 120:1049–1054, 1998.

[36] M.E. Poniewski and J.R. Thome. *Nucleate Boiling on Micro-structured Surfaces.* www.htri-net.com/ePubs/epubs.htm, 2008.

[37] V. Sernas L.S. Fletcher and W.H. Parken. Evaporation heat transfer coefficients for thin sea water films on horizontal tubes. *Ind. Eng. Chem., Process Des. Dev.*, 14:411–416, 1975.

[38] V. Sernas W.H. Parken, L.S. Fletcher and J.C. Han. Heat transfer through falling film evaporation and boiling on horizontal tubes. *Transactions of ASME*, 112:744–750, 1990.

[39] R. Armbruster and J. Mitrovic. Heat transfer in falling film on a horizontal tube. *Heat Transfer Conference - ASME*, 12:13–21, 1995.

[40] M.C. Chyu X. Zeng and Z.H. Ayub. Evaporation heat transfer performance of nozzle-sprayed ammonia on a horizontal tube. *Ashrae Transactions*, 101:136–149, 1996.

[41] Y. Fujita and M. Tsutsui. Evaporation heat transfer of falling films on horizontal tubes. Part 2: Experimental study. *Heat Transfer - Japanese Research*, 24:17–31, 1995.

[42] X. Hu and A.M. Jacobi. The intertube falling film, part 2: Mode effects on sensible heat transfer to a falling liquid film. *J. Heat Transfer*, 118:626–633, 1996.

[43] S.A. Moeykens and M.B. Pate. Spray evaporation heat transfer of R134a on plain tubes. *Ashrae Transactions*, 100:173–184, 1994.

[44] V. Sernas L.S. Fletcher and L. Galowin. Evaporation from thin water films on horizontal tubes. *Ind. Eng. Chem., Process Des. Dev.*, 13:265–269, 1974.

[45] E.N. Ganic and M.N. Roppo. An experimental study of falling liquid film breakdown on a horizontal cylinder during heat transfer. *J. Heat Transfer*, 102:342–346, 1980.

[46] M.C. Chyu and A.E. Bergles. An analytical and experimental study of falling-film evaporation on a horizontal tube. *Journal of Heat Transfer*, 109:983–990, 1987.

[47] L.S. Fletcher W.H. Parken. Heat transfer in liquid thin films flowing over horizontal tubes. *Proceedings of the 7th Int. Heat Transfer Conf.*, 4:415–420, 1982.

[48] Y. Fujita and M. Tsutsui. Experimental and analytical study of evaporation heat transfer in falling films on horizontal tubes. *Proc. of the 10th Int. Heat Transfer Conf., Brighton*, 6:175–180, 1994.

[49] X. Zeng M.C. Chyu and Z.H. Ayub. Nozzle-sprayed flow rate distribution on a horizontal tube bundle. *ASHRAE Transactions*, 101:443–453, 1995.

[50] V. Charan R.S. Rana and H.K Varma. Heat and mass transfer from a horizontal tube of an evaporative heat dissipator. *Int. J of Heat and Mass Transfer*, 29:555–562, 1986.

[51] G. Ribatski and J.R. Thome. A visual study of R134a falling film evaporation on enhanced and plain tubes. *5th Int. Symp. on Multiphase Flow, Heat Mass Transfer and Energy Conversion*, 3-6 July 2005:Xi'an, China, 2005.

[52] V.G. Burkin G.N. Danilova and V.A. Dyundin. Heat transfer in spray-type refrigerator evaporators. *Heat Transfer - Soviet Research*, 8:105–113, 1976.

[53] L.H. Chien and R.L Webb. Visualization of pool boiling on enhanced surfaces. *Experimental Thermal and Fluid Science*, 16:332–341, 1998.

[54] W.W. Huebsch S.A. Moeykens and M.B. Pate. Heat transfer of R134a in single tube spray evaporation including lubrificant effect and enhanced surface results. *ASHRAE Transactions*, 101:111–123, 1995.

[55] J.J. Lorenz and D. Yung. Film breakdown and bundle-depth effects in horizontal-tube, falling-film evaporators. *Journal of Heat Transfer*, 104:569–571, 1982.

[56] T.B. Chang and J.S. Chiou. Spray evaporation heat transfer of r-141b on horizontal tube bundle. *Int. J. of Heat and Mass Transfer*, 42:1497–1478, 1999.

[57] M.C. Chyu X. Zeng and Z.H. Ayub. Experimental investigation on ammonia spray evaporator with triangular-pitch tube bundle, part i: tube bundle effect. *Int. J. of Heat and Mass Transfer*, 44:2299–2310, 2001.

[58] B.J. Newton S.A. Moeykens and M.B. Pate. Effects of surface enhancement film feed-supply rate, and bundle geometry on spray evaporation heat transfer performance. *ASHRAE Transactions*, 101:408–419, 1995.

[59] J.E. Kelly S.A. Moeykens and M.B. Pate. Spray evaporation heat transfer performance of r123 in tube bundles. *ASHRAE Transactions*, 102:259–272, 1996.

[60] J.J. Lorenz and D. Yung. A note to combined boiling and evaporation of liquid films on horizontal tubes. *Transactions of the ASME*, 101:178–180, 1979.

[61] K.R. Chun and R.A. Seban. Heat transfer to evaporating liquid films. *Journal of Heat Transfer*, 93:391–396, 1971.

[62] L.H. Chien and C.H. Cheng. A predictive model of falling film evaporation with bubble nucleation on horizontal tubes. *HVAC Research*, 12:69–87, 2006.

[63] K. Tuzla A.A. Alhusseini and J.C. Chen. Falling film evaporation of single component liquids. *Int. Journal of Heat and Mass Transfer*, 41:1623–1632, 1998.

[64] G. Ribatski and J.R. Thome. Experimental study on the onset of local dryout in an evaporating falling film on horizontal plain tubes. *Experimental Thermal and Fluid Science*, 31:483–493, 2007.

[65] V. Gnielinski. New equations for heat and mass transfer in turbulent pipe and channel flow. *Advances in Heat Transfer*, 16:359–368, 1976.

[66] H. Kuwahara W. Nakayama, T. Daikoku and T. Nakajima. Dynamic model of enhanced boiling heat transfer omn porous surfaces. part ii: Analytical modeling. *Journal of Heat Transfer*, 102:451–456, 1980.

[67] Z.H. Ayub and A.E. Bergles. Pool boiling from Gewa surfaces in water and R113. *Wärme and Stoffübertragung*, 21:209–219, 1987.

[68] L.H. Chien and R.L. Webb. A nucleate boiling model for structured enhanced surfaces. *Int. J. of Heat and Mass Transfer*, 41:2183–2195, 1998.

[69] National Institute of Standards and Technology. *NIST Thermodynamic Properties of Refrigerants and Refrigerant Mixtures Database.* ver 7.0, Gaithersburg, MD, 2002.

[70] E.E. Wilson. A basis for rational design of heat transfer apparatus. *Trans. ASME*, 37:47–82, 1915.

[71] R.K. Shah. Assessment of modified Wilson plot techniques for obtaining heat exchanger design data. *Proc. 9th Int. Heat Transfer Conference*, 5:51–56, 1990.

[72] D.E. Briggs and E.H. Young. Modified wilson plot techniques for obtaining heat transfer coefficients for shell and tube heat exchangers. *Chemical Engineering Progress Symposium Series*, 65:35–45, 1969.

[73] R.N. Christensen H.F. Khartabil and D.E. Richards. A modified wilson plot technique for determining heat transfer correlations. *Proc. 2nd UK National Heat Transfer Conference*, C168/88:1331–1357, 1988.

[74] J.W. Rose. Heat-transfer coefficients, Wilson plots and accuracy of thermal measurements. *Experimental Thermal and Fluid Science*, 28:77–86, 2004.

[75] A. Joardar A.I. El Sherbini and A.M. Jacobi. Modified Wilson-plot technique for heat exchanger performance: Strategies for minimizing uncertainty in data reduction. *International Refrigeration and Air Conditioning Conf.*, Purdue:1–8, 2004.

[76] B.S. Petukhov. Heat transfer and friction in turbulent pipe flow with variable physical properties. *Advances in Heat Transfer*, 6:503–564, 1970.

[77] S.J. Kline and F.A. McClintock. Describing uncertainties in single-sample experiments. *Mechanical Engineering*, 75:3–8, 1953.

[78] Y. Ko D. Jung, Y. Kim and K. Song. Nucleate boiling heat transfer coefficients of pure halogenated refrigerants. *Int. Journal of Refrigeration*, 26:240–248, 2003.

[79] R.L. Webb and C. Pais. Nucleate pool boiling data for five refrigerants on plain, integral-fin and enhanced tube geometries. *International Journal of Heat and Mass Transfer*, 35:1893–1904, 1992.

[80] S.S. Hsieh and P.T. Hsu. Nucleate boiling characteristics of R114, distilled water and R134a on plain and rib-roughened tube geometries. *International Journal of Heat and Mass Transfer*, 37:1423–1432, 1994.

[81] D. Robinson and J.R. Thome. Flooded evaporation heat transfer performance investigation for tube bundles including the effects of oil using R410a and R507a. Technical report, ASHRAE Research Project RP-1089, 2003.

[82] M.-C. Chyu X. Zeng and Z.H. Ayub. Performance of nozzle-sprayed ammonia evaporator with square-pitch plain-tube bundle. *ASHRAE Transactions*, 103:68–81, 1997.

[83] J.R. Thome J.-F. Roques. Falling films on arrays of horizontal tubes with r-134a, part i: Boiling heat transfer results for four types of tubes. *Heat Transfer Engineering*, 28:398Ű414, 2007.

[84] D. Robinson and J.R. Thome. Local bundle boiling heat transfer coefficients on a turbo-bii hp enhanced tube bundle. *HVAC&R Research*, 10:441Ű457, 2004.

[85] F. Agostini. *Boiling on a Tube Bundle: Heat Transfer, Pressure Drop and Flow Patterns.* PhD thesis, École Polytechnique Fédérale de Lausanne, Department of Mechanical Engineering, 2008.

Curriculum Vitae

PERSONAL DATA

Name	**Mathieu HABERT**
Date of birth	14th February, 1982
Birthplace	Toul, France
Nationality	French

EDUCATION

2005–2009	**Doctoral Student and Assistant**, Laboratory of Heat and Mass Transfer, Swiss Federal Institute of Technology Lausanne (EPFL), Switzerland
1999–2004	**Master studies in Energy and Environment**, INSA Lyon, France
1996–1999	**High School Certificate**, Lycée Majorelle, Toul, France

WORKING EXPERIENCE

2005–2009 **Swiss Federal Institute of Technology (EPFL), Laboratory of Heat and Mass Transfer, Lausanne**, research project development, industrial contract, laboratory activity, students supervision and training:

- Falling film evaporation on tube bundle. Facility modifications, heat transfer measurements and predictions. Work supervised by Prof. John R. Thome;
- Consulting Work. Study and analysis of the thermal characteristics of an iron for the company Laurastar. Heat transfer consultancy for the company Creative Heating Services. Infrared imagery consultancy at EPFL;
- Lecturing (4h of theoretical work and 80h of practical work). Master/Diploma projects supervision.

2003–2004 **INSA Lyon, Energy and Environment department, France**, research project and laboratory activity:

- Numerical simulation of the thermal exchanges within the human body when exposed to an electromagnetic wave. Work supervised by Prof. B. Lips (CETHIL-TIM) and N. Siauve (CEGELY).